University of Southampton

Faculty of Physical Sciences and Engineering

Optoelectronics Research Centre

Characterisation of Hollow Core Fibres

by

Xuhao Wei

ORCID ID 0000-0002-1176-3551

Thesis for the degree of Doctor of Philosophy

September, 2024

University of Southampton

Abstract

Faculty of Physical Sciences and Engineering
Optoelectronics Research Centre

Doctor of Philosophy

Characterisation of Hollow Core Fibres

by

Xuhao Wei

For conventional optical fibres such as single mode fibres (SMFs), the development of characterisation techniques has played a crucial role in their success. This is because characterisation contributes in various aspects such as performance improvement and quality assurance. However, characterization for the emerging low loss hollow core fibres (HCFs) has regrettably lagged behind the rapid advancements in HCFs over the past three decades. This becomes particularly urgent when their loss (0.174 dB/km) is reaching the level of SMFs. In response to this disparity, this Thesis endeavours to explore and develop novel characterisation techniques for low loss HCFs, aiming to facilitate a deeper understanding and enhance the optimization of their performance.

The thesis unfolds in two main topics. The first delves into the impact of coating on the overall thermal sensitivity of HCFs. In both experimental observations and simulations, we demonstrate that the coating significantly influences thermal sensitivity. Remarkably, the coating is observed to introduce relaxation effects in optical phase stability (phase change goes back partly once temperature stays unchanged), which has not been previously discussed in the HCFs literature, to the best of our knowledge. The analysis on this effect is conducted via simulations, suggesting that this effect is caused by the viscoelastic properties of the coating. Finally, based on the studies of coating, a novel strategy is proposed to reduce the thermal sensitivity of a HCF when spooled, of interest to applications such as ultra-stable laser locking.

The second topic focuses on the distributed HCF characterisation using the technique of Optical Time Domain Reflectometer (OTDR). We firstly build a high dynamic range OTDR system (>45 dB) with high spatial resolution (<2 m). The system enables measurement of the backscattering in HCFs, allowing the distributed characterisation of HCFs not only when air-filled, but also when being evacuated. This enables real time distributed monitoring of HCFs evacuation, serving as a tool for studying the gas flow in HCFs. Furthermore, the backscattering of the HCFs varies with the air pressure within the core and the core size along the HCF length. This variation poses challenges for direct distributed loss measurement, as the backscattering signal depends on both the backscattering coefficient and the loss. The strategy is demonstrated on how to measure and process OTDR traces

to enable distributed loss measurement. Finally, this technique also enables monitoring of the backscattering coefficient variation along the HCF length.

Table of Contents

Table of Contents I

Table of Tables V

Table of Figures VII

Research Thesis: Declaration of Authorship XVI

Acknowledgements XVIII

Definitions and Abbreviations XX

Chapter 1. Introduction 1

1.1 Motivation 1

1.2 Research focus of the thesis 2

1.2.1 Thermal Sensitivity of Coated HCFs (Topic-1) 2

1.2.2 Distributed characterisation of HCFs (Topic-2) 4

1.3 Thesis Objectives 6

1.3.1 Thermal Sensitivity of Coated HCFs 6

1.3.2 Distributed characterisation of HCFs 6

1.4 Thesis outline 6

Chapter 2. Background: Introduction of Hollow Core Fibres 9

2.1 Historical perspective 9

2.2 Guiding principle 11

2.2.1 PBGFs 11

2.2.2 ARFs 12

2.3 Loss in HCFs 13

2.4 Unique features and their applications 14

2.4.1 Low latency 14

2.4.2 High thermal stability 14

2.4.3 Ultralow backscattering 15
2.4.4 High damage threshold and ultralow nonlinearities 15
2.4.5 Gas photonics 16
2.5 Fabrication of HCFs 16
2.6 Fibre coating 17
Chapter 3. Background: Introduction of HCFs' characterisation 21
3.1 COMSOL Multiphysics 21
3.2 Measurement of thermal phase sensitivity 23
3.2.1 Principle 23
3.2.2 Factors in measurements 25
3.3 Optical Time-Domain Reflectometry (OTDR) 27
3.3.1 Backscattering 27
3.3.2 Working principle 28
3.3.3 Key parameters 31
Chapter 4. Effect of Coating on thermal sensitivity of HCFs 35
4.1 Coating-induced change 35
4.1.1 Experiment 35
4.1.2 Simulation 38
4.1.3 Results and discussion 41
4.2 Coating-induced effect of relaxation 43
4.2.1 Relaxation observed experimentally and its quantification 43
4.2.2 Modified model for simulating relaxation of the dual-coated HCF 43
4.2.3 Fitting of coating's properties 46
4.3 Conclusion 50
Chapter 5. Thermally insensitive HCF coil 51
5.1 Principle of operation 51

5.2 Toy model 52
5.3 Coil model and Simulation 53
5.3.1 Number of turns 57
5.3.2 Coil diameter and number of layers 57
5.3.3 Fibre gap 58
5.4 HCF Coil-winding and updated simulation 59
5.5 Setup for Characterisation 61
5.6 Result 62
5.7 Conclusion 65
Chapter 6. Highly sensitive OTDR system 67
6.1 Pulse characterisation 67
6.1.1 Short-Pulse (ns-scale) measurement 67
6.1.2 Extinction ratio 69
6.2 Pulse generation and amplification 69
6.2.1 Pulse generation 69
6.2.2 Pulse amplification 72
6.3 Building a highly sensitive OTDR system 77
6.3.1 System based on a photo-counting OTDR 79
6.3.2 System based on a standard OTDR 85
6.4 Conclusion 87
Chapter 7. Distributed characterisation of HCFs 89
7.1 Air-filled HCFs 89
7.2 Evacuation of HCFs 92
7.2.1 Evacuation of a NANF (gas flow) 93
7.2.2 Evacuation of a DNANF (surface scattering) 101
7.3 End facet contamination 103

7.4 Bi-directional OTDR analysis 104
7.4.1 Principle 105
7.4.2 OTDR system calibration 108
7.4.3 Experimental results 110
7.4.4 Discussion 115
7.5 Conclusion 116
Chapter 8. Summary and future work 117
8.1 Summary 117
8.2 Future work 118
Appendix A: Pulse amplification optimisation 121
Appendix B: Publications 125
List of Reference 127

Table of Tables

Table 2.1 Properties of the two coating materials.....19

Table 4.1 The parameter of the used HCF samples.....35

Table 4.2 The model geometry (2D model) and its materials. 40

Table 4.3 Properties of the used silica in model. 41

Table 5.1 Typical material properties of optical fibre and their coatings, as considered in our simulations.....54

Table 6.1 Key parameters of pulse. 72

Table 6.2 Key parameters of pulses generated from the three setups above (* calculated using extinction ratio of 50 dB). 77

Table 6.3 Performance comparison between the amplified OTDR and non-amplified. 81

Table 7.1 Performance comparison of Amplified FOTR-203 and photon counting LOR-200 OTDR. 91

Table 7.2 Parameters of HCF samples. 110

Table 7.3 Comparison between the average loss extracted from the OTDR measurement and loss from cutback measurement. 115

Table of Figures

Figure 1.1 The measured backscattering in a NANF [9]. 5

Figure 2.1 Key achievements of PBGFs. 10

Figure 2.2 Key achievements of ARFs. 11

Figure 2.3 PBG Guidance (a) 1-D; (b) 2-D. 12

Figure 2.4 ARROW model [28] and its transmission spectrum (bottom) [69]. 13

Figure 2.5 Phase change of the light through 20 m lengths of SMF-28 (solid) and HC-PBGF (dashed), where the temperature was changed by 0.5°C peak-to-peak every 1000 s [10]. 15

Figure 2.6 Scalability of near-diffraction-limited CW power delivery in optical fibres at 1 μm, limited by SRS (The solid lines show the maximum fibre length versus the target output power achievable for a standard silica SMF, a large-core-area silica PCF, and an air-filled NANF [8]). 16

Figure 2.7 Fibre drawing process for ARFs [92]. 17

Figure 2.8 The Young's modulus of the primary coating (DP-1021) and secondary coating (DS-2042). 20

Figure 3.1 Experimental setup for HCF thermal phase sensitivity measurement based on a Mach-Zehnder interferometer (PD: photodetector; DAQ: data acquisition card). 23

Figure 3.2 Schematic of the optic for the (3x3) passive homodyne detection (PD1, PD2, PD3, the three outputs of the interferometer) [97]. 24

Figure 3.3 The calculated visibility as a function of the normalized intensity of $I2/I1$. 26

Figure 3.4 Polarization states of the lights on the two arms. 27

Figure 3.5 Spectrum of light scattering. 28

Figure 3.6 The illustration of scattering in a fibre and Fresnel reflection at the interface between fibre and air. 29

Figure 3.7 The typical setup of an OTDR system and a typical trace (PC: computer for data processing; DAQ: data acquisition card; PD: photodetector; AOM: acousto-optic modulator). 29

Figure 3.8 Dynamic range definitions. 32

Figure 3.9 Illustration of the Dead zone. 32

Figure 4.1 Cross section of (a) the dual-coated HCF and (b) thinly coated HCF with coating shown in yellow. 36

Figure 4.2 Experimental setup based on M-Z interferometer. 36

Figure 4.3 The measured phase and temperature changes of a 30 m dual-coated HCF (Thickness of coating: 123 μm)..... 37

Figure 4.4 The measured phase and temperature changes of a 24 m thinly-coated HCF (Thickness of coating: 10 μm)..... 37

Figure 4.5 The measured static thermal phase sensitivity of a dual coated HCF and a thinly coated HCF. 38

Figure 4.6 The measured dynamic thermal phase sensitivity of a dual coated HCF and a thinly coated HCF. 38

Figure 4.7 A dual-coated HCF cross-section (a) A HCF cross-section (red dotted circle: core in literatures; green solid circle: the defined core used in simulation) (b) The simplified dual-coated HCF structure for simulation. 39

Figure 4.8 (a) 2D model and (b) the corresponding 3D structure of the HCF in model. 40

Figure 4.9 Simulated and measured static thermal phase sensitivities of dual coated and thinly coated HCFs. 41

Figure 4.10 Simulated and measured dynamic thermal phase sensitivities of dual coated and thinly coated HCFs. 42

Figure 4.11 Phase Relaxation of the dual-coated HCF. 43

Figure 4.12 Updated HCF model to enable the simulation of the phase relaxation (viscoelastic material model used for both coatings, in blue). 44

Figure 4.13 An initial ‘proof of concept’ relaxation time used in in COMSOL model for both coatings. 45

Figure 4.14 Simulated phase change with the new viscoelastic model and its comparison to that using elastic theory. 45

Figure 4.15 Stress partly relaxed inside the new modelled coated HCF. 46

Figure 4.16 Phase change caused by the change of TEC of primary coating/secondary coating (Primary coating: 10 times reduction of the TEC based on the reference; Secondary coating: 2 times reduction of the TEC based on the reference;). 47

Figure 4.17 Simulated phase change after we modified the relaxation time. 47

Figure 4.18 Simulated phase change after TEC of secondary coating was reduced. 48

Figure 4.19 Simulated phase change after we reduced the TEC of silica jacket. 48

Figure 4.20 Simulated phase change with the increased Young's modulus of secondary coating. 49

Figure 4.21 The fitted parameters (a) Young's modulus of the secondary coating (b) TEC of the secondary coating (c) Relaxation time of the secondary coating (d) TEC of the silica jacket. 50

Figure 5.1 A 2D axisymmetric model (a) used to simulate a 3D cylinder shell (b). It is made of an Inner layer (Young's modulus = 0.55 MPa; TEC = 863 ppm/°C; thickness= 75 μm); and an Outer layer (Young's modulus = 73100 MPa; TEC = 0.5 ppm/°C; thickness= 75 μm). 52

Figure 5.2 Deformation and circumferential stress distribution of the two-layer cylinder shell cross section (temperature change: 30°C - 40°C). Here, the arrows show the deformation direction. The inner side of the Inner layer shrinks, introducing a negative inner diameter change of -14.7 nm (negative stress), while the outer boundaries of the Inner layer and Outer layer both expand (by +1.2 nm and +2.0 nm, respectively, positive stress). 53

Figure 5.3 The built HCF semi-coil model made with (a) bare HCF and (b) dual-coated HCF. (Coil diameter: 100 mm; number of layers: 5, materials shown in Table 5.1). 54

Figure 5.4 The calculated average circumference change of each layer in a HCF coil following the model shown in Figure 5.3 (bare HCF, black dots; dual-coated HCF, red circles; temperature change: 30°C - 40°C).....55

Figure 5.5 Circumferential Stress distribution of the model in Figure 5.3 (a) bare HCF (b) dual-coated HCF.....55

Figure 5.6 The calculated relative length change of the dual-coated HCF coil (temperature change: 30°C - 40°C). For coiled HCF (red circles), this change is shown for the inner *N* layers of the 5-layer coil (Figure 5.3 (b)). The change of uncoiled HCF is shown as a black solid line for comparison. 56

Figure 5.7 Key coil parameters. 56

Figure 5.8 Average length change per turn per layer in layers 1 to N (Sum of layers) for different number of turns (coil diameter: 100 mm; number of layers: 5; temperature change: 30°C - 40°C). 57

Figure 5.9 Simulated coil performance R for different total number of layers N_{tot} and coil diameters of 70 mm (black squares), 100 mm (red circles), 200 mm (blue triangles), and 300 mm (green stars) (temperature change: 30°C - 40°C). 58

Figure 5.10 Simulated influence of the gap distance on coil performance R (coil diameter: 100 mm) (temperature change: 30°C - 40°C). 59

Figure 5.11 Simulated influence of the HCF length on coil performance R considering coil realized experimentally (diameter of coil: 160 mm; fibre gap: 116 µm, number of turns: 57). 60

Figure 5.12 Simulated thermal phase sensitivity of the prepared HCF coil and the uncoiled HCF for comparison. 60

Figure 5.13 Photograph of the prepared support-free HCF coil (diameter of 160 mm; pitch of 500 µm; N_{tot} = 19; 57 turns). 61

Figure 5.14 Experimental setup for thermal sensitivity characterization of the HCF coil with the insert showing the cross-section of the used HCF (PD: photodetector, laser was locked to a carrier-envelope-stabilized optical frequency comb (Menlo FC1500-250)). 62

Figure 5.15 The measured accumulated phase change of the entire HCF coil (layers 1-19) when the temperature was increased from 30°C to 40°C and from 40°C to 50°C. 62

Figure 5.16 The measured length-normalized accumulated phase change for N = 8, 12, and 19 (temperature change: 30°C - 40°C) (The inset shows the temperature recorded for layer 1-12). 63

Figure 5.17 The measured length-normalized accumulated phase change for N = 8, 12, and 19 (temperature change: 40°C - 50°C). 63

Figure 5.18 The measured thermal phase sensitivity of the HCF coil with the simulated results that considers layers 16-19 to be loose. 64

Figure 6.1 Key parameters of optical pulses 67

Figure 6.2 The measurement setup (PD: photo detector). 68

Figure 6.3 The measured pulse of 10 ns. 68

Figure 6.4 Schematic setup of typical EOMs and AOMs. 70

Figure 6.5 A pulse generation setup based on EOM (Laser: NKT BASIK module; PD: photodetector; EOM: electro-optic modulator).....70

Figure 6.6 EOM's output when the amplitude of RF pulse changes. 71

Figure 6.7 A pulse generation setup based on EOM and AOM (PD: photodetector, EOM: electro-optic modulator, AOM: acousto-optic modulator).....71

Figure 6.8 The pulses generated by AOM with the EOM output as comparison.....72

Figure 6.9 System setup for pulse amplification (PD: photodetector, EOM: electro-optic modulator, AOM: acousto-optic modulator).....73

Figure 6.10 Pulse at the output of AOM 260 ns (period: 76.8 μs).....73

Figure 6.11 Output power of EDFA as a function of pump current. 73

Figure 6.12 Amplified pulses with an attenuator (20 dB attenuated) applied to avoid damaging the photodetector. 74

Figure 6.13 The measured signa floor and system noise. 74

Figure 6.14 System setup for pulse amplification with AOM reducing the noise (PD: photodetector, EOM: electro-optic modulator, AOM: acousto-optic modulator). 75

Figure 6.15 Amplified pulses with an attenuator (20 dB attenuated) applied to avoid damaging the photodetector. 75

Figure 6.16 Pulses generated in the setup when EDFA works at 100 mA (here, 20 dB is attenuated to protect PD when measuring pulses from EDFA and AOM). 76

Figure 6.17 AOM's noise-reducing effect, where the noise is reduced (out of the window). 76

Figure 6.18 The proposed setup of amplifying OTDR pulses and guiding the signal back to OTDR detector (PD: photodetector, AOM: acousto-optic modulator). 78

Figure 6.19 (a) The circuit and (b) the made Tap photodetector used in Figure 6.18. 78

Figure 6.20 The observed synchronised pulses of output of the made Tap PD, RF pulse on AOM and output of AOM.....78

Figure 6.21 The trace of the photo-counting OTDR instrument (500 m SMF + 1 km SMF) is shown when the pulse is 10 ns. 79

Figure 6.22 Increased power of the amplified pulse when EDFA works at different pump current. 80

Figure 6.23 (a) 2× amplified pulse when EDFA works at 29 mA (further amplified pulses requires attenuator for detector measuring) and (b) the noise of the pulse with the AOM open window demonstrated. 80

Figure 6.24 The OTDR traces of 500 m SMF + 1 km SMF when pulse-amplification is applied with the non-amplified OTDR showing for comparison. 81

Figure 6.25 AOM window's impact. 82

Figure 6.26 Optical spectrum of non-amplified and the amplified pulse. 82

Figure 6.27 The proposed setup of amplifying OTDR pulses and guiding the signal back to OTDR detector with a bandpass filter applied (PD: photodetector, AOM: acousto-optic modulator, BPF: bandpass filter). 83

Figure 6.28 Optical spectrum of the amplified pulse and the filtered (a) 55 mA (b) 200 mA. 83

Figure 6.29 Bandpass filter's impact on noise floor of OTDR trace of 500 m SMF + 1 km SMF (here, peak at 500 m appears due to the reflection at the SMF-SMF connector). 84

Figure 6.30 Setup based on two EDFAs. 84

Figure 6.31 Comparison in the performance of OTDR traces of 500 m SMF+1 km SMF between OTDR, amplified OTDR (one EDFA) and amplified OTDR (two EDFAs). 85

Figure 6.32 Optical spectrum of FOTR OTDR pulse. 86

Figure 6.33 Pulse Power of the system in Figure 6.30 (the power of -26 dBm at 0 mA is the power from the OTDR). 86

Figure 6.34 The OTDR traces of a 1 km SMF for FOTR based system. 87

Figure 7.1 Experimental system showing the detail of the implemented Pulse Amplification unit (a) and detail of SMF-HCF light coupling (b). PD: photodetector, AOM: acousto-optic modulator. 89

Figure 7.2 (a) The amplified pulse with the non-amplified shown for comparison (b) The measured backscattering using 10 ns pulses of the 509-m SMF and 885-m NANF with the FOTR-203 both without and with the Pulse Amplification unit. 90

Figure 7.3 Backscattering coefficients obtained from measurements with the Pulse Amplified FOTR-203 and with a high sensitivity LOR-200 OTDR without Amplification unit. 91

Figure 7.4 (a) The measured backscattering of a DNANF (b) The spatial resolution measured at the full width at half maximum (FWHM). 92

Figure 7.5 Illustration of the SMF-HCF connection for low loss and low back-reflection. ..93

Figure 7.6 The diagram of the experimental setup for HCF evacuation and monitoring. ..94

Figure 7.7 Backscattering distribution during evacuation. 94

Figure 7.8 Monitoring of the 55 m +112 m HCF. 95

Figure 7.9 Monitoring of the 55 m +112 m HCF after sealing the connection using glue. .95

Figure 7.10 Knudsen number based gas flow regimes. 96

Figure 7.11 Knudsen number as a function of pressure (gas: nitrogen; temperature: 25 °C) 97

Figure 7.12 The calculated distributed normalized pressure as a function of dimensionless time of (a) air-evacuation and (b) air-filling. 98

Figure 7.13 The comparison of pressure distribution between the measured results and the model in [128]. 98

Figure 7.14 The considered core size in model. 99

Figure 7.15 The comparison of pressure distribution between the measured results and the model in [128] when the core size is considered to be 70%, as suggested in [129]. 99

Figure 7.16 Monitoring of the HCF filling. 100

Figure 7.17 Pressure change during HCF filling (solid line: model; star: experiment). 100

Figure 7.18 (a) Experimental setup, with the insets showing the SMF-HCF connection and the cross-section of the used HCF sample (b) the measured backscattering trace of the SMF+HCF (at atmospheric pressure). 101

Figure 7.19 Monitoring of the 150 m HCF of up to 49 days. 102

Figure 7.20 The comparison of pressure distribution between the measured results and the model in [128] when consider the core size to be 70%, as suggested in [129]. 103

Figure 7.21 Experimental setup of monitoring the end facet contamination. 103

Figure 7.22 The monitored end facet reflection of the HCF (a) OTDR trace (b) The increased reflection based on HCF's backscattering level. 104

Figure 7.23 Evolution of contamination on the cleaved surface of a HCF [132]. 104

Figure 7.24 Setup for OTDR measurement performed by launching from the OTDR SMF pigtail into the HCF under test (a) from the SOP and (b) from the EOP end. Inset: cross section of NANF type HCF; (C) the obtained two OTDR traces. 105

Figure 7.25 Set-up for calibrating the OTDR system (a) and to measure powers of Pa (b),and Pb (c) for evaluating the quantities of $PEOP0$ or $PSOP0$. 107

Figure 7.26 The measured backscattering from the SMF pigtail and Fresnel reflection (attenuated by 40 dB) at its end. The measured Fresnel reflection (-54.5 dB) is at the level of -37.2 dB. Then SMF pigtail backscattering is evaluated to be -70.3 dB. Given pulse width of 10 ns, this corresponds to backscattering coefficient of -70.3 dB/m. 109

Figure 7.27 The calibration of the measured backscattering from the SMF pigtail and Fresnel reflection (attenuated by 40 dB) at its end. 109

Figure 7.28 The calibrated backscattering traces when launching light from both SOP and EOP for HCF-1. 111

Figure 7.29 (a) The accumulated loss for HCF-1 and its polynomial fit (red dashed line) and (b) Attenuation coefficients. 111

Figure 7.30 The obtained backscattering coefficient for HCF-1. 112

Figure 7.31 The calibrated backscattering traces when launching light from both SOP and EOP for HCF-2. 112

Figure 7.32 (a) The accumulated loss for HCF-2 and its polynomial fit (red dashed line) and (b) Attenuation coefficients. 113

Figure 7.33 The obtained backscattering coefficient for HCF-2 in standard bobbin (red) and large bobbin(blue). 113

Figure 7.34 The calibrated backscattering traces when launching light from both SOP and EOP for HCF-3. 114

Figure 7.35 The accumulated loss for HCF-3 and its polynomial fit (red dashed line). 114

Figure 7.36 (a) The obtained backscattering coefficient for HCF-3 (sub-atm) and (b) the calibrated backscattering trace at the EOP. 115

Figure 7.37 The extracted backscattering coefficient (at SOP) of three samples with the value predicted in [46] shown for comparison (HCF-3 has been compensated to 1 atm). 116

Research Thesis: Declaration of Authorship

Print name: **Xuhao Wei**

Title of thesis: **Characterisation of Hollow Core Fibres**

I declare that this thesis and the work presented in it are my own and has been generated by me as the result of my own original research.

I confirm that:

1. This work was done wholly or mainly while in candidature for a research degree at this University;

2. Where any part of this thesis has previously been submitted for a degree or any other qualification at this University or any other institution, this has been clearly stated;

3. Where I have consulted the published work of others, this is always clearly attributed;

4. Where I have quoted from the work of others, the source is always given. With the exception of such quotations, this thesis is entirely my own work;

5. I have acknowledged all main sources of help;

6. Where the thesis is based on work done by myself jointly with others, I have made clear exactly what was done by others and what I have contributed myself;

7. Parts of this work have been published as: [see List of Publications]

Signature:…… Date:……

Acknowledgements

Upon completing my thesis, my journey through the Ph.D. program is coming to an end. The past four years have been a cherished chapter, filled with memories shared with friends and family, an experience made even more profound by the disruptive impact of COVID-19.

I extend my heartfelt gratitude to Prof. Radan Slavík for his invaluable guidance throughout my entire Ph.D. studies. His support is instrumental in my successful completion.

I express my appreciation to Prof. Francesco Poletti for his kind support and exceptional work on the Hollow Core Fibres.

A special thanks goes to my colleagues in the ORC. Collaborating with such brilliant guys in the field of HCFs—Bo, Meng, Zitong, Nicolo, Dmytro, Irene, Win, Bertalan, Laura, Austin, Tom, Leonard, Greg, and many others, including Natalie, Eric, Yong, David, Peter, Yongmin—has been an amazing experience.

I would like to express my sincere gratitude to examiners, Peter and Matej, for their valuable feedback and constructive comments.

My gratitude goes to everyone who supported me in their ways during the lockdown, helping me navigate through this challenging period.

I also want to acknowledge Ziwei for the always support in work and thesis-writing.

My final thanks are reserved for my family, whose unwavering support has been a constant and meaningful force in my journey.

Definitions and Abbreviations

AOM……..……..Acousto-Optic Modulator

ARF…….…….Antiresonant Fibre

ASE…….…….Amplified Spontaneous Emission

DAQ……..……Data Acquisition Device

DNANF..……..Double Nested Antiresonant Nodeless Fibre

EOM…….Electro-Optic Modulator

EOP……..End of Pull

FEA……..……...Finite Element Analysis

FPs……Fabry-Perot Interferometers

FUT…….……..Fibre Under Test

GRIN……..……..Graded-Index Fibre

HCF……..Hollow Core Fibre

MFA……..Mode-Field Adapter

NANF……Nested Antiresonant Nodeless Fibre

OFDR……..Optical Frequency Domain Reflectometry

OTDR……..Optical Time Domain Reflectometry

PBGF……..……..Photonic Band Gap Fibre

PD……..Photodetector

PDE……..…….Partial Differential Equations

FSR……..……..Free Spectral Range

QAD……Quadrupolar

SBS…….Stimulated Brillouin Scattering

SMF……..……..Single Mode Fibres

SNR……..……..Signal To Noise Ratio

SOP……..Start of Pull

SRS……..Stimulated Raman Scattering

TEC……..Thermal Expansion Coefficient

UV…….……Ultraviolet

Chapter 1. Introduction

1.1 Motivation

By guiding light through air/vacuum, Hollow core fibres (HCFs) have demonstrated several extraordinary properties [1-3], including low loss [4-6], as well as low latency [7], ultralow non-linearity [8], ultralow backscattering [9], ultralow thermal sensitivity [10], and the exceptional ability in high power delivery [8]. These features make HCFs highly promising in not only replacing traditional solid core single mode fibres (SMFs) in applications such as long-haul telecommunications [11-13], and fibre sensing [14], but also opening new opportunities, such as light-gas interaction [15], that conventional fibres cannot achieve. In recent years, the most promising HCFs, namely the (Double) Nested Antiresonant Nodeless Fibres (NANFs/DNANFs), have achieved remarkable advancements that the lowest reported loss is 0.174 dB/km in the C-band, making it the lowest among all HCFs and comparable to conventional telecoms fibres [4, 16]. Not only have HCFs demonstrated their advantage in more and more applications, this significant progress has led to early-stage commercialization [17].

For conventional fibres such as SMFs, development of characterisation methods has played a crucial role in their success. This is because characterisation contributes in various aspects, including the quality assurance (e.g., attenuation), performance improvement (e.g., coating design), improving the understanding of their properties for practical applications (e.g., environment stability), maintenance of deployed cables, contribution to novel fibre designs for an improved performance and more. However, despite significant progress made over the last two decades, characterization has, unfortunately, not kept pace with the rapid advancements in HCFs [18].

For example, the impact of coating on the performance of conventional optical fibres has been extensively studied and well understood. However, this understanding does not fully extend to HCFs, especially when considering that these influences can be markedly different. For instance, in terms of thermal sensitivity, HCFs often suffer dominantly from thermal expansion, which is very different to conventional fibres. Another example pertains to distributed characterization, which is considered one of the most powerful characterization methods developed for optical fibres. However, when dealing with new emerging HCFs (NANFs/DNANFs), the application of backscattering-based distributed characterization becomes challenging, which is primarily because the backscattering in HCFs can be extremely low. As a result, we face delays in gaining a comprehensive understanding of their properties, consequently hindering our ability to contribute effectively

to their growth and advancement. This situation emphasizes the urgency to explore novel characterization methods that would allow us to gain a better understanding of the properties of HCFs, which becomes the main target of this thesis. This, in turn, will unlock their full potential in various applications and, hopefully, accelerate the process of large-scale commercialization. Throughout this thesis, we focus on using the state of art HCFs-NANFs/DNANFs, occasionally we just refer to them as HCFs.

1.2 Research focus of the thesis

In this thesis, we will present our studies on the characterization of HCFs (NANFs/DNANFs) through two main subtopics.

1.2.1 Thermal Sensitivity of Coated HCFs (Topic-1)

Thermal phase sensitivity of an optical fibre (phase of the light traveling through a fiber changes with temperature) is a limiting factor for applications of most fibre interferometers and their applications, e.g., in laser frequency stabilization and fiber sensing, where cross sensitivity to temperature limits the achievable performance [19-25]. Despite the expected low thermal phase sensitivity in HCFs, the existing thermal sensitivity is still a problem, and thus it is necessary to study the mechanisms in detail and meanwhile, explore new strategies to reduce or even completely null this thermal phase sensitivity.

The accumulated phase of the signal propagating through an optical fibre is:

$$\varphi = 2\pi n_{eff} L/\lambda, \tag{1-1}$$

where *L* is the fiber length, n_{eff} is the effective refractive index of the fundamental mode, and λ is the light wavelength in vacuum. Consequently, the fiber's thermal phase sensitivity, normalized to fiber length, can be calculated as:

$$S_{\varphi} = \frac{1}{L}\frac{d\varphi}{dT} = \frac{2\pi}{\lambda}\left(\frac{dn_{eff}}{dT} + \frac{n_{eff}}{L}\frac{dL}{dT}\right). \tag{1-2}$$

In equation 1-2, the first term quantifies the effect of effective index change caused by thermo-optic and elasto-optic effects, and the second term quantifies the effect of fiber elongation [26, 27].

For standard SMFs, that guide light through a glass core, the first term contributes about 95% (45 rad/m/°C) to the total thermal phase sensitivity, mostly due to the thermo-optic effect in silica glass. The second term that accounts for 5% is then 2.4 rad/m/°C caused by the thermally-induced elongation [26, 27]. Therefore, the strategies to reduce SMFs thermal

phase sensitivity focus on reducing/compensating the thermo-optic effect. Such techniques include core doping [28], and application of specialty coatings [29].

As more than 99% of the light propagates in the thermally-insensitive air, the first term in Eq. 1-2 is usually negligible in HCFs, which shows a dramatically low thermal sensitivity (up to 18 times lower than SMFs) [10, 30], which has been also demonstrated in some applications, such as FOGs and Fabry-Perot interferometers (FPs) [14, 31-33].

The thermal phase sensitivity of HCFs is believed to be mainly coming from the thermal expansion and, especially of the used coating whose thermal expansion ability is more than 100 times bigger than silica glass [26, 30, 34], so the straightforward method on reducing their thermal phase sensitivity would be to reduce coating thickness or even to remove coating. For example, Ref. [30] studied this contribution theoretically and concluded that an acrylate coating can dramatically increase the thermal phase sensitivity of HCFs, and this influence decreases as the coating gets thinner, which was later experimentally demonstrated in [30, 35]. Zero thermal phase sensitivity was achieved for bare HCFs, which, however, is applicable only at ultralow temperature of -71°C, far below the preferred room temperature [36].

The fact that fibres are usually applied with coating for either protection or easy handling makes it practically essential to study for coated fibres or coating's impact in detail in order to explore strategies to eliminate the thermal phase sensitivity, while hopefully working at room temperature. As mentioned above, the coating contributes to thermal phase sensitivity by both elongation (thermal expansion) for both HCFs and SMFs and the elongation induced refractive index changes for SMFs only (elasto-optic effect), as this is negligible in HCFs. This interesting difference makes the coating's influence on the thermal phase sensitivity of HCFs significantly less complex than SMFs. Furthermore, coating's influence is significantly more prominent in HCFs that have a very small inherent thermal sensitivity. Thus, HCF is a better system for studying coating's mechanical properties as compared to SMFs. This is often of an interest, as the coating properties on a drawn fibre can differ from those measured on coatings prepared as thin films, as often listed in data sheets [37, 38]. These differences can arise due to variation in the degree of curing applied to the coating, including factors such as curing time, temperature, and the dose of irradiating energy. For example, the thermal sensitivity of a measured coated HCF can be as much as two times different from the value calculated using data from the datasheet, indicating a significant change in properties [27].

Here, the aim is to investigate the thermal phase sensitivity of coated HCFs, with the primary goal of gaining a better understanding of the coating's impact and identifying solutions to mitigate it. Since zero thermal phase sensitivity for coated HCFs operating at room temperature has not yet been reported, this study seeks to achieve this.

To this end, a method has been proposed [39]. It is based on winding the HCF on a spool made of material with near-zero thermal expansion coefficient (TEC). This could potentially enable zero HCF thermal phase sensitivity at room temperature, but the demonstration showed only 3 times reduction than HCF itself. Although promising, the coil adds weight and volume, which are undesirable in space-constrained or weight-sensitive applications. Another method was also demonstrated that zero thermal phase sensitivity is possible for coated HCFs that used the escaping air to compensate the elongation. This, however, again, seems not possible at room temperature [40].

In the first part of my thesis, the influence of the coating on HCFs' thermal phase sensitivity is studied in detail, confirming that coating contributes to the overall thermal phase sensitivity, but most interestingly, it introduces significant relaxation effect. This effect causes a change in the phase of light once the temperature stabilizes, which is confirmed by simulations. A novel method is then proposed for achieving zero thermal phase sensitivity by using standard coated HCFs. As expected, this approach enables a ultralow thermal phase thermal sensitivity at room temperature, as demonstrated via both simulation and experiment.

1.2.2 Distributed characterisation of HCFs (Topic-2)

Breakthrough demonstration of a successful measurement of ultralow backscattering in HCFs during my 2nd year of PhD studies caught our attention, in particular in its potential to revolutionize HCF characterization. Therefore, after discussion with my supervisory team that was very keen on pursuing this new research direction in the fast-developing field of HCFs, I re-focused in the 2nd part of my PhD work on the distributed characterisation of low-loss HCFs as my second sub-topic of HCFs characterisation.

For traditional fibres, backscattering based distributed Optical Time Domain Reflectometry (OTDR) or Optical Frequency Domain Reflectometry (OFDR) has been widely used for identifying properties and defects along the fibre [41, 42]. This technique is proved to be very advantageous due to the fact that it allows distributed characterisation by accessing to only one end of the fibre (e.g., installed fibre cables). Subsequently, applying this technique to HCFs is then becoming urgent for HCFs researchers and users. However, HCFs' extremely low backscattering makes it very challenging to characterise using commercial instruments due to their relatively low sensitivity, especially when high spatial resolution is required.

By using a highly-sensitive custom-built optical frequency domain reflectometer (OFDR) [9], the first backscattering measurement was demonstrated experimentally in 2020 that the fundamental backscattering, caused by the glass surface, is more than 40 dB lower than that of a SMF, as shown in Figure 1.1. However, the air induced backscattering was not

demonstrated with this custom-built system as the air induced thermal Doppler broadening is beyond the system's measurement bandwidth, which limits the application for the desired widely HCFs characterisation, especially when the air backscattering is of interest. For newly-drawn HCFs, they are easily filled with air at pressures as low as 0.2 atm, even when ignoring the pressure gradient induced ingress during the necessary tests [43]. Although it can be evacuated, the evacuation of a HCF is still very time-consuming with current techniques (e.g., weeks for hundreds meters fibre [44]). Besides, OTDR can be used for gas pressure distribution monitoring, e.g., in gas flow or HCF evacuation study, and potentially for distributed sensing [45]. This strongly suggests the non-coherent OTDR technique is more preferred for HCFs' distributed characterisation. Promisingly, the result in Ref [9] serves as an important guidance to apply the technique of OTDR to HCFs.

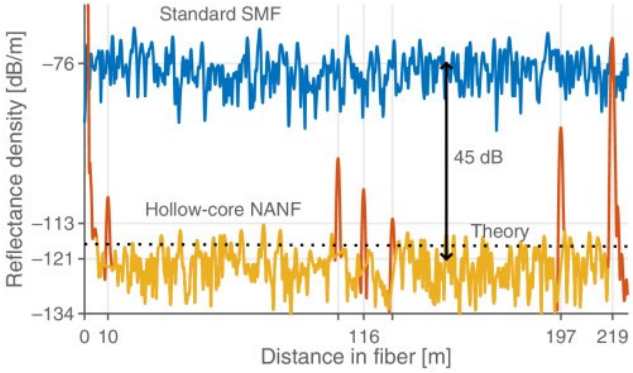

Figure 1.1 The measured backscattering in a NANF [9].

Soon after the experimental demonstration of ultralow backscattering in HCFs, the theoretical studies found that backscattering can be more than 10 dB higher than the fundamental backscattering when the fibre is filled with air at atmospheric pressure [46]. This expectation led to the first backscattering measurement in air filled HCFs using OTDR technique [47]. Although it used a highly sensitive photon-counting OTDR instrument (LOR-200 from Luciol, Switzerland), the spatial resolution was only 15 m (100 ns pulses) [48]. Furthermore, it takes very long time (few hours to reduce noise) to obtain a decent curve, which is not suitable for a fast measurement to reduce the gas ingress in as-drawn fibres, for monitoring the gas filling or fibre drawing.

Therefore, I target to build a high performance OTDR system using standard detectors, with high sensitivity and high spatial resolution. This system is expected to characterise in detail of various HCFs in various conditions, e.g., air-filled and evacuated, as well as study the dynamics of HCFs evacuation.

Due to the limitation of current fabrication technique, the microstructure in a HCF can vary significantly along the drawn fibre. This non-uniformity, together with the air distribution, impacts the distribution of backscattering coefficient, resulting in OTDR traces of HCFs being influenced not only by fibre loss but also by variations in the backscattering coefficient. As a result, obtaining useful data from OTDR traces becomes challenging. To solve this

discrepancy and investigate the longitudinal properties of the new made low loss HCFs, this technique is extended to acquire the loss distribution, and backscattering coefficient distribution by applying bi-directional OTDR analysis. This is expected to not only show the fibre loss distribution, in good agreement with cutback loss, but also enable a better understanding of uniformity of the HCFs, and potentially provides feedback to fabricators for drawing long uniform and low loss fibres. Compared to the destructive cross-section imaging method, this could potentially serve as a non-destructive tool for monitoring the fibre drawing process, as real-time tracking of the backscattering signal from a drawing fibre enables the monitoring of fibre loss and uniformities of HCFs microstructure so that operators can make real-time adjustments as needed.

1.3 Thesis Objectives

The objective of this thesis is to develop novel characterisation methods for recently emerging low loss HCFs (NANFs/DNANFs).

1.3.1 Thermal Sensitivity of Coated HCFs

In this section, an in-depth investigation is conducted on the impact of coating on thermal phase sensitivity of HCFs. A novel approach is developed to comprehend the distinctive behaviour introduced by the coating, as extensively discussed in Chapter 4.

Building upon the insights gained from the coating analysis, a thermally insensitive HCF coil is designed and discussed in Chapter 5. The novel coil aims to mitigate thermal expansion, offering enhanced stability of ultralow thermal sensitivity in relevant applications.

1.3.2 Distributed characterisation of HCFs

An OTDR system with high spatial resolution and high sensitivity is built for the distributed characterisation of HCFs, as will be discussed in Chapter 6.

Based on the built system, a comprehensive series of characterisation experiments is performed on various HCF samples, and these investigations delve into the distributed properties, as shown in Chapter 7.

1.4 Thesis outline

This thesis proceeds with a background in Chapter 2, which covers the basic information of HCFs, with a particular focus on the state of the art NANFs/DNANFs, a type of HCFs we are using throughout the entirety of this work. We firstly discuss the developing history of HCFs, including their guiding mechanisms, and their unique properties compared to SMFs.

As we study coating's impact on their thermal sensitivity in Chapter 4, HCFs fabrication is also examined and discussed.

Chapter 3 introduces all the characterisation methods that will be used in the thesis. Firstly, the numerical analysis tool of COMSOL Multiphysics for studying HCFs thermal sensitivity and the characterisation method are discussed. Finally, the principle of OTDR is discussed, including the backscattering mechanism, working principle, and key parameters.

Chapter 4 presents the coating's effect on thermal phase sensitivity of HCFs. This chapter is in close cooperation with my colleague who conducted the experiments on measuring the thermal phase sensitivity of HCFs, including dual-coated and thinly coated HCFs. My work on simulation via COMSOL Multiphysics is discussed based on the comparison to the experimental results. From the experimental results, we observe a new "memory" effect-stress relaxation when temperature is stabilized after a change, where we propose a novel method that helps us gain significantly better understanding of the coating's behaviours. This chapter ends with my fitting on the coating's key parameters in terms of thermal behaviours. The fitted data, when compared with that supplied by coating manufacturer, is deemed more useful for researcher, e.g., to better predict the thermal behaviour of coated fibres.

Benefiting from the understanding of coating's behaviour in Chapter 4, Chapter 5 shows a novel method on reducing the already low thermal sensitivity of HCFs to be close to zero. This is based on the interplay between fibre coating and silica. We start with a toy model to illustrate the stress distribution in a coated HCF coil where exists negative thermal expansion in inner layers due to the compression of outer layers that have positive thermal expansion, followed by a series of simulations on the thermally insensitive HCF coil's key parameters to enable us to design it properly. Finally, the characterisation experiment on the made coil is presented and the summary is discussed.

Chapter 6 presents our experiments on building a high-sensitivity OTDR system for characterising HCFs. Since high-power pulses are the key for achieving high-sensitivity OTDR system, we firstly discuss the characterisation technique for pulsed laser, the commercial EDFAs based pulse amplification, and the single-noise ratio improving methods. After that, we propose our highly sensitive OTDR system via building a pulse-amplification unit based on commercial OTDR instruments. The built system is then able to improve the sensitivity significantly.

In Chapter 7, we firstly show its capacity to measure the weak backscattering in HCFs, with comparison to that obtained by highly sensitive photon-counting OTDR and then the experiments on various characterisations for HCFs are discussed. This covers not only characterisation of the air-filled HCFs, but also the even more challenging measurement on

the evacuated HCFs and the evacuation monitoring. Furthermore, since the microstructure in a HCF varies along the length, the direct OTDR trace usually gives a loss with huge uncertainty and even negative value, which is not the case for SMFs as its slope normally indicates the loss. To solve this problem, the OTDR analysis is applied based on two direction measurements, which shows the capacity of deducing not only the loss, but the backscattering coefficient variation. The acquired result of the loss is in a good agreement with cut-back loss provided by the fibre fabrication group. The backscattering coefficient variation suggests the fibre uniformity can vary significantly and needs improvement. Its origin seems complicated, which requires further investigation, and some conclusions are discussed based on these primary results. We conclude by the future plan.

Finally, Chapter 8 discusses the conclusions from all of this work and offers a few possibilities for future work.

Chapter 2. Background: Introduction of Hollow Core Fibres

In this chapter, we discuss the basics of Hollow Core Fibres that will be used throughout the whole thesis. This includes the developing history, main guiding mechanisms, unique features and their opportunities, fabrication and coatings followed by a brief summary.

2.1 Historical perspective

Ever since Charles Kao reported his research on optical waveguide in 1960s [49], optical fibres have developed so quickly and have been seen as the basis of the information age. All conventional optical fibres guide light in a solid core through the effect known as total internal reflection where the refractive index in the core is higher than in the cladding region. This made people think of replacing the solid core with a hollow core so that the loss caused by the materials (scattering loss and absorptive loss) can be eliminated. Obviously, new guiding mechanisms are then required to confine the light inside a hollow core, which is impossible with the total internal reflection. Various methods had been proposed, but it was not until the 1990s that this idea started to seem realistic. In 1991, Philip Russell proposed the idea of photonic-crystal effect, which is created by a periodic array of wavelength-scale holes that creates a low index cladding [50]. This microstructure was proved to be able to confine light into a solid core [51]. Soon after, the first hollow core fibre (HCF) was born, which has a cladding named as photonic band gap (HC-PBGF or simply PBGF) that could confine the light inside a hollow core [1].

Unlike solid core fibres, most of the light propagates in air instead of the glass, which makes them suffer dramatically less from material induced loss, and thus they are expected to achieve ultralow loss. Such efforts had been made in the next few years that 13 dB/km loss was achieved for a seven-cell PBGF in 2002 [52] and then Russel's group further reported a loss of as low as below 2 dB/km in a 19-cell PBGF two years later [53] and a 1.2 dB/km loss was claimed soon after that. This was seen as a huge achievement for PBGFs (lowest loss in HCFs then) but after that progress became very challenging, which is believed to be mainly limited by the strong scattering loss at the air-glass surfaces (intrinsically due to frozen in thermodynamic fluctuations) [54, 55]. The developing history of PBGFs is shown in Figure 2.1.

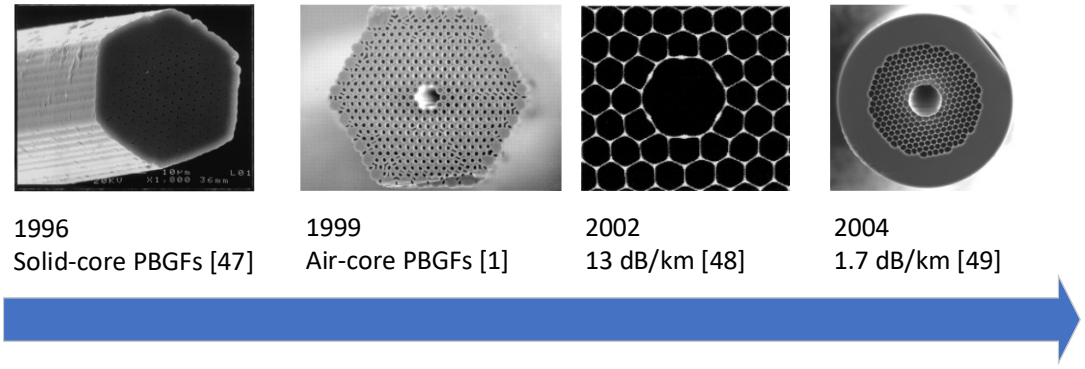

Figure 2.1 Key achievements of PBGFs.

Meanwhile, many other methods of confining light in a hollow core have been tested and one of the most promising guiding mechanisms is achieved by the antiresonant layer between a hollow core and the surrounding cladding. Researchers at the University of Bath found that it is not the reflection but the prevention of light coupling between core and cladding modes that contributes to the light guiding, which was soon proved by a Kagome fibre with ice-cream-cone shaped hypocycloid facing into the hollow core [56-58]. This opened the door into a new types of HCFs-hollow-core antiresonant fibres (HC-ARFs or simply ARFs). Walter Belardi then presented in numerical simulation that the negative curvature helps light confinement and he further proposed a method based on a single layer of tubes inside a hollow tube [59, 60]. Later, he modified the design by introducing a smaller tube (additional antiresonant elements) inside each tube in the negative-curvature layer, which can effectively reduce the loss by preventing the light from coupling into the cladding [61].

Another design was proposed in 2014 by Poletti at the University of Southampton that is NANF, where he analysed that the loss (leakage, surface scattering and bending) can be reduced further to be even below that of conventional solid fibres by removing the nodes where tubes touched [16]. This design is promising as it not only has the combined characteristics of the low loss and bend robustness in PBGFs and the wide bandwidth and low modal overlap with cladding in ARFs, but also can be effectively single mode guided, which is preferred for long-haul data transmission.

The rapid progress in the following years has made NANF undoubtedly one of the most promising alternatives to conventional solid core fibres. In 2018, 1.3 dB/km at 1450 nm was achieved, which is an important achievement as it is the first HCF to be below the 1.7 dB/km PBGF in 2004 [62]. Just one year later, the loss was reduced twice to be 0.65 dB/km [63] and further reduced to 0.28 dB/km in the C+L band in 2020 [64] and 0.22 dB/km at the edge of L band (1625 nm-1640 nm) [65]. Very recently in 2022, the loss record for HCFs was broken again by the NANF based modified design of DNANF, where one extra nested tube was added to each nested elements of NANFs [4]. This reduces the confinement loss that leads to the 0.174 dB/km loss in C band (comparable to conventional solid core fibres [66]),

representing the lowest loss in all HCFs that have been reported. Furthermore, the achieved 0.22 dB/km loss in O band is even lower than the fundamentally possible loss in a solid core fibre. The key achievements for ARFs are listed in Figure 2.2. Since almost all of the key progresses on NANFs/DNANFs were made in ORC, at the University of Southampton, we have access to these fantastic low-loss HCFs.

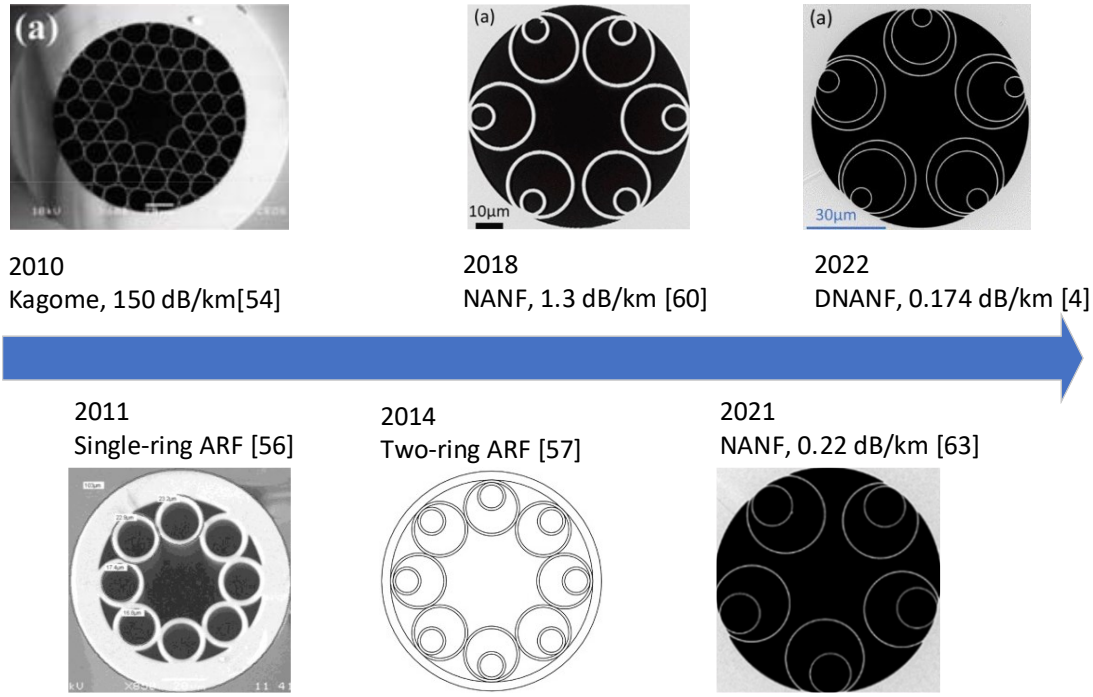

Figure 2.2 Key achievements of ARFs.

2.2 Guiding principle

2.2.1 PBGFs

For the PBGFs, the light is restricted to hollow core surrounded by the periodic holey dielectric cladding region, which forms the photonic bandgap effect. When light is launched on the structure, it experiences successive reflections and transmissions at all layers. The guiding mechanism can be simply explained in Figure 2.3.

When it is 1-D structure (Figure 2.3 (a)), consisting of material-1 (refractive index: n_1) and material-2 (refractive index: n_2) with a periodicity of Λ, the light undergoes constructive interference when the Bragg condition:

$$N\lambda = 2\Lambda sin\theta. \qquad 2\text{-}1$$

is satisfied. This allows the light at λ with a wavelength range of $\Delta\lambda$ to be totally reflected when it is injected within $\Delta\theta$ at θ.

Here, λ is light wavelength, and θ is the injection angle. As shown in Figure 2.3 (b), light will not be able to travel in any direction when the angle for reflection is large enough and thus, it can be confined in a hole within the structure.

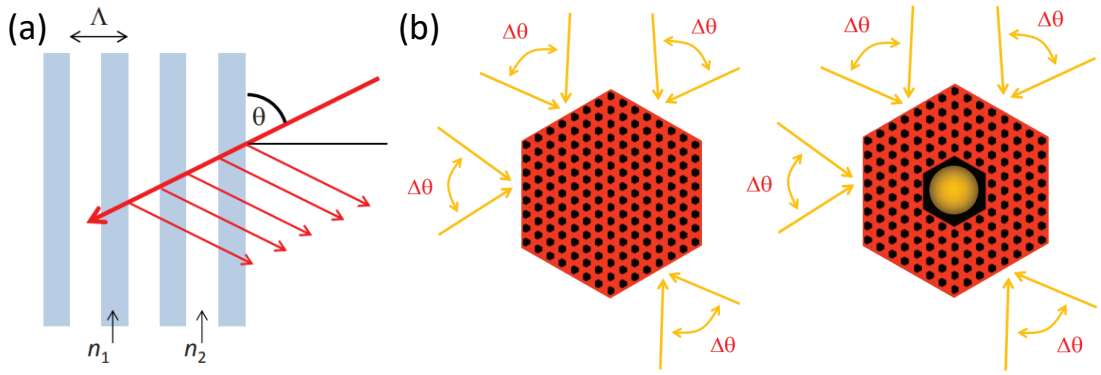

Figure 2.3 PBG Guidance (a) 1-D; (b) 2-D.

2.2.2 ARFs

ARFs guide a light through the coherent reflection in the radial direction, where the reflections from the cladding interfere constructively (resonance) at certain wavelengths. Light escapes when they are at resonance and is confined into the core when at antiresonance. Considerable theoretical efforts have been made to study the guiding mechanism [67, 68], with the ARROW model being one widely used example [69], as shown in Figure 2.4. The core is surrounded by two high index (n_2) and low index (n_1) cladding layers, each layer can be seen as a resonator. In the ARROW model, the wavelengths at resonance (high loss) are given by:

$$\lambda_m = \frac{2t}{m}\sqrt{n_{glass}^2 - n_{air}^2} \approx \frac{2t}{m}\sqrt{n_{glass}^2 - 1}. \qquad 2\text{-}2$$

Where m is 1, 2……, and t is the thickness of each layer. n_{glass} and n_{air} are the refractive index of the air core and glass microstructure. Therefore, the 1st window (m = 1) has the biggest bandwidth when we consider the thickness of the layers are the same. By decreasing the thickness, the operational windows can be adjusted, which indicates the thickness is a key parameter in fabricating ARFs. The transmission window is like that shown in Figure 2.4.

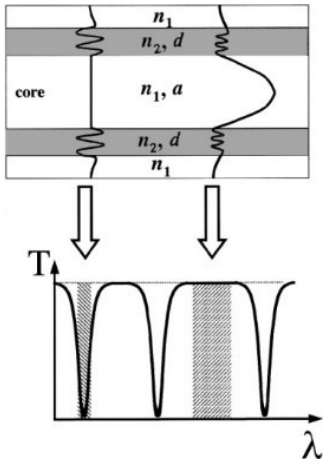

Figure 2.4 ARROW model [28] and its transmission spectrum (bottom) [69].

2.3 Loss in HCFs

In conventional fibres, which usually do not suffer from confinement loss, the minimum achievable loss is determined by the fundamental scattering and absorption processes in the high-purity glass [70]. In contrast, HCFs, which confine light in air, experience loss from various sources, including confinement loss, surface scattering loss, and bend loss, among others. Depending on the fibre type, either confinement loss or surface scattering loss tends to dominate for the above discussed PBGFs and ARFs.

All HCFs suffer from some degree of leakage. However, the guidance mechanism is crucial in determining the contribution of confinement loss to the total loss. Significant efforts have been made to gain a deeper understanding of the physical principles behind confinement loss in HCFs [55, 68, 71].

For PBGFs [72], confinement loss can be significantly suppressed to a very low level by incorporating a sufficient number of air holes in the cladding. As confinement loss is minimized, surface scattering loss, resulting from the roughness of the glass surface, becomes the dominant loss mechanism in PBGFs. This roughness is, unfortunately, inevitable because of its thermodynamic origin during the fibre drawing process.

In ARFs, adding nested tubes has proven to be very effective in reducing their confinement loss, as evidenced by the performance improvements observed across the three types of ARFs: tubular HCFs, NANFs (with one nested tube), and DNANFs (with two nested tubes), which is also mentioned in the developing history of ARFs.

Estimating surface scattering loss is complex due to the difficulty in accurately assessing the small-scale roughness of the glass surface. However, a simplified yet fairly accurate method has been adopted in various studies [16, 73, 74], which calculates the loss using the following equation:

$$SSL = \eta F(\frac{\lambda^3}{\lambda_0{}^3}). \quad \text{2-3}$$

where F is the optical power overlap of the fundamental mode with the silica glass, η is calibration factor (300 at the wavelength of λ_0 = 1.55 μm).

Because of the extremely smaller overlap (*F*) in ARFs (>99.99%), surface scattering loss is significantly smaller than PBGFs and is typically negligible compared to confinement loss. However, in today's lowest-loss HCFs (DNANF [75]), where confinement loss has been reduced to levels comparable to surface scattering loss, the latter has become increasingly significant. This highlights the importance for further investigation into surface scattering to advance the development of low-loss HCFs. One of the goals of this thesis is to collect data related to surface roughness using the OTDR technique.

2.4 Unique features and their applications

Since light is guided through air or vacuum core in HCFs instead of solid glass that forms the core in conventional fibres, the material-imposed limitations can be eliminated or significantly reduced. This enables HCFs to show several unique features, and thus leading to a host of potential opportunities.

2.4.1 Low latency

As there is no high group refractive index materials in the core, the light can be transmitted at a speed that is 1.46 times faster than SMFs, which is close to the speed of light in vacuum [7]. This low latency benefits for many applications, including 5G networks, supercomputers, autonomous systems and video conferencing, etc.

2.4.2 High thermal stability

As the light propagates in air or vacuum, HCFs suffers significantly less from the effect of thermal dependence of the glass refractive index, thus allowing more stable transmission compared to SMFs [10]. The temperature sensitivity was measured to be almost 20 times lower than SMFs, as shown in Figure 2.5. This makes HCFs particularly suitable for high-precision interferometry, time and frequency metrology [10, 14, 30, 76]. As discussed earlier in Chapter-1, the understanding of their sensitivity to temperature is one of the thesis goals.

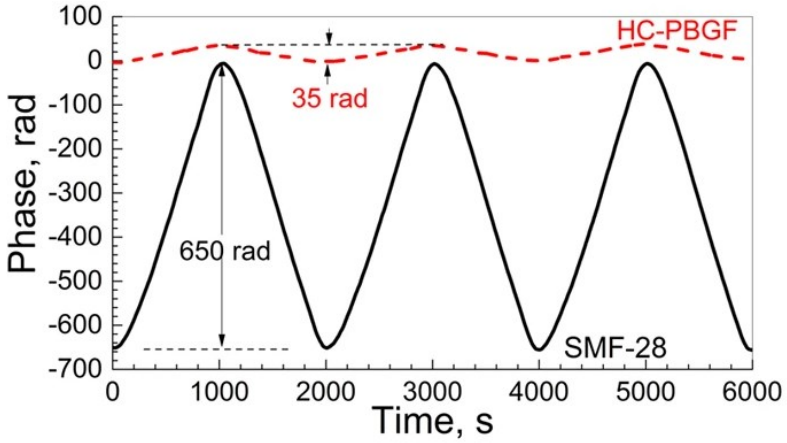

Figure 2.5 Phase change of the light through 20 m lengths of SMF-28 (solid) and HC-PBGF (dashed), where the temperature was changed by 0.5°C peak-to-peak every 1000 s [10].

2.4.3 Ultralow backscattering

The backscattering in HCFs can be extremely low in some HCFs such as NANFs. As the overlap of the light with glass microstructure cladding is extremely small (<0.1%) in HCFs, the backscattering that mostly comes from the hollow core is dramatically smaller than in SMFs, with the demonstrated fundamental level to be more than 40 dB lower than SMFs [9]. This ultralow backscattering sees its advantage in many applications relying on bidirectional propagation such as fibre gyroscopes where backscattering contributes to a source of noise, as demonstrated in [14]. However, this preferred advantage is not desirable in terms of conducting characterisation, e.g., it becomes very challenging to characterise HCFs using the widely deployed methods for distributed characterisation of conventional fibres such as OTDR, which is achieved by measuring the backscattering signal. Thus, this will be one target of this thesis of building highly sensitive OTDR system for testing HCFs.

2.4.4 High damage threshold and ultralow nonlinearities

The hollow core eliminates the solid material induced the optical nonlinearities, e.g., Kerr effect, stimulated Brillouin scattering (SBS) and stimulated Raman scattering (SRS), which often set a limitation in solid core fibres. As these effects are highly reduced by several orders of magnitudes in HCFs [8, 77, 78], which makes HCFs preferable in ultrahigh power laser delivery (for both continuous wave and high power pulsed laser), benefiting for many applications in industrial manufacturing [8, 79, 80]. The scalability of near-diffraction-limited CW power delivery in optical fibres at 1 μm (limited by SRS) is shown in Figure 2.6. It is interesting to see this performance can be further improved when the fibre is at low pressure and even in vacuum state (Chapter 7 will show experiments on monitoring the HCF evacuation). As will be discussed later in this thesis, the high damage threshold allows us

to send significantly higher power pulses into HCFs, compared to SMFs, without incurring any penalties.

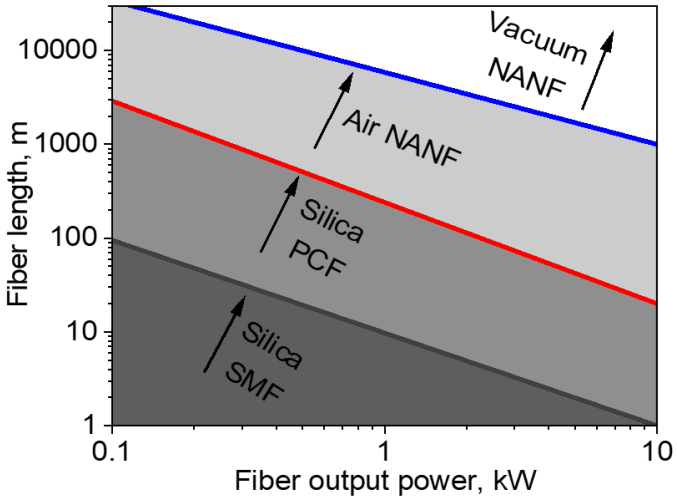

Figure 2.6 Scalability of near-diffraction-limited CW power delivery in optical fibres at 1 μm, limited by SRS (The solid lines show the maximum fibre length versus the target output power achievable for a standard silica SMF, a large-core-area silica PCF, and an air-filled NANF [8]).

2.4.5 Gas photonics

The holly nature of HCFs makes them capable of serving as an excellent platform for light–matter interactions, which can be easily filled with a diverse range of gases (e.g., acetylene, methane) and at different pressures [81]. The long interaction length provided by the low loss HCFs is usually difficulty to be achieved by methods, e.g., multi-pass cells [82]. Thus, HCFs can be used in gas sensing, including preparing gas cells for sensing or laser locking [83, 84], nonlinear optics [85, 86], supercontinuum generation [87] and macroscopic particle guidance for biomedical applications [88]. However, long HCF gas cells have significant limitations. One challenge is the time required to fill the hollow core with the gas sample. Although techniques such as pressurization and drilling side-holes can accelerate the process, they often introduce trade-offs, such as reduced compactness or increased optical loss [89]. Using large-core HCFs can help reduce the filling time, but they requires careful connection with SMFs due to the mismatch in mode-field diameters [90]. Furthermore, strong Fresnel reflections may cause parasitic Fabry–Perot resonances. This severely degrades gas cell performance, which can be suppressed using techniques such as angled connections [91].

2.5 Fabrication of HCFs

For the fabrication of HCFs, it usually follows a similar but improved process as traditional optical fibres: two stage stack and draw process. For the first step, capillaries and spacing

elements are stacked into a slender jacketing tube according to the fibre design and then fused and drawn into canes. The cane is then inserted into a thicker jacket tube to form the final preform. After a preform has been made, the next step is to draw the preform into a fibre, which is conducted by lowering the preform into the drawing furnace with high temperature, where the glass softens and is drawn into final fibre under tension. The fibre drawing process for ARFs is shown in Figure 2.7.

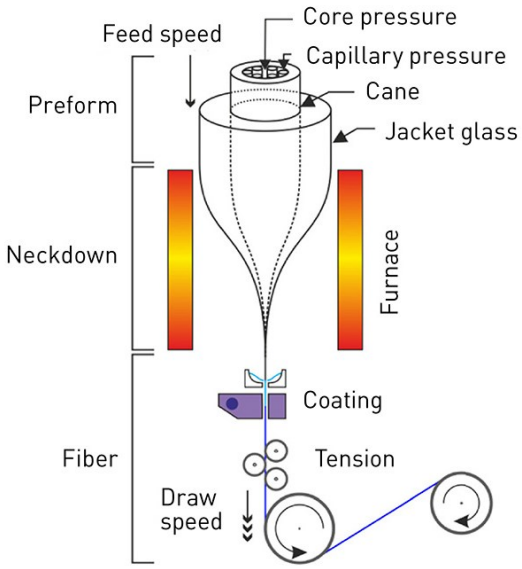

Figure 2.7 Fibre drawing process for ARFs [92].

To take ARFs in [92] for example, there are seven silica capillaries surrounding the central air core, which are stacked and fused inside a jacket tube and drawn to canes. During fibre drawing, not only the surface tension, but the careful control of the hollow regions of the microstructure is specially required, in which gas pressures in hollow core and capillary are independently controlled so that the desired fibre geometry can be precisely maintained. As we may notice, the coating application is followed once fibre is newly drawn in order to provide immediate protection for the fragile fibre, which suggests the practical importance of coating for HCFs. The detailed study on coating's impact on HCF's thermal stability performance will be discussed in Chapter 3.

2.6 Fibre coating

Since the new drawn fibre is very fragile, coating is primarily used to provide mechanical protection. Optical fibres must be coated for applications, e.g., telecommunications, with the reason that moisture and stress can cause microscopic flaws in the glass to propagate, eventually resulting in fibre failure. In addition, proper coating design contributes to a smaller signal-attenuation by reducing the micro-bending loss of optical fibres and the loss, otherwise, would never be as low as it is today [93, 94].

Over the past several decades, many types of optical fibre coatings have been studied. Among various coating materials developed, such as blocked urethanes, solvent-based lacquers, and silicone rubbers, acrylate coatings have been extensively used in commercial fibres with only a few limited exceptions since 1980s. Their wide use is thanks to their relatively low cost, ability to be cured at high speed using ultraviolet (UV) light, excellent adhesion to glass surface, low moisture absorption, low hydrogen generation, etc [93, 94].

There are usually two coating layers in current fibres: a soft inner coating, and a hard outer coating. This dual layer coating is more effective than a single coating in providing lower micro-bending loss. As reported in [95, 96], micro-bending loss could be reduced by shielding the fibre from outside forces by using a soft inner coating and the outer coating protects the inner coating against mechanical damage.

The primary coating should have a higher refractive index than glass (to eliminate light propagating in the fibre cladding) and while having good adhesion, it should have a minimum bonding to the glass surface so that the coating can be stripped easily for splicing and connecting. Since optical fibres could be also exposed to low temperatures, it is necessary for the primary coating to have a low glass transition temperature, ensuring it is in the soft rubbery phase (with small Young's modulus) over the full operation temperature range.

For the outer/secondary coating, it is a hard coating with a high Young's modulus, which is achieved by using an acrylate with the glass transition temperature above the temperature operation range. This ensures this coating is always operated below the glass transition temperature in its hard, glassy phase state. It must also have good chemical resistance to solvents and ability to stop any moisture to get through it. The surface properties of the secondary coating should also be carefully controlled to allow good adhesion of the ink used in colour identification while allowing for good winding onto spools. Here in our report, the HCF involved in experiment and simulation is dual coated with typical acrylate.

When we study the coating-induced influence on thermal sensitivity of fibres, three properties of the coating materials are mostly important: Young's modulus, thermal expansion coefficient, and Poisson's ratio. For the coated HCF used in our study, the primary coating is DP-1021 and secondary coating is DS-2042, which are both manufactured by DeSolite® and the data on the properties of the two materials is provided.

Properties of the two coatings are shown in the Table 2.1, which are supplied by the manufacturer and the values with * are typical values for acrylate).

Table 2.1 Properties of the two coating materials.

Primary coating (DP-1021)		Secondary coating (DS-2042)	
Liquid Coating	**Typical Properties**	**Liquid Coating**	**Typical Properties**
Viscosity, 25°C	6,000 MPa·s	Viscosity, 25°C	6,002 MPa·s
Density,23°C	1,030 kg/m^3	Density,23°C	1,130 kg/m^3
Cured Coating	**Typical Properties**	**Cured Coating**	**Typical Properties**
Glass Transition Range, at E=1000 MPa	-57°C	Glass Transition Range, at E=1000 MPa	10.6°C
Glass Transition Range, at E=100 MPa	-45°C	Glass Transition Range, at E=100 MPa	86.1°C
Volumetric coefficient of expansion	239 ppm/°C (glassy region) and 863 ppm/°C (rubbery region)	Volumetric coefficient of expansion	80 ppm/°C
Poisson's ratio	0.37*	Poisson's ratio	0.37*

One of the key parameters is the Young's modulus, and since elastic modulus provided in the data is measured only slightly different to Young's modulus, we assume they are the same in our study. As shown in Figure 2.8, Young's modulus of the primary coating is nearly constant above -45°C, ensuring this coating is in rubbery state. For the secondary coating, the glass transition happens at a lot higher temperature, and it becomes softer as Young's modulus decreases with temperature. This difference between their glass transition temperature ranges implies that the secondary coating behaves more temperature-dependently than the primary coating at the operation temperature range. To make both coatings work as they are supposed to, the operation temperature region is about between -45°C and 86°C (grey region). In our research, we primarily study it in the vicinity of room temperature.

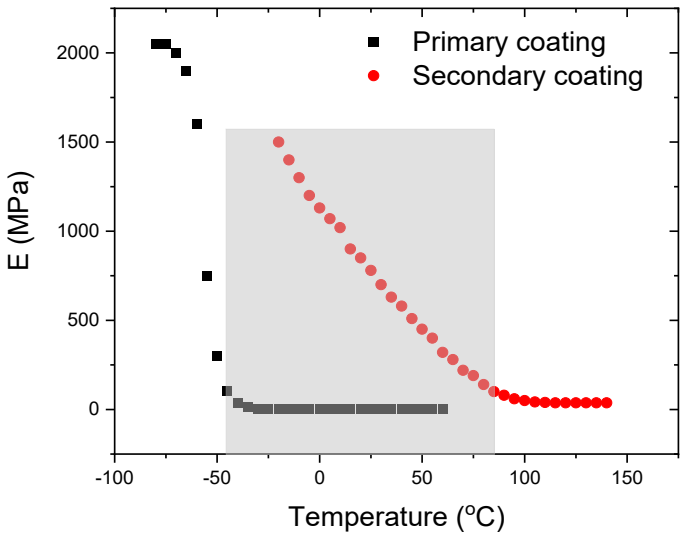

Figure 2.8 The Young's modulus of the primary coating (DP-1021) and secondary coating (DS-2042).

Chapter 3. Background: Introduction of HCFs' characterisation

In this chapter, we discuss all the characterisation methods used in the thesis. For the studies on thermal sensitivity of coated HCFs, we use both numerical simulations and experimental methods to characterise the thermal sensitivity. The backscattering based distributed characterisation of OTDR will be discussed later in this chapter.

3.1 COMSOL Multiphysics

Finite element analysis (FEA) is a numerical method to solve partial differential equations (PDE) that are difficult to solve analytically. A given geometry is broken down into small elements by FEA, which uses a system of algebraic equations to express the relationship at the points (nodes) connecting the elements. This allows the original differential equations to be simplified into a system of algebraic equations that can be quickly solved by a computer with providing an approximate solution to the problem. Today, FEA is a very common technique used among engineers as it allows for computational models to be developed for real world engineering problems. The solutions of these models are used to verify experimental results, which leads to significantly fewer experiments needed to be run.

COMSOL Multiphysics is a powerful interactive simulation software used to model and solve a large variety of scientific and engineering problems. The software provides a powerful integrated desktop environment with a Model Builder that gives a full overview of the model and access to all functionalities. With COMSOL Multiphysics, we can easily extend conventional models for one type of physics into multiphysics models thanks to the ability to couple any number of physics phenomena together, which is usually impossible with traditional approaches. This does not require an in-depth knowledge of advanced mathematics or numerical analysis. With the help of the built-in physics interfaces and the support for material properties, models can be built by defining the relevant physical quantities (e.g., material properties and constraints) instead of defining underlying equations. COMSOL then internally compiles a set of equations that describe the model. Therefore, in our research, we use COMSOL as the tool to do simulations in Chapter 4 and Chapter 5 when we study coating's impact on thermal sensitivity of HCFs.

The workflow for building a model usually consists of the following steps:

1) Setting up the model environment
2) Building the geometry
3) Specifying material properties

4) Defining physics and boundary conditions
5) Creating the mesh
6) Running the simulation
7) Postprocessing the results

To simulate the thermal elongation of an optical fibre, the theoretical model includes both mechanical properties and heat transfer. In COMSOL, this requires the use of two independent physics interfaces (Solid mechanics and Heat transfer in solids). By combining these two interfaces together, the effect of thermal expansion can be simulated.

The Solid mechanics interface is based on solving the equations of motion together with a constitutive model for a solid material and results such as displacements, stresses, and strains are computed. The Heat transfer in solids interface is used to model heat transfer in solids by conduction, convection, and radiation. These two interfaces are then coupled together by the coupling interface of Thermal expansion. This coupling occurs on the domain level, where the temperature from the Heat transfer interface acts as a thermal load for the Solid mechanics interface, causing thermal expansion. After equations for heat transfer and solid mechanics are solved by COMSOL, changes in temperature will be reflected in material dimension changes and resulting stresses and strains in the solid mechanics.

The principle for heat transfer is given by the equation:

$$\rho C_P u \cdot \nabla T + \nabla \cdot q = Q \ (q = -k \cdot \nabla T), \qquad 3\text{-}1$$

with the following material properties, fields, and sources: ρ (kg/m^3) is the solid density, C_P (J/kg/K) is the solid heat capacity at constant pressure, k (W/m/K) is the solid thermal conductivity, u (m/s) is the velocity field defined by the node of translational motion when parts of the model are moving in the material frame and Q (W/m^3) is the heat source.

The temperature at any point is determined with Eq. 3-1. Once the temperature at every point is known, the strain, ε_{th}, due to thermal expansion, can be calculated by:

$$\varepsilon_{th} = \alpha\big(T - T_{ref}\big). \qquad 3\text{-}2$$

Here, α is the coefficient of thermal expansion. At the same time, the stresses in the materials can be obtained by the momentum conservation theory.

In partial differential equations, boundary conditions are necessary for the solution. Here in our models, the dependent variables are prescribed when boundary conditions (temperature for heat transfer and displacement for solid mechanics) are given. Equations for such degrees of freedom can thus be eliminated from the problem. When looking in the equation view of COMSOL, these conditions will appear as constraints.

Let us take the boundary condition of solid mechanics for example, all boundaries are free by default, which means there are no constraints and no loads acting on the boundaries and thus they are free to move. We change this according to requirement of the model by fixing one or more boundary through the node of prescribed displacement where the displacements are prescribed in the direction to the geometric domain, which allows the solid to be free to deform in the other directions.

3.2 Measurement of thermal phase sensitivity

3.2.1 Principle

Our experimental system of measuring thermal phase change of HCFs is based on conventional Mach-Zehnder interferometer as illustrated in Figure 3.1. The laser source is split and injected into the two arms through a coupler, part being sent through one arm and the remainder through the other arm. After passing through different paths, the two signals are joint together at the second coupler and an interference signal is then formed and detected by photodetectors.

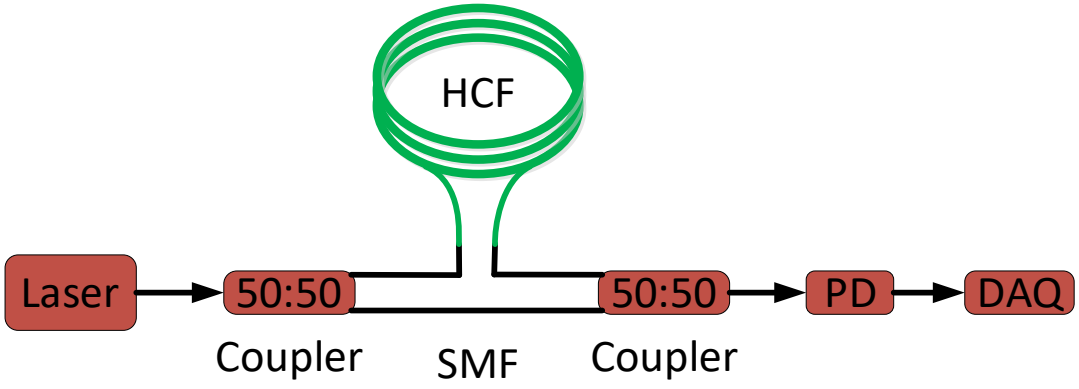

Figure 3.1 Experimental setup for HCF thermal phase sensitivity measurement based on a Mach-Zehnder interferometer (PD: photodetector; DAQ: data acquisition card).

In our experiment, the HCF under test is inserted into one arm and the lengths of the fibre coupler pigtails of both arms are carefully balanced so that their thermal behaviour induced impact can be minimized and thus the phase change only comes from the HCF under test. The entire interferometer is put into a thermal chamber along with one or more thermometers to monitor the temperature.

When temperature changes, the optical path length of the HCF under test changes and the phase ($\varphi = {}^{2\pi n_{eff} L}/_{\lambda}$) of the light propagating through it changes accordingly. This changes the intensity of the output (interferometric fringes) and since one fringe corresponds to phase change of 2π, the accumulated phase change can be obtained by counting the number of fringes.

The thermal phase sensitivity S_φ can be calculated from the number of fringes:

$$S_\varphi = \frac{1}{L}\frac{d\varphi}{dT} = \frac{2\pi}{\lambda}\left(\frac{n_{eff}}{L}\frac{dL}{dT} + \frac{dn_{eff}}{dT}\right) = \frac{number\ of\ fringes \cdot 2\pi}{\Delta T \cdot L}. \quad 3\text{-}3$$

where L is the length of the fibre under test, λ is the laser wavelength, and ΔT is the temperature change occurring during the observation time.

This method is simple for the thermal phase sensitivity calculation, but it is unable to find if the phase is increasing or decreasing (this will be important for us to experimentally observe the phase relaxation effect in Chaper-4). What's more, when the phase change is very slow (e.g., for a thermally insensitive fibre), this method becomes useless.

To overcome these difficulties, the method based on 3x3 coupler is used in our experiment [97]. The core idea of this method is to construct orthogonal variables and then demodulate the phase. The optical path scheme of this method are shown in Figure 3.2.

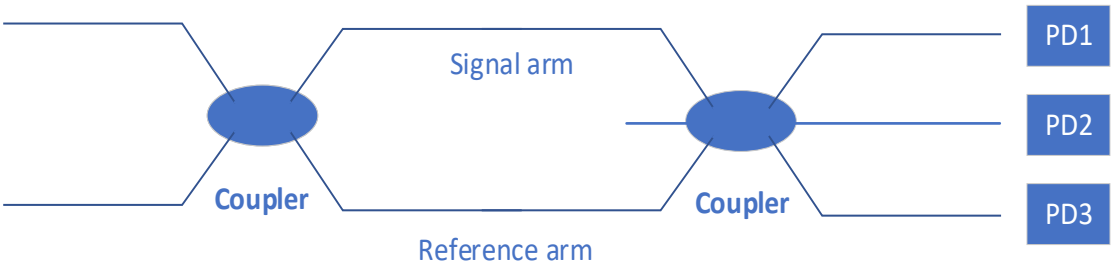

Figure 3.2 Schematic of the optic for the (3x3) passive homodyne detection (PD1, PD2, PD3, the three outputs of the interferometer) [97].

The three outputs at the second coupler are:

$$I_1 = A_1\cos(\theta + \varphi_1) + B_1. \quad 3\text{-}4$$

$$I_2 = A_2\cos(\theta + \varphi_2) + B_2. \quad 3\text{-}5$$

$$I_3 = A_3\cos(\theta + \varphi_3) + B_3. \quad 3\text{-}6$$

Here, I_1, I_2, I_3, and A_1, A_2, A_3, and B_1, B_2, B_3 are amplitudes, ac amplitudes and offsets of the three outputs after photodetectors, respectively. θ is the phase difference of the two arms. φ_1, φ_2 and φ_3 are delayed phases related to the coupler output (0, + $2\pi/3$ and -$2\pi/3$). After normalization:

$$I_1 = \cos(\theta + \varphi_1). \quad 3\text{-}7$$

$$I_2 = \cos(\theta + \varphi_2). \quad 3\text{-}8$$

$$I_3 = \cos(\theta + \varphi_3). \quad 3\text{-}9$$

Then orthogonal variables using any two outputs can be built as the following:

$$S_1 = I_1 + I_2 = 2\cos(\theta + (\varphi_1 + \varphi_2)/2)\cos\left(\frac{\Delta\varphi}{2}\right). \quad 3\text{-}10$$

$$S_2 = I_1 - I_2 = -2\sin(\theta + (\varphi_1 + \varphi_2)/2)\sin\left(\frac{\Delta\varphi}{2}\right). \quad 3\text{-}11$$

$$S_1 \cdot \dot{S_2} - \dot{S_1} \cdot S_2 = 4\sin\left(\frac{\Delta\varphi}{2}\right)\cos\left(\frac{\Delta\varphi}{2}\right)\dot{\theta} = 2\sin(\Delta\varphi)\,\dot{\theta}\,. \quad 3\text{-}12$$

The phase difference between the two of the three interferometer outputs: $\Delta\varphi = \varphi_1 - \varphi_2$. This can be integrated, which is directly proportional to the phase change of the fibre under test:

$$\int 2\sin(\Delta\varphi)\,\dot{\theta}\,dt = 2\sin(\Delta\varphi)\,\theta. \quad 3\text{-}13$$

3.2.2 Factors in measurements

In the experiment, some factors might also influence the measurement of the thermally induced phase change of the fibre under test, which should be considered.

3.2.2.1 Stability of the laser source

According to $\varphi = {}^{2\pi n_{eff} L}/_{\lambda}$, phase change comes from three sources: effective index change, fibre length change and wavelength change. The first two terms are related to the fibre and the third term is related to the frequency variation of the laser source. Therefore, it is important to keep the frequency of laser source stable in order to make sure that the phase change is solely caused by temperature change on the HCF under test. This requires us to use a laser, of which the linewidth should be sufficiently narrow. This is usually determined by the spectral period of the Mach-Zehnder Interferometer. For a Mach-Zehnder Interferometer, the Free Spectral Range (FSR) is given by:

$$\Delta f = \frac{c}{n\Delta L}. \quad 3\text{-}14$$

Where *c* is the speed of light in vacuum, n is the refractive index of the fibre and ΔL is the path length difference between the two arms of the interferometer. Therefore, to distinguish the individual interference fringes clearly, the laser linewidth must be narrower than the FSR, which is related to the path length difference. For example, the FSR, when a 30 m HCF acts as the path difference, would be 10 MHz, requiring the source linewidth to be few MHz or less.

3.2.2.2 The power balance on the two arms

If the intensity of each arm is I_1, I_2, respectively, after passing through the combined 2×2 3 dB coupler, the output intensity for interference would be half of that. When the phase difference of signal in the two arms is $\Delta\varphi$, the intensity of the interference signal is [98]:

$$I = \frac{1}{2} I_1 + \frac{1}{2} I_2 + \sqrt{I_1 I_2}\cos(\Delta\varphi). \quad 3\text{-}15$$

Therefore, the maximum and minimum intensity at the output are:

$$I_{max} = \frac{1}{2} I_1 + \frac{1}{2} I_2 + \sqrt{I_1 I_2}. \quad 3\text{-}16$$

$$I_{min} = \frac{1}{2} I_1 + \frac{1}{2} I_2 - \sqrt{I_1 I_2}. \quad 3\text{-}17$$

Then the fringe visibility [99] is calculated:

$$V = \frac{I_{max} - I_{min}}{I_{max} + I_{min}} = \frac{2\sqrt{I_1 I_2}}{I_1 + I_2}. \quad 3\text{-}18$$

As shown in Figure 3.3, the visibility is calculated as a function of the normalized intensity of I_2/I_1, where *V* reaches its maximum value of 1 when $I_1 = I_2$. Therefore, the output power of the two arms is preferred to be balanced. In practice, a power meter is used to monitor the power when fibres of the two arms are spliced.

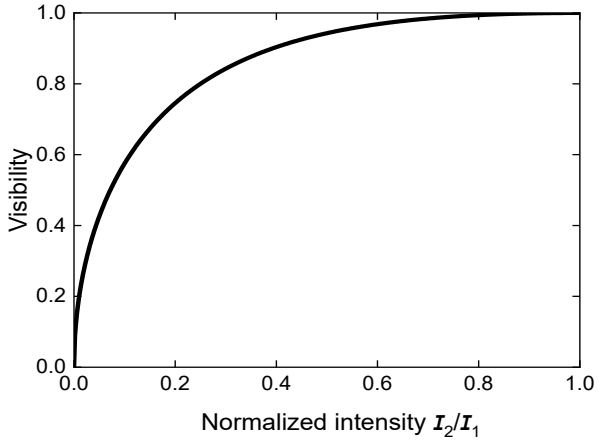

Figure 3.3 The calculated visibility as a function of the normalized intensity of I_2/I_1.

3.2.2.3 Influence of polarization

Because of the birefringence of the fibre, the polarization state of the lights on the two arms changes. To simplify our analysis, let's suppose that at the end of the two arms, the light is linearly polarised and the polarisation states of them are as shown in Figure 3.4.

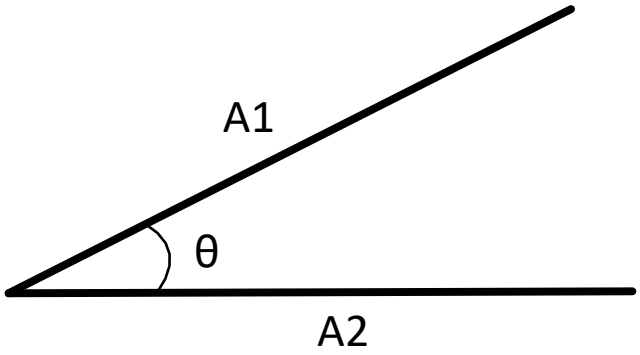

Figure 3.4 Polarization states of the lights on the two arms.

And then we assume the intensities of the two arms are the same: $I_1 = I_2 = I_0$, in which case the output of the interferometer can be given by (Eq. 3-15):

$$I = I_0 + I_0 \cos\theta \cos\Delta\varphi. \qquad 3\text{-}19$$

where $\Delta\varphi$ is the phase difference of signals in the two arms. If $\theta = 0$, $I = I_0 + I_0 \cos\Delta\varphi$; if $\theta = \pi/2$, $I = I_0$; Therefore, the visibility of the fringes can get worse due to the polarization states of the lights in the two arms. To improve it, a polarization controller can be used to adjust the polarization state of the light, ensuring maximum interference and thus better fringe visibility.

3.3 Optical Time-Domain Reflectometry (OTDR)

In this section, we will discuss the OTDR, including the physical mechanism, the basic principle, and the key parameters.

3.3.1 Backscattering

The frequency spectrum of scattered light, including Rayleigh, Brillouin, and Raman scattering, is depicted in Figure 3.5. The central peak at the incident light frequency is Rayleigh scattering, which is caused by small-scale inhomogeneities (small in comparison to the wavelength of the light) that arise during the fibre fabrication process. Examples of these inhomogeneities include fluctuations in glass composition, resulting in slight refractive index variations, as well as density fluctuations. As there is no frequency shift between the incident and scattered light, Rayleigh scattering is categorized as elastic scattering.

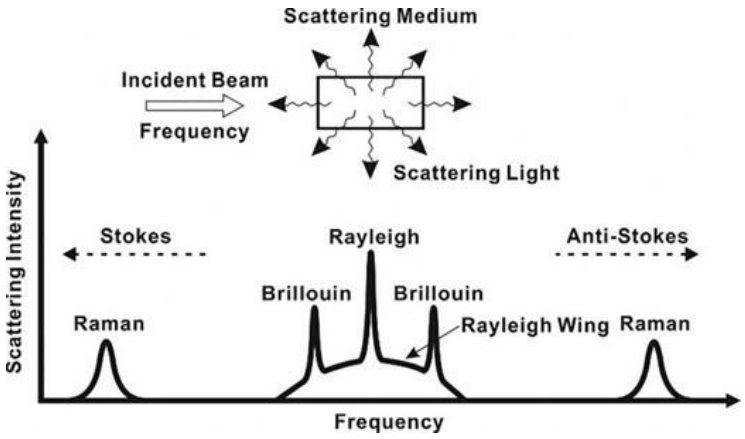

Figure 3.5 Spectrum of light scattering.

Adjacent to the central Rayleigh peak, Brillouin scattering is caused by light's interactions with propagating acoustic phonons. When incident light is scattered by molecular vibrations, it is recognized as Raman scattering, which can also be seen as the light scattering from optically generated phonons. Due to the frequency shift between the incident and scattered light, both Brillouin and Raman scattering are inelastic scattering. Scattering that shifts to lower frequencies compared to the incoming photons is termed the Stokes components, whereas those shifting to higher frequencies are anti-Stokes components.

As it is the dominant scattering, Rayleigh scattering is an important linear effect in solid optical fibres, as it typically sets the fundamental limit for the transmission loss. It accounts for most of the loss in the conventional SMFs in the centre of silica's transmission window, as other sources of loss have been already minimized. Backscattering in HC-PBGFs is caused by surface scattering which (incidentally) also set the minimum achievable loss in these types of fibres. Interestingly, as backscattering travels back to the launching end of the fibre, it is often used in reflectometers for fibre testing [100, 101]. One interesting point worth noting is that the Rayleigh scattering makes the sky blue. This is because Rayleigh scattering is inversely proportional to the fourth power of the wavelength, and so shorter wavelengths (like blue light) can scatter more.

3.3.2 Working principle

Since the first demonstration in 1970s, Optical Time-Domain Reflectometry (OTDR) has been seen as a powerful tool in characterizing optical fibres, identifying faults, and assessing the health of fibre optic networks [102, 103]. OTDR operates on the principle of sending a short optical pulse into an optical fibre and then measuring the backscattering (Rayleigh scattering) and Fresnel reflection along the fibre. The illustration of backscattering and reflection is shown in Figure 3.6. The reflection at silica-air interface (n_1 vs n_3) is approximately -14.4 dB, which is several orders of magnitude higher than the backscattering in fibres. The time delay between the launched pulse and the arriving time of the

backscattered signals provides information about the distance to the points of reflection. By analysing the intensity and time-of-flight of these signals, OTDR allows users to have a comprehensive view (losses, fibre faults, splice points and connectors) of the entire length of an optical fibre.

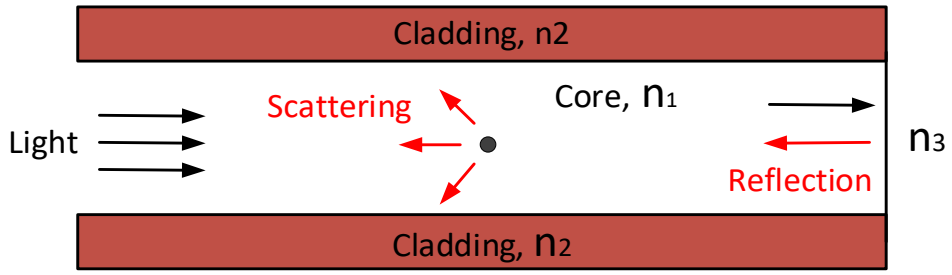

Figure 3.6 The illustration of scattering in a fibre and Fresnel reflection at the interface between fibre and air.

As a non-destructive technique, OTDR can do the measuring by accessing to just one end of the fibre, as the backscattered signal is collected from this same end. This is a very important advantage, which, therefore, is preferred for installed fibres as the other end is always kilometres away. The phenomenon of Rayleigh backscattering operates in a linear fashion, indicating that the magnitude of the backscattered power is directly proportional to the optical power at that specific location. Consequently, the backscattered power gradually decreases at a rate, which is the same as the fibre attenuation.

The typical OTDR system setup is shown in Figure 3.7. The CW laser is firstly modulated into pulses (pulse width can vary from ~ns to ~μs) and these pulses are injected into the fibre under test (FUT) via a circulator. The backscattering signal from the FUT can be directed to the detector and then converted into digital signal and analysed in data acquisition device (DAQ). Since the DAQ card is synchronised to the pulse source, the time delay between the pulse launching and backscattering arriving time can be precisely known, which is used to calculate the location of the signal. Thus, the backscattering power can be shown as a function of fibre distance, as illustrated by a typical OTDR trace in Figure 3.7.

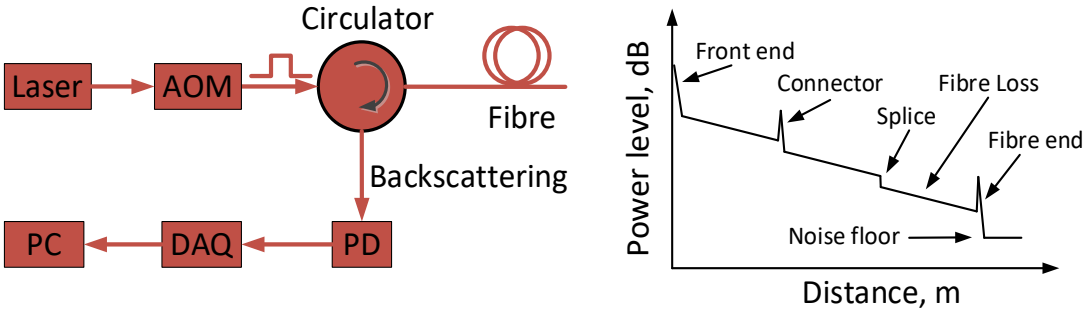

Figure 3.7 The typical setup of an OTDR system and a typical trace (PC: computer for data processing; DAQ: data acquisition card; PD: photodetector; AOM: acousto-optic modulator).

When we consider the attenuation coefficient of an fibre is α, which can have several origins such as scattering loss and absorption loss, the power that arrives at the point of z can be expressed as:

$$\mathrm{P(z)} = P_0 e^{-\alpha z}, \qquad \text{3-20}$$

P_0 is the launched power (when z = 0).

Since the pulse length is the fibre section that produces the backscattering, here we consider the pulse length as:

$$\Delta L = v_g \tau_p = \frac{c}{n_g} \tau_p, \qquad \text{3-21}$$

Here, v_g is the group velocity in the fibre ($v_g = \frac{c}{n_g}$), c is the speed of light in vacuum, n_g is the group refractive index of the fibre and τ_p is pulse width (unit: ns). The used group refractive index is usually 1.468 for SMFs [104] and 1.003 for HCFs.

The distance of a point (z) in the fibre that gives rise to backscattering signal can be calculated from the delay of the pules traveling in forward and backward direction as:

$$z = \frac{v_g t}{2} = \frac{1}{2} \frac{c}{n_g} t, \qquad \text{3-22}$$

Here, ½ is introduced since z represents the distance from the start of the fibre (z = 0).

Then, when a typical rectangular pulse with length of ΔL is used, the backscattering power at z can be defined as:

$$P_b(\mathrm{z}) = P(z) \alpha_s S \Delta L = \alpha_s S \Delta L P_0 e^{-\alpha z}, \qquad \text{3-23}$$

α_s is the attenuation factor due to Rayleigh scattering and S is the recapture coefficient. Thus, $\alpha_s S$ can be seen as the backscattering coefficient.

Therefore, the received backscattering power at z = 0 is:

$$P_{br}(\mathrm{z}) = \alpha_s S \Delta L P_0 e^{-2\alpha z}, \qquad \text{3-24}$$

For the backscattering power within a pulse length of ΔL, the received value would be corresponding to that of half of the pulse length, so:

$$P'_{br}(\mathrm{z}) = \alpha_s S \frac{c}{2 n_g} \tau_p P_0 e^{-2\alpha z}. \qquad \text{3-25}$$

As seen in Eq. 3-25, shorter pulses result in lower backscattered power. As a consequence, the sensitivity of the OTDR system is influenced by the pulse width, where wider pulses tend to provide higher sensitivity, but lower spatial resolution (mentioned later). In addition,

the sensitivity increases linearly with the launched power, which provides an general approach for researchers in building high-sensitivity OTDR system.

3.3.3 Key parameters

The performance of an OTDR system is mainly specified by several parameters, which will be discussed in the following.

3.3.3.1 Spatial resolution

The spatial resolution, here, denoted as *SR*, in an OTDR system (also referred to as the two-point resolution) is determined as the smallest distance between two distinct reflective events of equal power within a fibre [105]. This value is the same as the full-width half-maximum (FWHM) of a singular reflection in a reflectometry trace.

SR is defined as:

$$SR = \frac{c\tau_p}{2n_g}. \tag{3-26}$$

Since the spatial resolution is proportional to pulse width, so the shorter the pulse width is, the better is the spatial resolution. For example, 10 ns pulse corresponds to a spatial resolution of 1 m in SMFs and 1.5 m in HCFs, while 100 ns gives a 10 times bigger spatial resolution. It is worth mentioning, however, that other factors can also set a limitation on spatial resolution, e.g., DAQ and photo detector [106]. For example, a centimetre level resolution is only possible when the bandwidth of the used DAQ is better than gigahertz.

3.3.3.2 Dynamic range

As one of the most important parameters for a OTDR, the dynamic range represents the instrument's ability to accurately measure and distinguish between various levels of backscattered signals within an optical fibre [105]. It is defined as the difference (expressed in dB) between the extrapolated point of the backscattering trace at the beginning of the fibre and the RMS level of the noise, which is related to the detection principle, but not often used today. The more often used definition is the level when 98% of the data falls below, of which the dynamic range is about 1.6 dB smaller than that when using RMS of noise as the noise level [107, 108]. This definition was used by the International Electrotechnical Commission, IEC. When we consider the limit that OTDR can measure, the noise level is 0.1 dB on the trace [108]. This provides a dynamic range that is 6.6 dB less than the dynamic range (RMS). The three definitions are illustrated in Figure 3.8. Here in this thesis, we use dynamic range (98%).

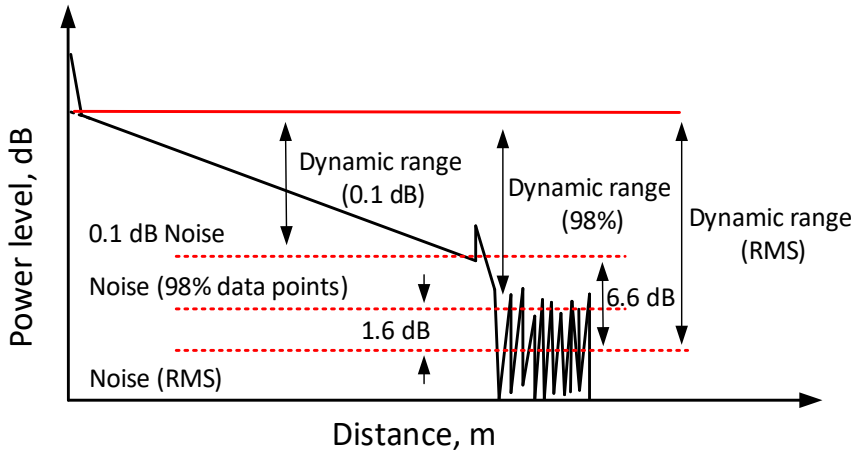

Figure 3.8 Dynamic range definitions.

3.3.3.3 Sensitivity

Although it is not often to be mentioned in the performance sheets for OTDR instruments, the general definition of the sensitivity is the lowest backscattering level that can be separated from noise after a certain measuring time, for a certain pulse width. Therefore, it is akin to dynamic range.

3.3.3.4 Dead zone

Since the signal from the reflective events can be several orders of magnitude higher (e.g., Fresnel reflection at the glass-air interface when connecting HCFs to SMFs), this strong reflection potentially can cause detector saturation. This results in a temporary saturation and so a certain recovery period is needed before accurate measurement can be obtained. During this recovery period, the precise recording of the backscattering signal becomes compromised. The fibre distance between the initial edge of this reflection and the point where the OTDR can once again accurately measure (usually 0.1 dB within the fibre's backscattering level [108]) is termed as the "dead zone", as simply illustrated in Figure 3.9.

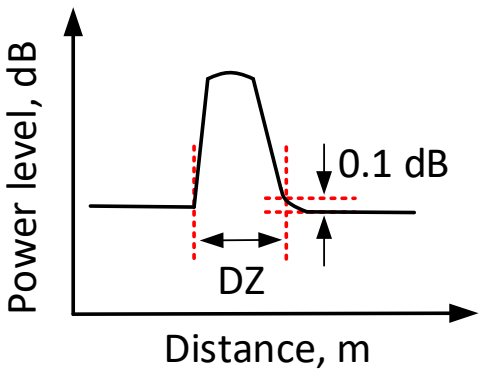

Figure 3.9 Illustration of the Dead zone.

The range of the dead zone for OTDR instruments typically varies from a few meters to several hundred meters, depending on factors such as the sensitivity of the detector, the intensity of the reflection, and the pulse width. Therefore, for a given detector or instrument, it is advisable to use connections with low reflection, such as angled connections between SMFs and HCFs, to minimize the dead zone. Additionally, using an optical shutter has proven effective in reducing the effect of high reflections [109]. A narrow pulse also helps, although it results in a lower dynamic range, and we will show later the approach to compensate this.

Chapter 4. Effect of Coating on thermal sensitivity of HCFs

In this chapter, we (supervisor, my colleague who conducted the experiment) aim to study how the coating influences the overall thermal phase sensitivity of HCFs. This is studied by conducting experiments (by my colleague) and simulations (by myself) on both standard dual-coated HCFs and thinly coated HCFs.

4.1 Coating-induced change

4.1.1 Experiment

Here, we show the experimental results on the thermal phase sensitivity of both dual coated and thinly coated HCFs, which was conducted by B. Shi, a colleague in my group. The key parameters of the HCF samples are listed in Table 4.1. It would be ideal to have both fibre with identical silica thickness to compare the coating's impact, but in practice we were limited to available fibre samples. The cross-sections of the two samples are shown in Figure 4.1. The simulations and discussion on coating's effects later in this chapter will be based on the results here.

Table 4.1 The parameter of the used HCF samples.

Samples to compare	Type	Loss at 1550 nm	Inner diameter of Silica Jacket, μm	Outer diameter of Silica Jacket, μm	Diameter of Coating, μm
Dual-coated	6-element NANF	3.5 dB/km	83	245	368
Thinly-coated	6-element NANF	6 dB/km	70	185	205

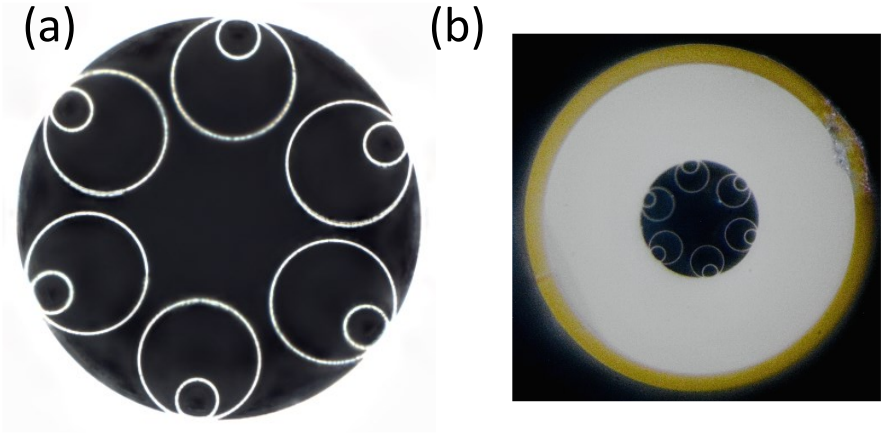

Figure 4.1 Cross section of (a) the dual-coated HCF and (b) thinly coated HCF with coating shown in yellow.

To measure the optical phase change in a HCF, a 30 m dual coated HCF was spliced into one arm of a Mach-Zehnder interferometer, as shown in Figure 4.2. The used laser source is a laser that has a narrow linewidth of < 1 MHz (1558 nm, RIO Orion from NuFern). This is more than sufficient for our experiment to ensure the observed phase change is not related to the source, as the MZI spectral period is >10 MHz (determined by the relatively short HCF length). The length of the fibre coupler pigtails in both arms (SMFs) were carefully balanced to minimize the impact of their thermal behaviour during the experiment. To extract the phase change direction, the 3x3 coupler based demodulation method is used here, as we discussed earlier in Chapter 3.

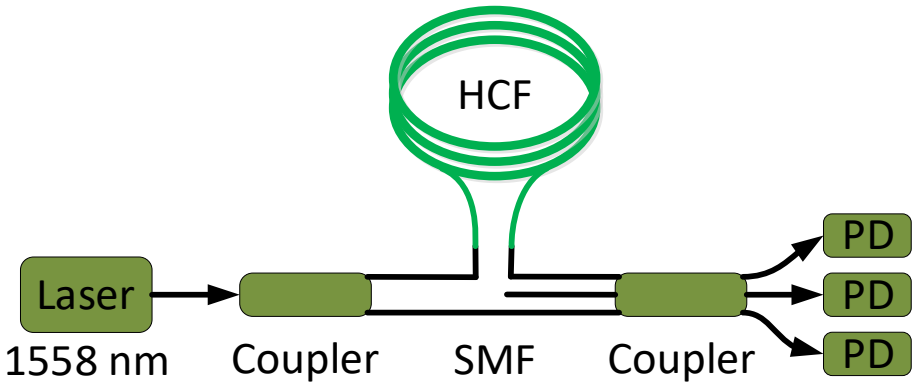

Figure 4.2 Experimental setup based on M-Z interferometer.

In this experiment, temperature was increased from 20°C to 40°C, from 40°C to 58°C, from 58°C to 40°C and finally went back to 20°C. As shown in Figure 4.3, the phase increases with temperature, which is as expected. However, once the temperature stays unchanged, the phase change still keeps decreasing, lasting for several hours. This effect of “relaxation” is believed to be observed for the first time and will be discussed in detail later.

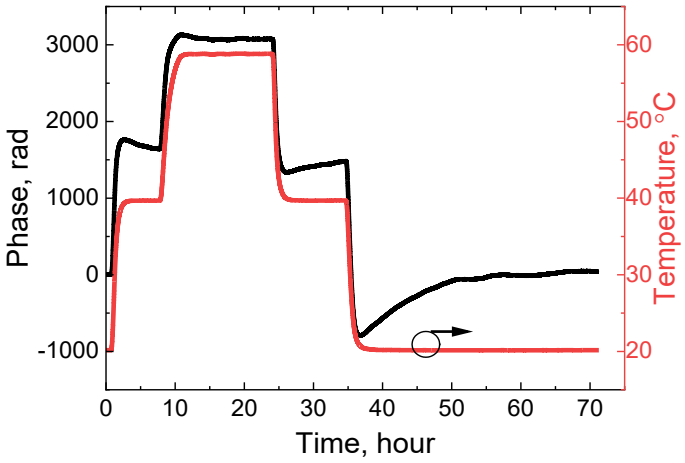

Figure 4.3 The measured phase and temperature changes of a 30 m dual-coated HCF (Thickness of coating: 123 μm).

To identify the coating's influence, a 24 m thinly coated HCF (only 10 μm thickness) was also measured. The measured phase change with temperature is shown in Figure 4.4, where the effect of "relaxation" is not introduced for this HCF as the contribution from the coating becomes very limited.

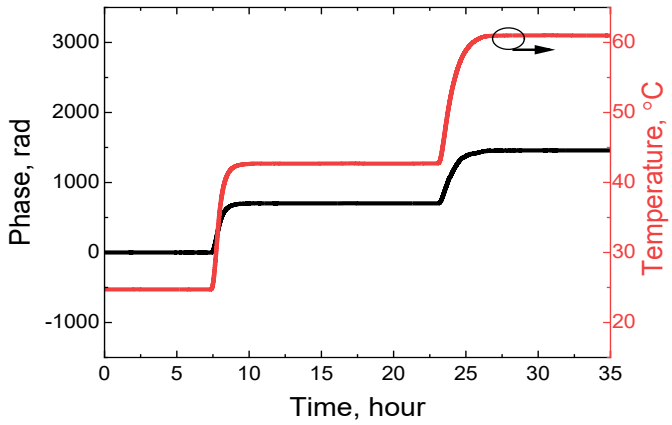

Figure 4.4 The measured phase and temperature changes of a 24 m thinly-coated HCF (Thickness of coating: 10 μm).

The thermal phase sensitivity of an optical fibre is usually defined as the derivative of the phase change with temperature (and length), as seen in the Eq. 3-3. However, the calculated result with this method (named as dynamic thermal phase sensitivity) varies significantly with the measurement condition of how much relaxation has occurred. Thus, we define a static thermal phase sensitivity, which is obtained by dividing the stable phase change when the phase reaches a stable level after a temperature change. Although this requires us to wait hours longer to stabilize the fibre, it only depends on fibre properties, which, thus, is repeatable.

Therefore, it can help us to better understand the difference of various fibres or between experiments and simulations by comparing both their dynamic and static thermal sensitivities. Since the static thermal sensitivity is only a function of fibre properties, it will

be more straightforward to be considered than the dynamic when we aim to reduce HCFs thermal sensitivity.

The measured static thermal phase sensitivity is shown in Figure 4.5. The measured dynamic thermal phase sensitivity is shown in Figure 4.6. As shown in Figure 4.5 and Figure 4.6, dynamic thermal phase sensitivity behaves very differently compared with the static value, which is dramatically influenced by how we measure it. Here, the dynamic thermal sensitivity is calculated using the phase-temperature change before the temperature reaches the stable level.

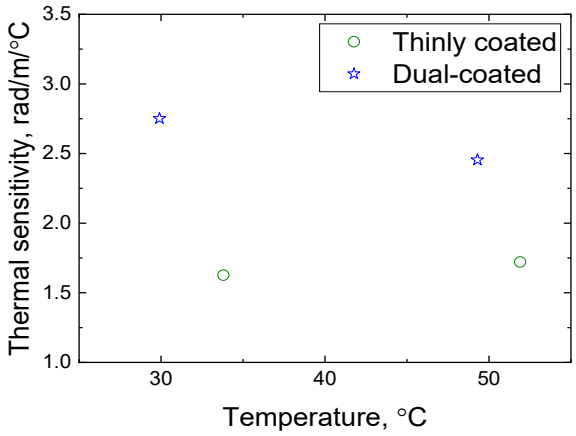

Figure 4.5 The measured static thermal phase sensitivity of a dual coated HCF and a thinly coated HCF.

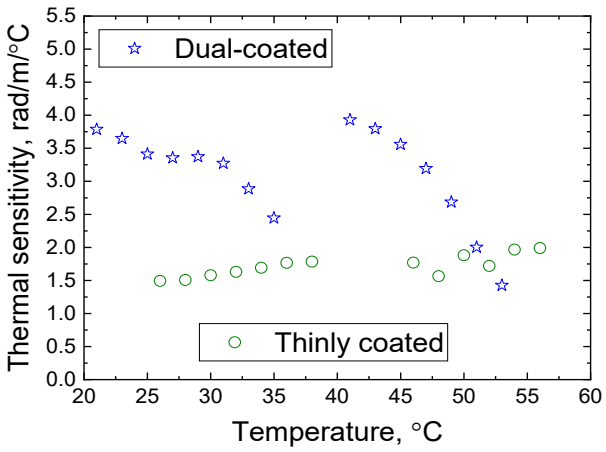

Figure 4.6 The measured dynamic thermal phase sensitivity of a dual coated HCF and a thinly coated HCF.

4.1.2 Simulation

In the COMSOL model, the thermal sensitivity of HCFs is considered to originate only from the thermally induced elongation, neglecting the refractive index change of the fibre. As analysed in [76], error caused by such approximation is negligible in HCFs.

The thermal phase sensitivity is calculated from the HCF thermally induced elongation ΔL as:

$$S_\phi = \frac{2\pi}{\lambda}\frac{n_{eff}\boldsymbol{\Delta L}}{L\Delta T}. \quad \text{4-1}$$

where λ is the light wavelength (here, we set λ =1550 nm), L is the fibre length, ΔT is the temperature change experienced by the fibre, and n_{eff} is the fibre effective refractive index ($n_{eff} \approx 1$).

A simplified HCF structure was used in my model (Figure 4.7 (a)). It disregards the influence of the microstructure to the elongation properties, which is considered to be very small. In fact, it is a simple capillary fibre. The "hollow core" in simulation is then the entire central hole (green circle), which is different to most literature, where the "core" size is given by the microstructure within the core, which is the red circle as seen in Figure 4.7 (a).

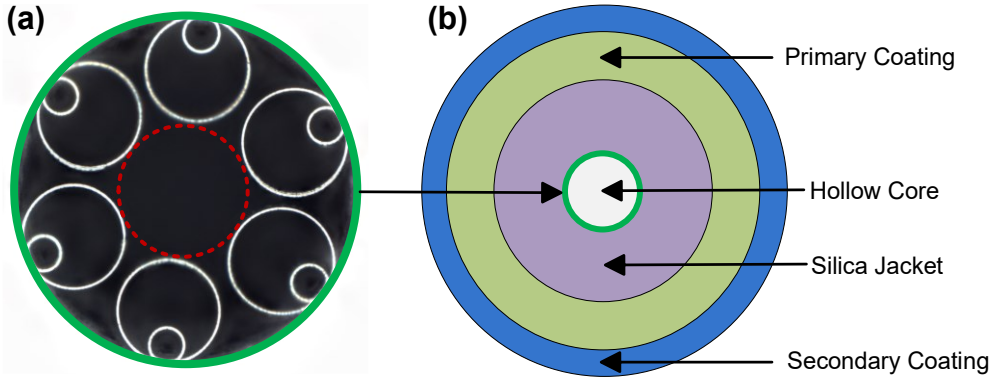

Figure 4.7 A dual-coated HCF cross-section (a) A HCF cross-section (red dotted circle: core in literatures; green solid circle: the defined core used in simulation) (b) The simplified dual-coated HCF structure for simulation.

Two independent physics interfaces (solid mechanics and heat transfer in solids) were used to build a 2D axis-symmetric model, which were coupled together to simulate the thermal elongation of an optical fibre, considering both heat transfer and mechanical properties. Although a stationary solution was employed, the heat transfer in solids interface was still used as it can visualize the temperature distribution inside the structure. As seen in Figure 4.8 (a), the model consists of four layers - hollow core, silica jacket, primary coating, and secondary coating. The corresponding 3D HCF structure built from the 2D structure is then shown Figure 4.8 (b).

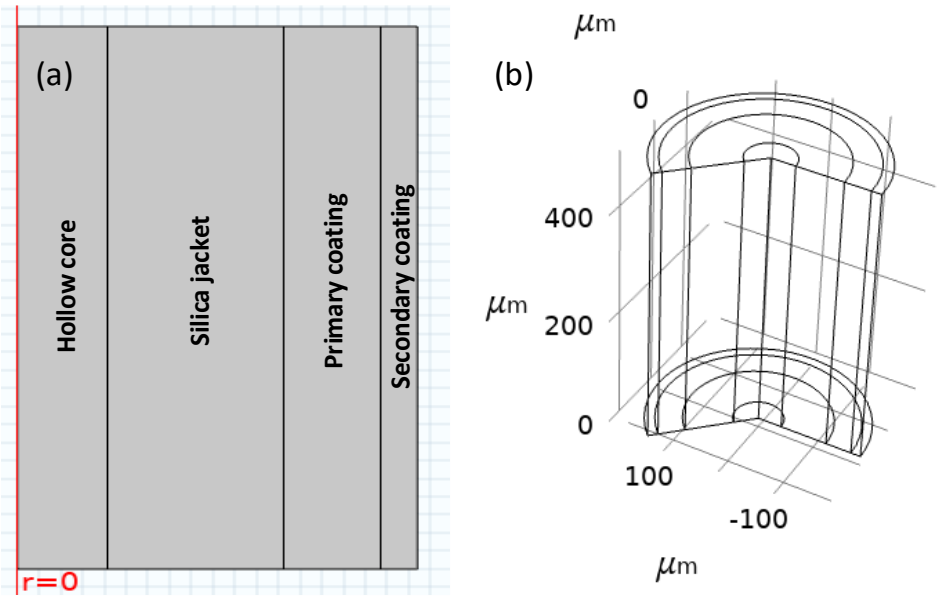

Figure 4.8 (a) 2D model and (b) the corresponding 3D structure of the HCF in model.

The simulated HCF has the same diameters as the used HCF in experiment with a modelled length of 10 mm. A fixed constraint was applied at one end of the fibre structure to prevent movement in the axial direction, while the other end was allowed to move freely (to show the elongation). For the temperature setting, the outer surface of the structure was defined as the boundary and was set to a target temperature, as the fibre surface is the first to be heated. The mesh was optimized based on simulation, ensuring that further refinement did not affect the results. With all of these settings in place, The thermal elongation at a target temperature can be directly obtained using a stationary solution. This elongation was then used (in Eq. 4-1) to calculate the thermal phase sensitivity.

The model geometry, based on the actual dimensions of the fibre, is detailed in Table 4.2, which also lists the used materials. The properties of the used coatings are listed in Table 2.1 and silica's properties listed in Table 4.3.

Table 4.2 The model geometry (2D model) and its materials.

The domain	Material	Width, μm
Hollow core	air	41.5
Silica jacket	silica	81
Primary coating	DeSolite® DP1021	44
Secondary coating	DeSolite® DS2042	17

Table 4.3 Properties of the used silica in model.

Density,23°C	2,203 kg/m^3
Young's modulus	73,100 MPa
Coefficient of expansion	0.45 ppm/°C
Poisson's ratio	0.17

4.1.3 Results and discussion

(1) Static thermal sensitivity

The simulated and measured static thermal phase sensitivities are shown in Figure 4.9. For the thinly coated HCFs, the thermal phase sensitivity is nearly constant with temperature, which is expected given the silica glass thermal expansion properties are weakly dependent on the temperature within the shown temperature range (the contribution from the thin coating is very limited). The slight difference in the level can be attributed to the difference between the used parameters of the materials in model and fabricated fibre.

Situation is different for the dual coated HCFs, in which their measured thermal phase sensitivity decreases by 10% and even more for the simulation. This might be because the influence from the difference between the used parameters of the materials, coating in particular, becomes more significant than the thinly coated HCF. The highly temperature dependent behaviour than thinly coated HCF is due to the thermal properties (e.g., Young's modulus) of the coatings being strongly temperature dependent.

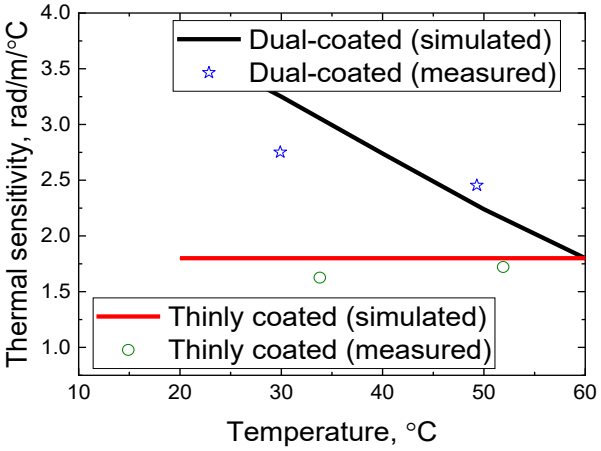

Figure 4.9 Simulated and measured static thermal phase sensitivities of dual coated and thinly coated HCFs.

(2) Dynamic thermal sensitivity

As discussed earlier, the temperature in the experiment (as shown in Figure 4.10) was increased from 20°C to 40°C, kept it at 40°C for few hours and increased again from 40°C to 58°C. As the dynamic thermal sensitivity depends on the experimental conditions, the temperature recorded in experiment was used as input to the COMSOL model. As can be seen in Figure 4.10, there is a jump at the stable temperature of 40°C, which we believe is related to the hours' waiting at 40°C of the fibre that makes the stress inside the fibre relax. Justification of this effect becomes clearer when we discuss relaxation of the coating later in this chapter.

As shown in Figure 4.10, the simulated dynamic thermal phase sensitivity of dual coated HCF, which was calculated based on the simulated phase-temperature curve, shows similar trend as measured result, though the slope is smaller. The dynamic thermal phase sensitivity seems to decrease with temperature between the two temperature increasing steps, which is similar to what we have observed in the static thermal sensitivity. In addition to this, the waiting's effect in the experiment can also be seen in our simulation, which indicates stress inside the fibre relaxed during the waiting time at 40°C. Here, the stress was simulated to be zero at 40°C, which was achieved by changing the reference temperature. We will discuss this effect in the following sub-section.

For the thinly coated HCF, the measured dynamic thermal phase sensitivity slightly increases with temperature (a constant value of 0.45 ppm/°C was used in simulation). This suggests that the TEC of silica is also temperature-dependent, which agrees with the data reported in literatures where shows a range of as much as 45% when compared to 0.55 ppm/°C (from 0.3 to 0.55 ppm/°C [34, 110-112]).

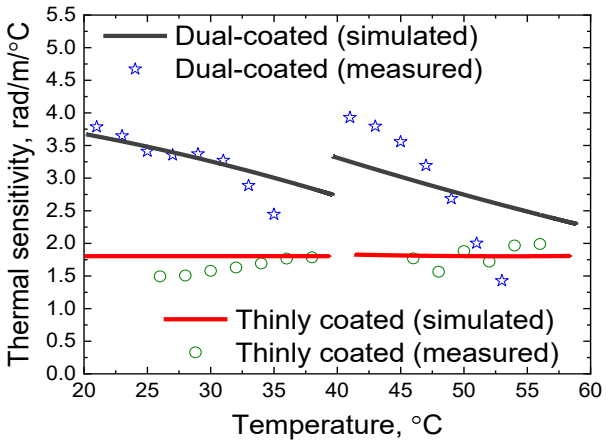

Figure 4.10 Simulated and measured dynamic thermal phase sensitivities of dual coated and thinly coated HCFs.

4.2 Coating-induced effect of relaxation

4.2.1 Relaxation observed experimentally and its quantification

In the measured phase-time curve in Figure 4.11, relaxations can be seen: phase change goes back partly after temperature reaches to a stable level (at 40°C, 58°C and 20°C). Here, relaxation change *RC* is defined as:

$$RC = \frac{\Delta phase_{peak} - \Delta phase_{stable}}{\Delta phase_{peak}}. \quad 4\text{-}2$$

$\Delta phase_{peak}$, the maximum phase change that occurs once the temperature becomes stable; $\Delta phase_{stable}$, the stabilized phase change measured after full relaxation. Based on this definition, a 6% relaxation happens following temperature increase from 20°C to 40°C and 2% when increasing temperature increases from 40°C to 58°C. For the process of cooling down, a >8% relaxation happens when temperature decreases from 58°C to 40°C (unfortunately, this step was not fully relaxed) and 35% when temperature decreases from 40°C to 20°C (Figure 4.11).

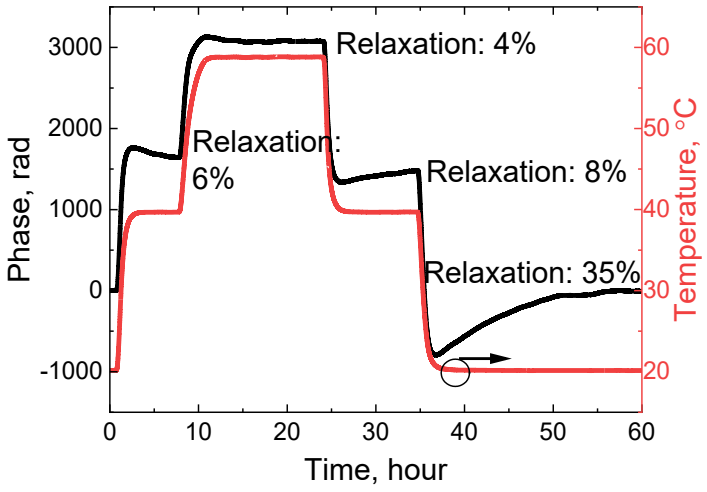

Figure 4.11 Phase Relaxation of the dual-coated HCF.

4.2.2 Modified model for simulating relaxation of the dual-coated HCF

Viscoelastic materials exhibit both viscous and elastic properties, which combines characteristics of both viscous behaviour (fluids) and elastic behaviour (solids). In our previous model, the thermal expansion effect was solely studied by elastic theory (silica jacket and coatings are defined as elastic materials), so there is no phase relaxation once temperature keeps constant, which is different to what has been observed in the experiment. However, the polymeric coatings for optical fibres are usually viscoelastic materials characterized by relaxation time, where the thermal stresses can be relaxed [113, 114].

Therefore, the coating material model needs improving to describe this relaxation phenomenon.

Here, the elastic model used for coatings was improved to a viscoelastic model using time-dependent solution, which besides the elastic material properties also considers stress relaxation following material deformation [115]. The updated HCF model is graphically shown in Figure 4.12.

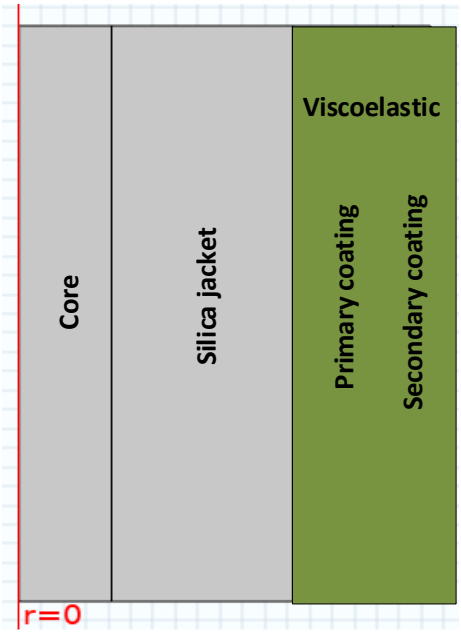

Figure 4.12 Updated HCF model to enable the simulation of the phase relaxation (viscoelastic material model used for both coatings, in blue).

Compared to the previously-used elastic model, the viscoelastic material COMSOL model requires a special parameter - Relaxation Time. However, no data or indication of the value of this parameter is provided by the coating manufacturer. Most viscoelastic materials are significantly dependent on temperature [116]. To test whether the viscoelastic model would actually describe the relaxation as seen in experiment, we used the following approach.

Firstly, we “guess” a temperature-dependent relaxation time we self-defined it as a temperature-dependent function, just for our proof of concept verification (shown in Figure 4.13), plugged it into our COMSOL model (for both coatings) and compared the result with the previously-calculated one (using elastic model only), as seen in Figure 4.14. Here we see that the relaxation appears once temperature stabilizes (with this proof of concept relaxation time).

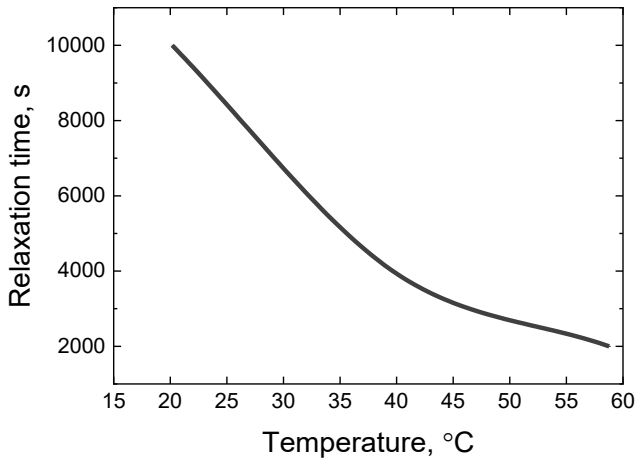

Figure 4.13 An initial 'proof of concept' relaxation time used in in COMSOL model for both coatings.

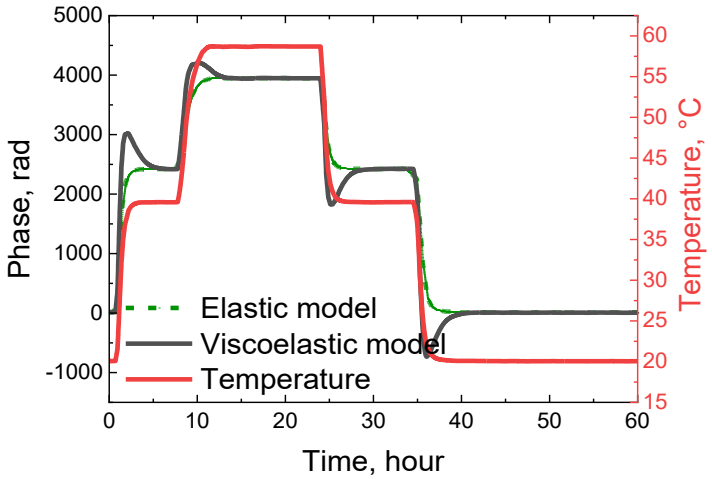

Figure 4.14 Simulated phase change with the new viscoelastic model and its comparison to that using elastic theory.

This effect of the viscoelastic coating properties is further illustrated in Figure 4.15, where shows the stress in axial direction inside different layers (average over each region) of the coated HCF. The temperature increase brings positive stress to the silica that is compensated by the negative stress in the secondary coating. Average stress in the primary coating is low, as it acts as a transducer between the silica and secondary coating. Following temperature stabilization, the secondary coating and silica glass stress difference is relaxed, causing silica glass length (and thus accumulated light phase) to change during the relaxation time.

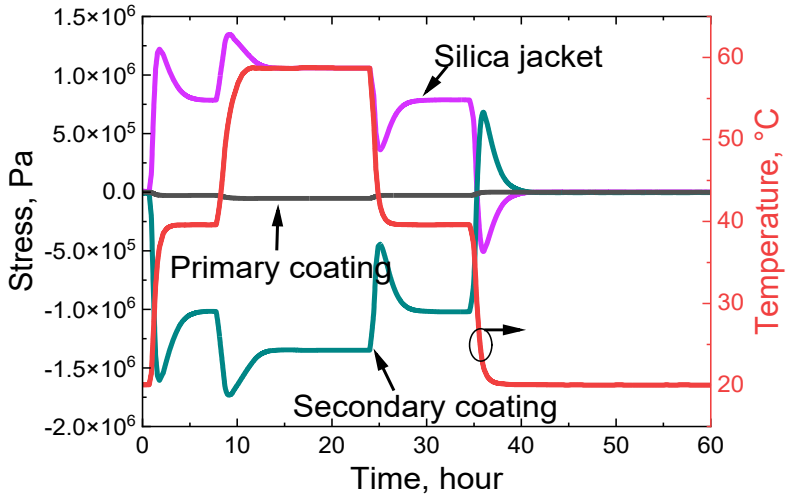

Figure 4.15 Stress partly relaxed inside the new modelled coated HCF.

4.2.3 Fitting of coating's properties

The next step is to modify the coating parameters through simulations to obtain agreement with the experimental results. This shall allow us to acquire more accurate data on coating parameters that reflects the real performance of the used fibre coating. There are three coating properties that mainly decide the phase change and its relaxation, which are thermal expansion coefficient (TEC), Young's modulus, and relaxation time. TEC mainly influences the absolute phase change. Since the stiffness of the coating is decided by Young's modulus, where a harder coating can pull the fibre more effectively, Young's modulus also strongly influences the absolute phase change. Relaxation time alters predominantly the relaxation process, e.g., the phase peak value (the 'overshoot') during temperature change and the stabilized time. As mentioned before, a function of temperature will be used, which is strongly estimated by fitting it to the relaxation steps at 20°C, 40°C and 58°C.

Since in the temperature range we consider (20°C-58°C, as given by the experiment), the primary coating is in the soft, rubbery state (small Young's modulus), its "pulling effect" on HCFs is significantly weaker than the secondary coating [117], which has Young's modulus about two orders of magnitude higher. Thus, coated HCF behaviour is expected to be more dependent on the secondary coating rather than the primary coating. For example, as shown in Figure 4.16, changing the primary coating TEC by 10 times (e.g., from 863 ppm/°C to 86.3 ppm/°C) brings negligible change to the phase change behaviour. However, changing the TEC of the secondary coating by as little as 2 times (e.g., from 120 ppm/°C to 60 ppm/°C) results in a significant change in both phase change values and relaxation-caused "overshoot". This simplifies the fitting, as only secondary coating parameters must be varied. On the other hand, this does not allow us to fit reliably the properties of the primary coating.

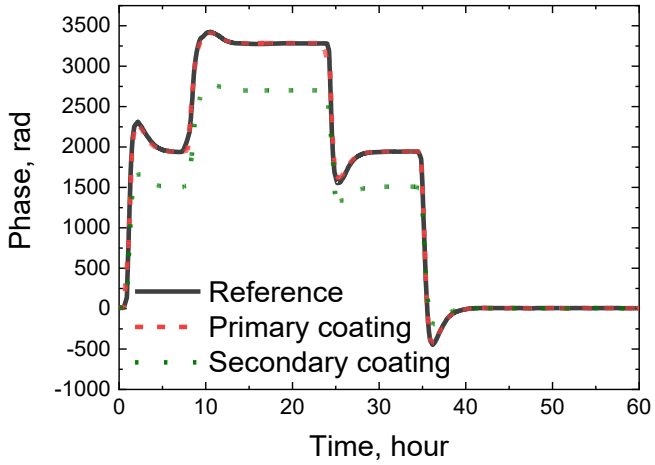

Figure 4.16 Phase change caused by the change of TEC of primary coating/secondary coating (Primary coating: 10 times reduction of the TEC based on the reference; Secondary coating: 2 times reduction of the TEC based on the reference;).

Since relaxation time decides the phase (stress) relaxation, it was firstly fitted to make it match the relaxation changes at 20°C, 40°C and 58°C. During the fitting process, initial values were provided for each temperature step, and these values were interpolated to create a smooth curve for the targeted parameter. Considering the fact that larger time constant leads to a longer relaxation, the parameter was then adjusted separately for each step until all steps reached a reasonable agreement with the experimental data. As shown in Figure 4.17, by increasing relaxation time, the phase takes longer time to relax and the modified relaxation time contributes to a better fitting regarding the phase relaxation rate. The modified relaxation time will be shown later.

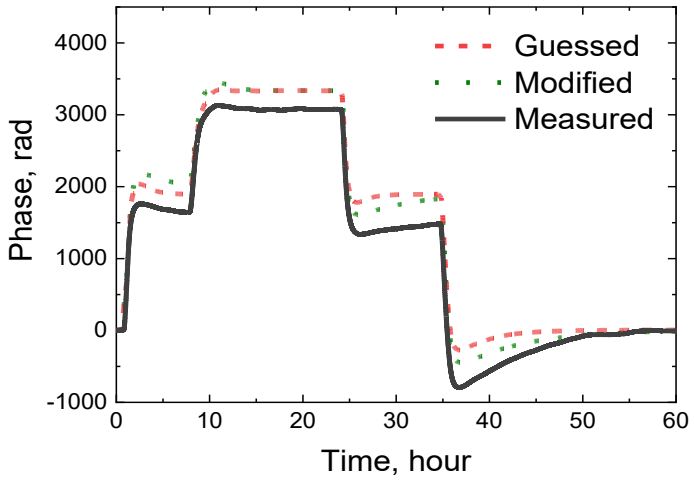

Figure 4.17 Simulated phase change after we modified the relaxation time.

With an improved relaxation time input for the model, the TEC of secondary coating was then adjusted, which narrows the gap of the stable phase change between the simulated and measured phases. As shown in Figure 4.18, the TEC is already reduced by 25%, which, however, still shows a quite significant difference with the measured curve. We turned to adjust the TEC of silica jacket and it can be improved significantly, as shown in Figure 4.19.

The reason we did this is because the TEC of silica jacket has been demonstrated to be temperature-dependent, with a range varying from 0.3 to 0.55 ppm/°C [34, 110-112].

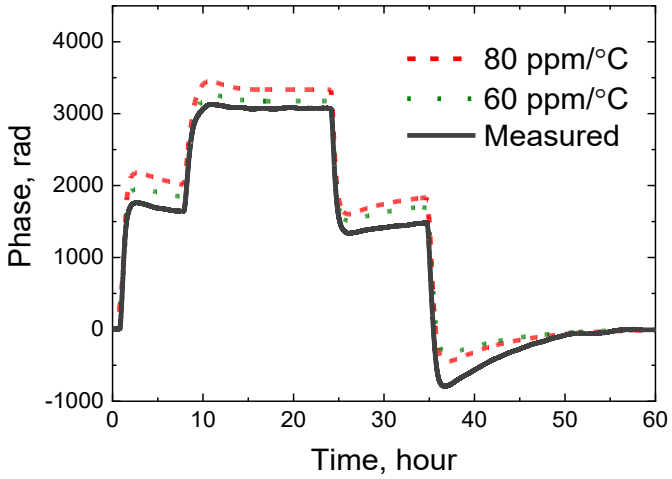

Figure 4.18 Simulated phase change after TEC of secondary coating was reduced.

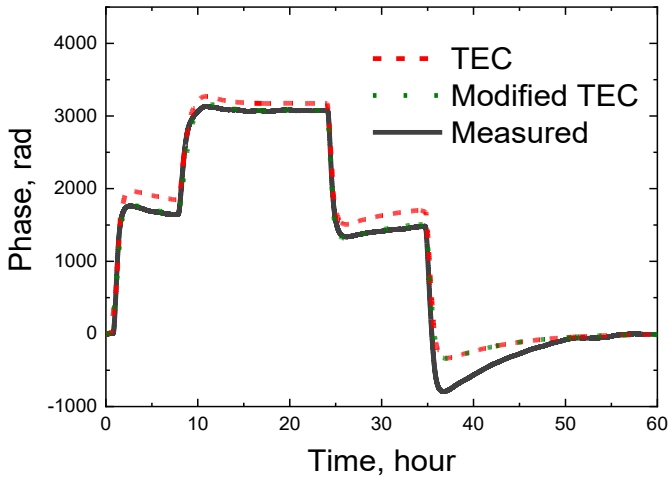

Figure 4.19 Simulated phase change after we reduced the TEC of silica jacket.

As shown in Figure 4.19, a very good fitting at the first three steps have been achieved. However, the phase peak at 20°C has been improved very limitedly with the above adjustments. Thus, Young's modulus, especially at 20°C, is increased. This is because stiffer coating can pull the fibre more to expand. Finally, by adjusting the three parameters of the secondary coating and the TEC of silica jacket, we achieved a good agreement between the simulations and experimental results, as shown in Figure 4.20.

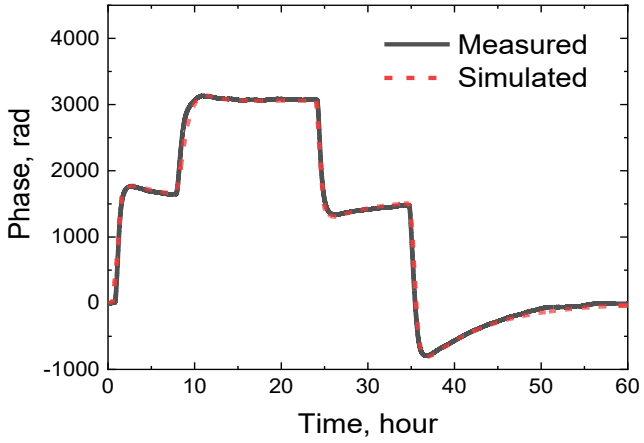

Figure 4.20 Simulated phase change with the increased Young's modulus of secondary coating.

The material parameters that give the best fit are shown in Figure 4.21. For the fitted Young's modulus of the secondary coating, it is increased less than threefold at 20°C and even less at higher temperature when compared to that from datasheet (in Figure 2.8). For TEC of secondary coating, it is reduced only by 25% to 60 ppm/°C compared to the typical value of 80 ppm/°C. This agrees with the reported value [118, 119], particularly when considering the secondary coating operates within its glass transition range. The fitted time constant of the coating decreases from 20000 s at 20°C to 5000 s at 58°C, indicating it is significantly temperature-dependent. We consider this reasonable, as the other coating parameters (Young's modulus, in particular) also change significantly with temperature. The fitted TEC of the silica jacket shows a slight (15%) reduction compared to the typical value of 0.55 ppm/°C, which is within the reported range (0.3 to 0.55 ppm/°C [34, 110-112]).

It is certainly arguable that there are alternative solutions that can fit the experimental result, especially when considering that the phase change/thermal expansion is simultaneously dependent on both TEC and Young's modulus. However, we believe the obtained parameters are reasonably valid for the tested HCF as they, after moderate adjustments, follow expected trends and fall within reasonable ranges suggested in literatures. The obtained parameters would be practically useful to HCF users when such data might not be available, in particular the time constant.

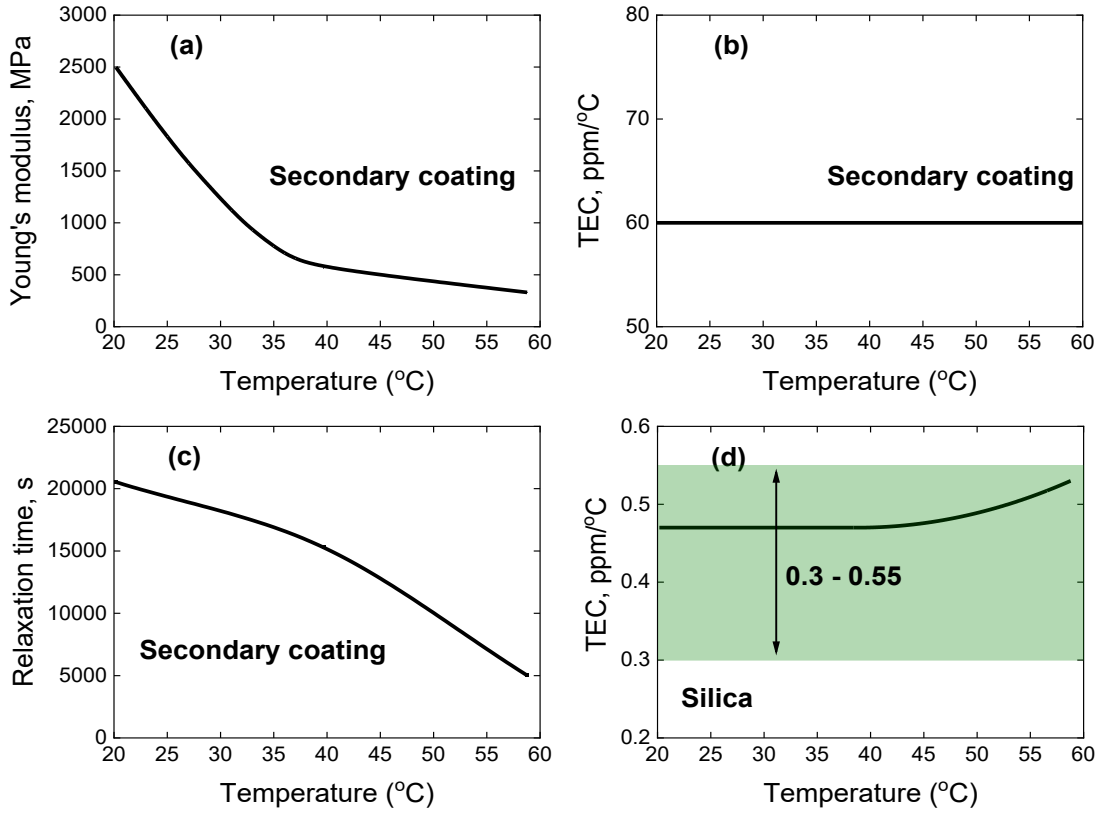

Figure 4.21 The fitted parameters (a) Young's modulus of the secondary coating (b) TEC of the secondary coating (c) Relaxation time of the secondary coating (d) TEC of the silica jacket.

4.3 Conclusion

It has been discussed in this chapter that coating changes the overall thermal sensitivity of HCFs in two effects. Firstly, coatings can cause significant change on the thermal sensitivity of HCF (increase), as it expands significantly more than silica. Secondly, heating coated fibres creates stress due to the different expansion coefficients of the silica jacket and coating. Once temperature stabilizes, this stress is partly relaxed, resulting in phase relaxation, due to the viscoelastic characteristics of the coating. This was confirmed with simulations, which qualitatively described all effects observed in the experiments. Finally, we fitted our simulation to the measured result by adjusting the parameters of the secondary coating and silica jacket, which agrees well with experimental result. Compared to the data provided by coating manufacturer, the fitted parameters, particularly the time constant, enable us to better predict behaviour of such coated HCFs. Furthermore, the built model provides a comprehensive framework for understanding and predicting not only the thermal behaviour, but also for developing coated HCFs with enhanced performance, such as reduced micro-bending loss [120].

Chapter 5. Thermally insensitive HCF coil

The target of studying coating's influence is to find novel approaches to eliminate this influence. In this chapter, we suggest and design a coated HCF support-free coil with a reduced thermal sensitivity and potentially zero thermal sensitivity. Firstly, a COMSOL coil model is built to verify this idea. Subsequently, we investigate the influence of four coil parameters (number of turns, coil diameter, number of layers, and the fibre gap) on coil performance and design coil with minimized thermal sensitivity. Finally, a coated HCF coil is made, and then experiments are conducted to characterise the designed coil.

5.1 Principle of operation

In fibre optic gyros, winding the sensing coil in a specific pattern, e.g., quadrupolar (QAD) winding pattern, octupolar winding pattern and cross winding pattern [121], helps to create symmetrically distributed thermal gradients within the coil. This effectively reduces unwanted thermally induced nonreciprocity (commonly known as Shupe effect [25]). However, temperature variations produce thermally induced stress and subsequent fibre coil deformation, especially when the coil is tightly winded. Thus, designing a gyro coil requires understanding of its mechanical properties under temperature variations to minimize this effect, which has been studied quite extensively.

In such a fibre coil, the distinct mechanical characteristics of the silica glass and the fibre coating materials create a composite, orthotropic material. This composite exhibits varying stiffness and thermal expansion, leading to diverse regimes of overall behaviour. The interplay of these mechanical properties within the coil introduces complexities that give rise to different mechanical responses and thermal expansion patterns [122]. Interestingly, for certain coil geometries and coating material properties, thermal expansion in such a coil can be negative for the inner layers and positive for outer layers, and crossing zero inside the coil. This zero thermal expansion is of little relevance to the phase stability of a signal in a standard optical fibre, as its stability is predominantly given by the thermo-optic effect. However, it is of interest in HCFs, where signal phase stability is dominated by this elongation. Given the inner layers have negative thermal expansion coefficient and the outer layers a positive one, it is believed to be possible to achieve a zero thermal sensitivity by using only a certain number of selected layers in the spool.

5.2 Toy model

To illustrate the principle of the proposed method, a simplified toy model has been employed to simulate the thermal expansion. This model comprises a cylindrical shell with two layers composed of distinct materials. The 3D cylindrical shell is represented using a 2D axisymmetric model implemented in COMSOL Multiphysics. Details of the model and its parameters, selected randomly, are outlined in Figure 5.1. To restrict the scope of the simulation, boundary conditions at the top and bottom are set to enforce zero expansion in the axial direction. This approach simulates an infinite cylindrical shell, ensuring that the thermal expansion is fully directed in the interested direction. To increase the possibility for negative thermal expansion, the inner layer is modelled with a material that has a large thermal expansion coefficient (DP1021, DeSolite®), while the outer layer uses silica glass as it has a small thermal expansion coefficient.

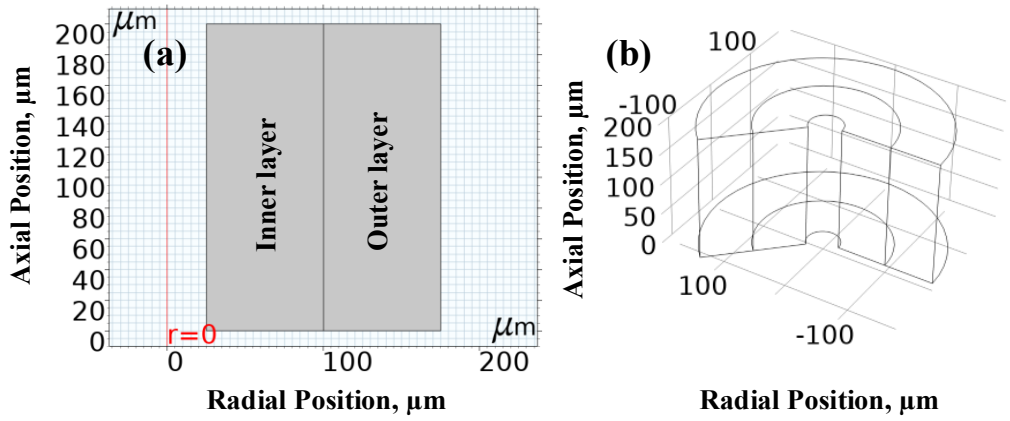

Figure 5.1 A 2D axisymmetric model (a) used to simulate a 3D cylinder shell (b). It is made of an Inner layer (Young's modulus = 0.55 MPa; TEC = 863 ppm/°C; thickness= 75 μm); and an Outer layer (Young's modulus = 73100 MPa; TEC = 0.5 ppm/°C; thickness= 75 μm).

The initial temperature is set to be 30°C and subsequently raised to 40°C. While operation at room temperature is preferred, the 30°C-40°C range, which is slightly above room temperature, was chosen because it is relatively easier to control the chamber by simply heating it without the need for cooling. In Figure 5.2, the deformation is illustrated by arrows indicating the direction of the deformation, and the circumferential stress distribution is color-coded at the cross-section of the two-layer shell. Notably, as the outer layer undergoes expansion in both its inner and outer diameter, a distinct behaviour is observed in the inner layer. Specifically, while the outer diameter of inner layer expands by 2.0 nm, its inner diameter experiences a contraction, shrinking by 14.7 nm.

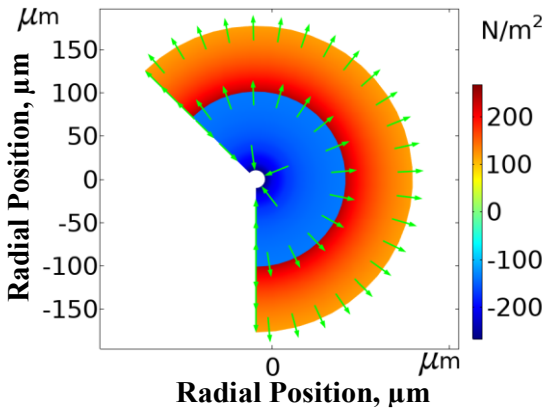

Figure 5.2 Deformation and circumferential stress distribution of the two-layer cylinder shell cross section (temperature change: 30°C - 40°C). Here, the arrows show the deformation direction. The inner side of the Inner layer shrinks, introducing a negative inner diameter change of -14.7 nm (negative stress), while the outer boundaries of the Inner layer and Outer layer both expand (by +1.2 nm and +2.0 nm, respectively, positive stress).

This phenomenon can be understood intuitively by considering the expansion of each layer: the outer layer, characterized by a low TEC, effectively constrains the inner layer with a higher TEC. As a result, the inner layer is compelled to expand in the only available direction, which is inward. This has been confirmed by the stress distribution shown in Figure 5.2.

5.3 Coil model and Simulation

Our coil structure exhibits a greater degree of complexity compared to the previously described two-layer cylinder shell. Nonetheless, as demonstrated later, it also achieves a zero-expansion point through the interaction of materials with distinct thermal properties.

Our HCF consists of four materials: air, silica glass, primary coating, and secondary coating. As explained earlier in Figure 4.7, the influence of the HCF microstructure used for light guiding is neglected in our model. This is because the microstructure contains a minimal amount of glass, making its thermal and mechanical properties insignificant in affecting the overall thermo-mechanical properties of the HCF. Consequently, the simplified representation of the HCF structure includes four layers, as shown in Figure 4.7.

Previous work in [122] demonstrated that a coil composed of multiple materials can behave similarly to the cylindrical shell model. Here the strands of non-compliant, low-TEC silica distributed through the composite coil structure constrain the high TEC polymer coating. This interaction effectively forces the innermost layers inward, resulting in compressive circumferential strain.

For the coil model, we adopt a 2D-axisymmetric model, effectively simulating each fibre turn as a solid torus of glass enclosed by hollow torus of coating material. While in practice, the fibre coil is a layered helix, this torus model gives a faithful representation of the coil

behaviour while providing a significant reduction in the required simulation size. Due to the symmetry about the coil mid-plane, the model can be further simplified to a semi-coil model, as shown in Figure 5.3. This helps reduce the computing time.

The model, as seen in Figure 5.3, is a semi-coil that has five layers and eight turns per layer, which is wound in a 100-mm inner diameter. We show the used properties of the materials of the fibre, as listed in Table 5.1. Here, coils made of both a bare HCF (Figure 5.3 (a)) and coated HCF (Figure 5.3 (b)) are built to further highlight the difference in stress experienced by composite versus mono-material structures.

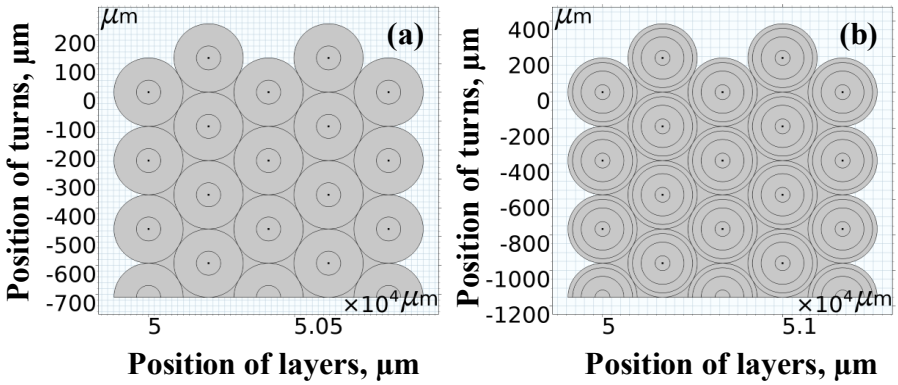

Figure 5.3 The built HCF semi-coil model made with (a) bare HCF and (b) dual-coated HCF. (Coil diameter: 100 mm; number of layers: 5, materials shown in Table 5.1).

Table 5.1 Typical material properties of optical fibre and their coatings, as considered in our simulations.

Parameters	Silica Jacket	Primary coating	Secondary coating
Young's modulus (MPa)	73100	0.55	700 (20°C) 520 (40°C) 470 (60°C)
CTE (ppm/°C)	0.47	363	80
Poisson's ratio	0.17	0.37	0.37
Density (kg/m^3)	2203	1030	1130

In the simulation, temperature is changed from 30°C to 40°C and changes are recorded of the diameters in the air cores at each layer. The average change in the circumference of each layer is then calculated, as depicted in Figure 5.4. In the scenario where the coil is composed of air and silica glass alone (bare HCF), all coil layers exhibit similar elongation, aligning with expectations. However, the behaviour is different for the coated HCF and is

akin to the two-material cylinder model. In this case, the first layer contracts, the second experiences nearly negligible length change, while the outer three layers expand. This distinction in performance is further evident in the circumferential stress (hoop stress) distribution illustrated in Figure 5.5. The bare HCF model shows zero stress, whereas the coated HCF model exhibits a complex stress distribution: negative stress in layer 1, close to zero stress in layer 2, and positive stress in layers 3, 4, and 5.

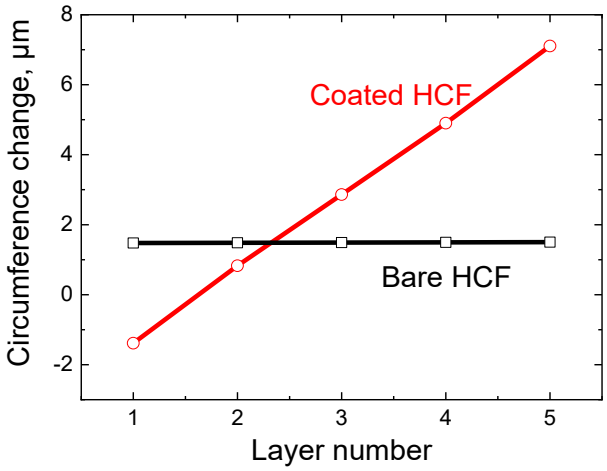

Figure 5.4 The calculated average circumference change of each layer in a HCF coil following the model shown in Figure 5.3 (bare HCF, black dots; dual-coated HCF, red circles; temperature change: 30°C - 40°C).

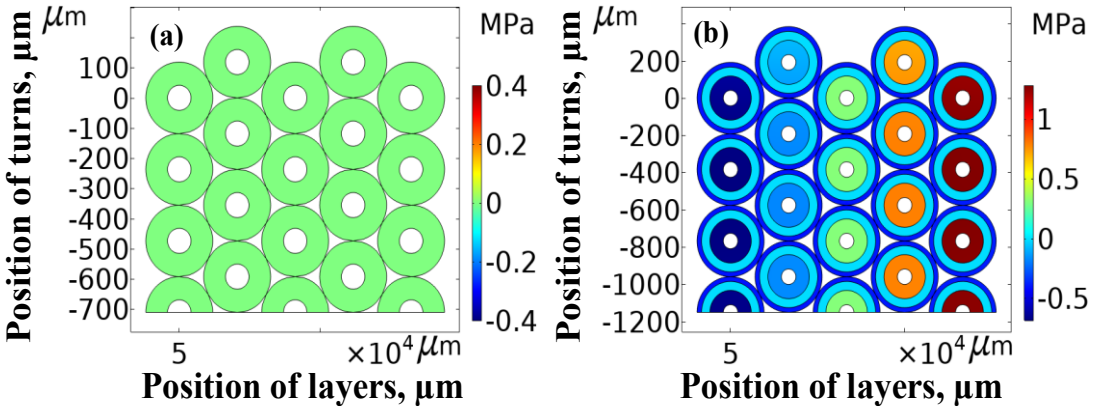

Figure 5.5 Circumferential Stress distribution of the model in Figure 5.3 (a) bare HCF (b) dual-coated HCF.

To obtain a fibre path with minimal net thermal sensitivity, we use the *N* inner layers of the coil that, when concatenated, have near-zero change to the total length. As demonstrated in Figure 5.6, it shows the fractional change in path length for concatenated layers (starting from the innermost layer 1). For comparison, the uncoiled HCF behaviour is also shown, in which the thermal expansion is unconstrained and thus constant.

For the HCF coil modelled here, the combined length change of layers 1 and 2 results in a near-zero length change over temperature. To build a fibre path having minimal thermal sensitivity, only the layers that exhibit minimal thermal expansion (layers 1 and 2 in this

example) are used for light propagation. The remaining layers (3, 4, and 5) do not guide light and serve only to maintain the inner layers at minimum thermal expansion.

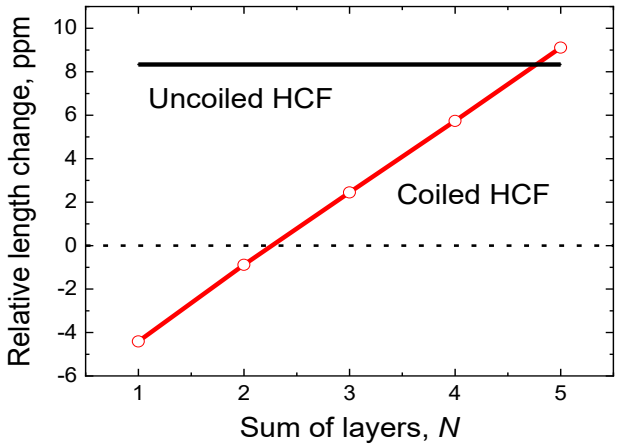

Figure 5.6 The calculated relative length change of the dual-coated HCF coil (temperature change: 30°C - 40°C). For coiled HCF (red circles), this change is shown for the inner *N* layers of the 5-layer coil (Figure 5.3 (b)). The change of uncoiled HCF is shown as a black solid line for comparison.

Although the above example uses only two of five layers, various coil geometries and combinations of material properties can result in structures where compressive and tensile strains are more balanced around the radial midpoint. This creates a minimum thermal expansion path that is closer to the entire coil length. Our primary objective is to maximize the utilization of the HCF path. Therefore, our figure of merit, referred to as "coil performance" (*R*), is defined with the goal of optimizing the entire HCF length.

In the example above, two out of five layers are used for light guiding, resulting in $R = 2/5 = 0.4$. In the following sections, we explore the maximization of *R* by examining its dependence on various coil parameters. These parameters include the number of turns, the number of layers, the coil diameter, and the gap between fibres in consecutive turns, as seen in Figure 5.7. The aim of the simulation is to understand how adjusting these coil parameters can optimize the figure of merit (*R*) and enhance the overall performance of the coil.

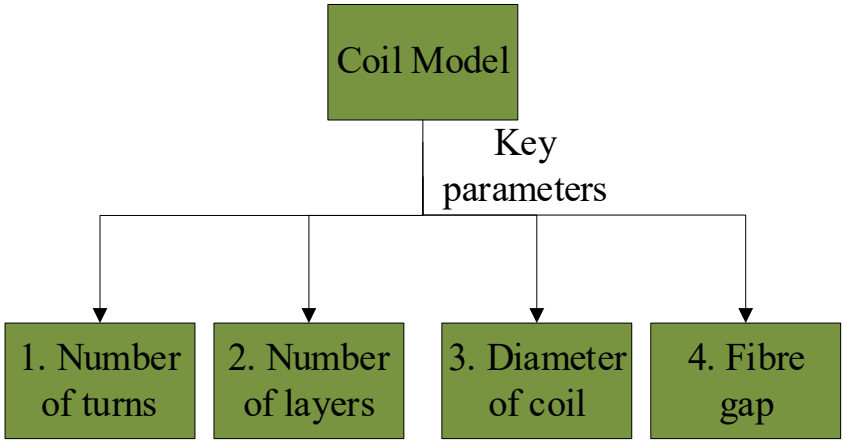

Figure 5.7 Key coil parameters.

5.3.1 Number of turns

In general, the coil experiences unconstrained conditions at the top and bottom surfaces, resulting in the primary mechanical constraint being applied solely in the radial direction. It is expected that, within a given layer, the axial position of the turn has minimal influence on its circumferential strain. This assumption finds support in the calculated results depicted in Figure 5.8, where the model illustrated in Figure 5.3 (b) is extended to up to 32 turns. Consequently, for subsequent analyses, we exclusively employ the 4-turn model (as shown in Figure 5.3 (b)), which is computationally efficient. It will be used in the following sections to investigate the dependence of coil performance on parameters of coil diameter, number of layers, and fibre gap.

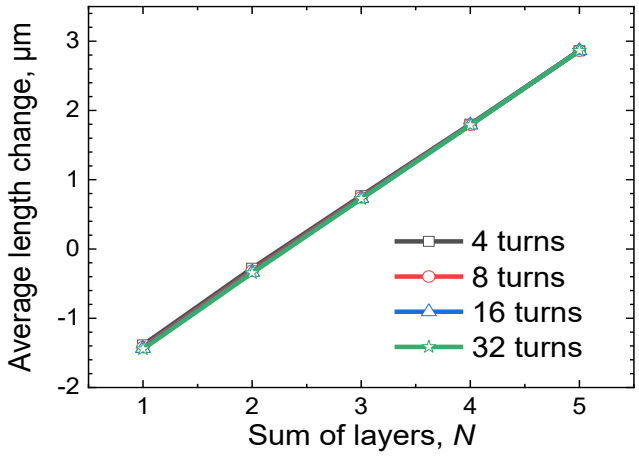

Figure 5.8 Average length change per turn per layer in layers 1 to *N* (Sum of layers) for different number of turns (coil diameter: 100 mm; number of layers: 5; temperature change: 30°C - 40°C).

5.3.2 Coil diameter and number of layers

The diameter and layer count of the coil is constrained by the volume requirements of the application for large coils, and the bend-loss performance limits for small diameters. To keep the analysis within practical limits, coils with diameters ranging from 70 to 300 mm are considered. As shown in Figure 5.9, it illustrates the coil performance (R) as a function of the total number of layers (N_{tot}) across this range of coil diameters. Initially, the coil performance R increases with the total number of layers, which can be understood by considering that when the coil has only a few layers, particularly in the case of a single layer, there is no constraint from surrounding layers. As more layers are added, the inner layers become increasingly constrained by the outer layers, thereby increasing the coil performance. However, as the number of layers continues to increase, the desired effect gradually decreases, likely because the outermost layers contribute less to the overall constraining effect. This phenomenon can also be explained by the fact that sufficiently

large diameters (with more layers) approach a "near-flat" configuration, where the "coil effect" is diminished. This might also explain why the maximum *R* occurs later for larger diameters.

In short, this simulation provides guidance in selecting the optimum number of layers once the coil diameter for an application has been determined. For example, for a coil diameter of 100 mm, N_{tot} is predicted to be around 13, achieving a coil performance *R* of 0.69. Although the maximum achievable *R* varies slightly with coil diameter, the differences remain moderate (e.g., R_{max} = 0.67 for 70 mm coil diameter versus 0.69 for the 300-mm coil).

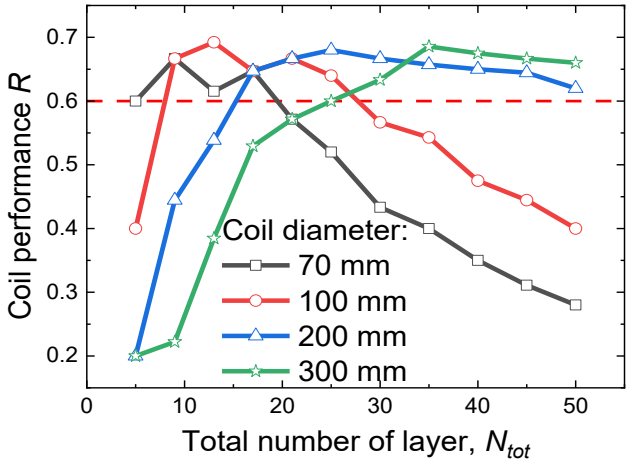

Figure 5.9 Simulated coil performance *R* for different total number of layers N_{tot} and coil diameters of 70 mm (black squares), 100 mm (red circles), 200 mm (blue triangles), and 300 mm (green stars) (temperature change: 30°C - 40°C).

5.3.3 Fibre gap

When winding an optical fibre, a gap was intentionally introduced between adjacent turns to enable a smooth and regular winding pattern. In Figure 5.10, we model this gap and show how it influences coil performance *R*. Here the results indicate that the zero gap gives the best performance, corresponding to the most compact winding pattern. As the gap increases, the performance *R* diminishes, reaching a value of approximately 0.4. However, as the gap continues to increase, the performance *R* improves again, which is possibly due to the change in coil compactness. The exact reason for this behaviour, however, is not examined. It is also expected that the performance could improve when a filler (glue) with optimized properties (Young's modulus and TEC) is applied in between the fibres.

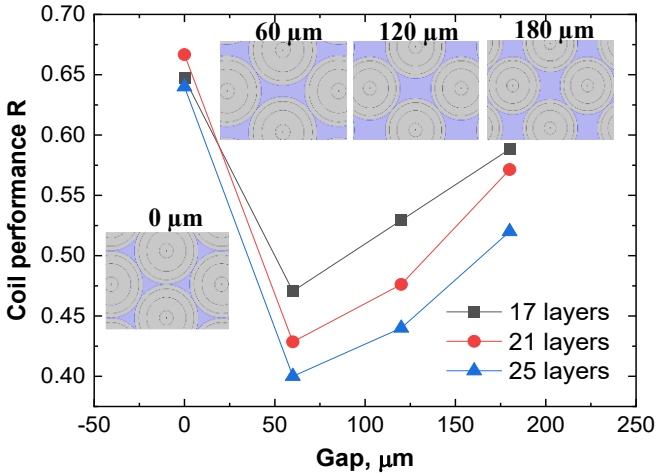

Figure 5.10 Simulated influence of the gap distance on coil performance *R* (coil diameter: 100 mm) (temperature change: 30°C - 40°C).

5.4 HCF Coil-winding and updated simulation

The HCF used is a standard dual-coated NANF. To select an optimum subset of the HCF path for experimental purposes, simulations have been conducted utilizing the parameters corresponding to the as-coiled configuration, as outlined below.

To prepare a “support-free” HCF coil, the fibre was wound onto a 160 mm diameter spool, which was subsequently removed from the centre of the coil to leave a freestanding structure, bound in places with tape/string to keep the outer layers from popping out. It is worth mentioning that this was initially studied for use in fibre gyroscopes, where glue would typically be applied for long-term stability. However, in this proof-of-concept experiment, we intentionally avoided using glue to simplify the coil-winding process. In practice, we did not observe significant fibre shifting, primarily due to the sticky coating of the fibre, as evidenced by the phase-time curves.

Although a zero gap in coil winding is ideal, it requires very precise control and is practically very challenging. Therefore, the gap was, after discussing with my colleague who made the coil, set to be 116 μm (400 μm between adjacent fibre centre). On average, there are 57 turns in a single layer.

Based on the coil parameters (gap and turn number), coil performance *R* can then be calculated as a function of the used HCF length (a certain number of coil layers), which is shown in Figure 5.11. It is worth mentioning that the coating’s relaxation effect is considered for the coil performance calculation. We observe a rapid increase in *R* with the length of the HCF up to a length of 485 m, at which point it reaches a value of $R = 0.53$. Beyond this, R only increases to 0.58 at a length of 544 m before slightly decreasing, reaching $R = 0.56$ for an HCF length of 717 m. In the experiment, the used HCF (6-element NANF, 1.6 dB/km at

1550 nm) is 548-m long, a length determined from the simulations to achieve maximum *R*. Considering the discussed coil diameter, number of turns, and the fibre gap, this fibre length can be accommodated by spooling it in 19 layers.

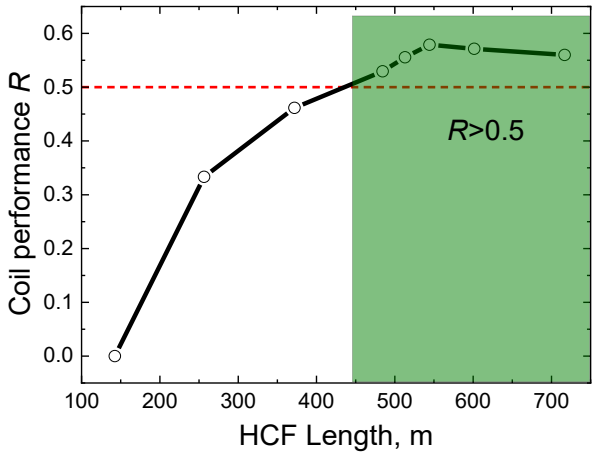

Figure 5.11 Simulated influence of the HCF length on coil performance *R* considering coil realized experimentally (diameter of coil: 160 mm; fibre gap: 116 μm, number of turns: 57).

Using the same calculation as discussed earlier in Chapter 4, the calculated (simulated) thermal sensitivity of N = 8 (layers 1-8, and corresponding R = 0.42), N = 10 (R = 0.53), N = 11 (R = 0.58), N = 12 (R = 0.63), and $N = N_{tot}$ = 19 (the whole coil), is shown in Figure 5.12. For comparison, the expected result of un-coiled HCF is also show. The minimum thermal sensitivity, closest to zero, across the entire considered temperature range is achieved when the number of turns is N = 11.

To validate our predictions experimentally, the coil was wound with access loops at layers 8 and 12. As the optimum occurs at N = 11, the model predicted thermal sensitivity of layers 1-8 is negative, while that of layers 1-12 is positive.

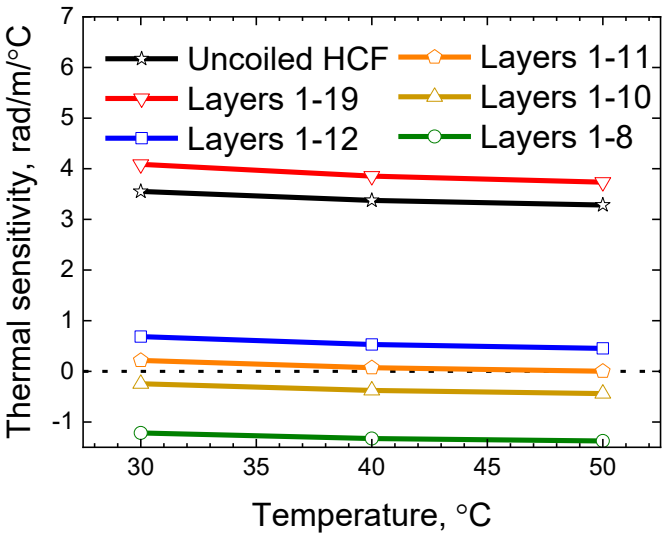

Figure 5.12 Simulated thermal phase sensitivity of the prepared HCF coil and the uncoiled HCF for comparison.

In the preparation of the coil, the fibre was initially wound (by Austin Taranta, a colleague in ORC) onto a removable bobbin following the designed pattern. Subsequently, the bobbin was removed to create a support-free coil. A photograph of the prepared coil is presented in Figure 5.13. It holds together thanks to the slightly “sticky” nature of the acrylate fibre coating. The Kapton tape was used solely to prevent the spool from breaking down during handling, and its influence is neglected in the simulations. To access the fibre of different sections (layer 8 and 12), one-meter of HCF was taken out for free access after spooling layers 8 and then after finishing layer 12 during the spooling process.

Figure 5.13 Photograph of the prepared support-free HCF coil (diameter of 160 mm; pitch of 500 µm; N_{tot} = 19; 57 turns).

5.5 Setup for Characterisation

The thermal phase change of the HCF coil was then measured using the Mach-Zehnder interferometer depicted schematically in Figure 5.14, and the detailed principle has been discussed in Chapter 3. The laser (RIO Orion from NuFern, 1558 nm) wavelength is locked to a carrier-envelope-stabilized optical frequency comb (Menlo FC1500-250) to avoid any drift and associated interference pattern changes [36]. The entry to the MZI is via a 2x2 fibre coupler and the measurement arm consists of the HCF coil spliced to the coupler pigtails while the reference arm has the coupler pigtails directly spliced together. The coupler pigtail lengths were matched in both interferometer arms, so that their contribution to thermally-induced phase delays would cancel in the detected signal. The signals from both arms were combined at a 3x3 coupler and the interference pattern detected by three photodetectors. The use of the 3x3 coupler enables evaluation of the phase, including its sign, from the detected interference fringes [97], as discussed in Chapter 3. The entire interferometer was put into a thermal chamber, where a thermometer was used to record the temperature inside.

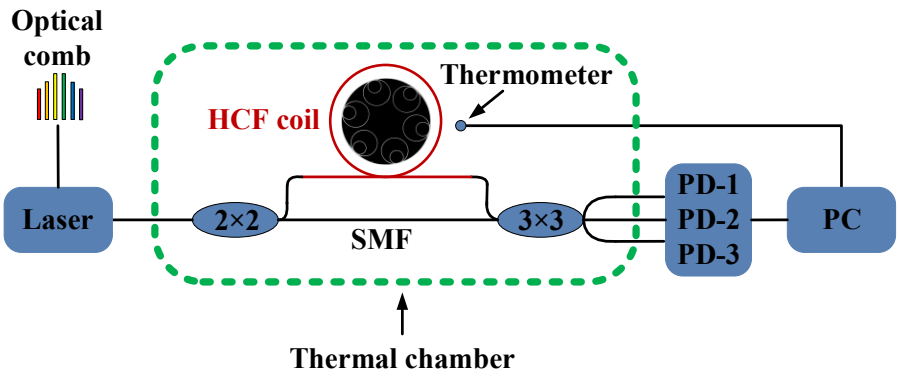

Figure 5.14 Experimental setup for thermal sensitivity characterization of the HCF coil with the insert showing the cross-section of the used HCF (PD: photodetector, laser was locked to a carrier-envelope-stabilized optical frequency comb (Menlo FC1500-250)).

5.6 Result

We first measured the thermal phase response of the whole coil (layers 1-19) over two thermal excursions from 30°C to 40°C and then from 40°C to 50°C. As seen in Figure 5.15, the phase initially increases with the temperature. However, once the temperature stabilized, the phase response steadily decreased until it stabilized after some 15-20 hours. This phenomenon of long time-constant phase relaxation arises from the coatings' viscoelastic properties, which was studied in detail in chapter 4 and the result was published in [35].

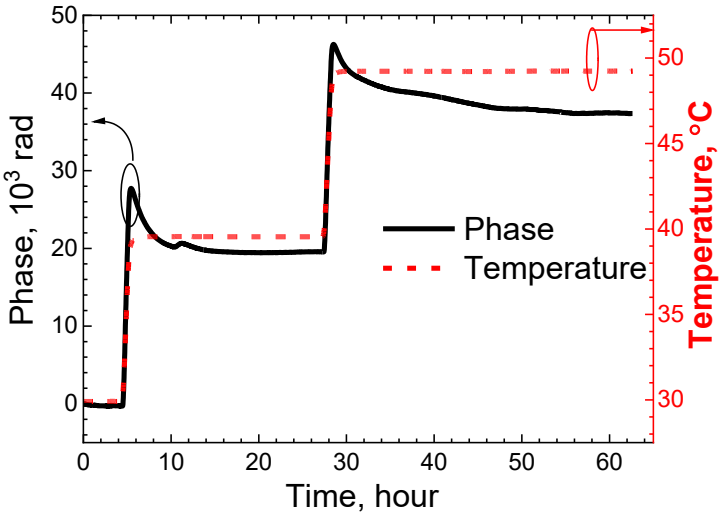

Figure 5.15 The measured accumulated phase change of the entire HCF coil (layers 1-19) when the temperature was increased from 30°C to 40°C and from 40°C to 50°C.

After this measurement, we cut at layer 12 and repeated this measurement for the aggregate path spanning layers 1-12. We then did the same for layers 1 to 8. To compare these results obtained for the three different fibre lengths, a length-normalized accumulated phase $\varphi_L(t)$ is used:

$$\varphi_L(t) = \varphi(t)/L\,, \qquad 5\text{-}1$$

where $\varphi(t)$ is the demodulated accumulated phase and *L* is the HCF length through which the light propagates. Results are shown in Figure 5.16 (temperature increase from 30°C to 40°C) and Figure 5.17 (temperature increase from 40°C to 50°C). It is worth mentioning that a small bump occurs at approximately 28 hours for the layers 1-12 in Figure 5.16, which was related to a slight temperature variation observed over the same time (shown as the inset).

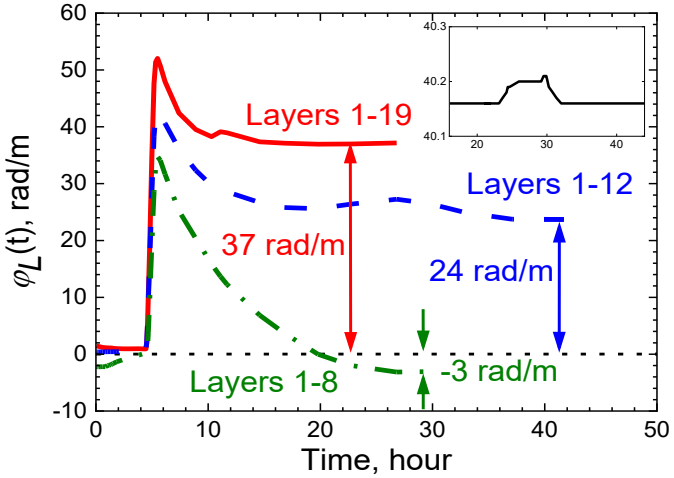

Figure 5.16 The measured length-normalized accumulated phase change for *N* = 8, 12, and 19 (temperature change: 30°C - 40°C) (The inset shows the temperature recorded for layer 1-12).

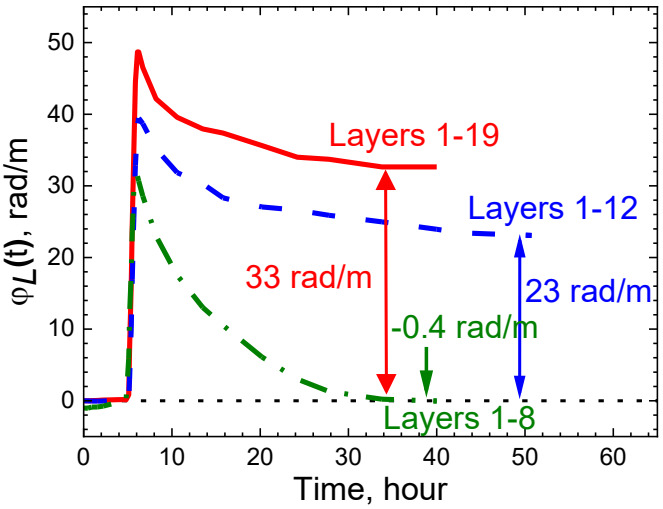

Figure 5.17 The measured length-normalized accumulated phase change for *N* = 8, 12, and 19 (temperature change: 40°C - 50°C).

To compare the results, the thermal phase sensitivity is defined as:

$$S_\varphi = \frac{1}{L}\frac{\Delta\varphi(t\to\infty)}{\Delta T_t} = \frac{\varphi_L(t\to\infty)}{\Delta T_t}. \qquad 5\text{-}2$$

where ΔT_t is a temperature change applied at t = 0. The calculated thermal sensitivity for the support-free coil is shown in Figure 5.18, as discrete points. It is shown that the thermal phase sensitivity reduces as the layer number *N* decreases from 19 to 12 and 8. For example, between 30°C and 40°C, the thermal phase sensitivity decreases from 3.8

(N = 19) to 2.4 (N=12) down to -0.3 rad/m/°C (N = 8). This corresponds to the achieved coil performance R = 0.42.

These results confirm that the fibre of a few inner layers has a negative thermal expansion coefficient. We also see that the thermal phase sensitivity decreases with temperature, reaching a value of -0.04 rad/m/°C from 40 to 50°C for N = 8. We expect we could tune this closer to zero or even achieve zero thermal sensitivity by unwinding (part of) the outer layers. We also expect we could reach the zero sensitivity at lower temperatures (e.g., room temperature) by further unwinding the other layers.

For such a designed coil of 160 mm diameter, containing 548-m HCF wound in 19 layers, 57 turns, and with a fibre gap distance of 116 μm, we achieve a nearly zero (-0.04 rad/m/°C) thermal sensitivity over a temperature step from 40°C to 50°C. This minimum sensitivity was obtained by using only the 230 m length of the inner 8 layers. To achieve high coil performance (R), options such as using proper glue, might be considered, which, however, is not studied here. The observed thermal phase sensitivity is nearly 85 times smaller than that obtained for an uncoiled HCF (3.4 rad/m/°C). Considering the thermal phase sensitivity of HCFs is already 14 times smaller than that of standard SMFs ([10]), this makes our HCF coil more than three orders of magnitude less thermally sensitive than a SMF based coil. In principle, an even lower value is potentially achievable by unwinding some of the outer layers.

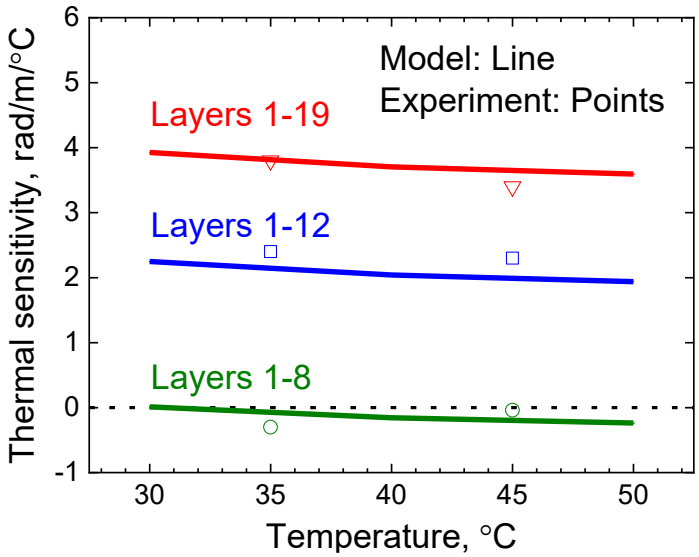

Figure 5.18 The measured thermal phase sensitivity of the HCF coil with the simulated results that considers layers 16-19 to be loose.

Compared to the predicted result in Figure 5.12, the experimental results for layer 1-8 and layer 1-12 show less reduction in thermal expansion. For example, the measured close to zero thermal sensitivity is achieved only for the fibre of the first 8 layers, which is, however, acquired already for layer 1-11 in the simulations. Despite this slight discrepancy, it is

important that the desired close-to-zero thermal phase sensitivity has been achieved experimentally.

Subsequently, it is found that a satisfactory agreement between simulations and experiments can be obtained when the top four layers from the coil (layers 16-19) are considered loose in the model (Figure 5.18), meaning they do not contribute to the coil performance (15 layer coil + non-coiled HCF of layer 16-19). This is believed to be a reasonable assumption given the coil may have become loose in coil handling despite securing the spool with Kapton tape, as we have not used any glue (which is often used, e.g., in fibre optic gyroscopes coils) and relied only on the fibre sticking together. Another possible explanation is that the used coating parameters are slightly different to those of the actual fibre.

Given the relatively high cost of the used HCF, using only part of the coil seems inefficient. To address this, filling the gaps with glue is preferred, as it offers greater design flexibility, thereby promising in maximizing the number of useful layers. Another straightforward option is to replace the HCF of outer layers with low-cost fibres of a similar diameter.

Similarly to the result in Chapter 4, the relaxation effect caused by the viscoelastic behaviour of the acrylate coating is observed experimentally, which, here, has introduced a temporally phase shift of as much as 33 rad/m (almost 8000 rad in the used 230-m long HCF). This adverse effect can be problematic in applications, which, as believed, can be significantly optimized when using a thinly-coated HCF in combination with a glue that would have suitable mechanical properties (low viscoelasticity in particular). Moreover, for applications in thermally isolated environments, where thermal time constants are 20 hours or longer, this technique can be employed immediately.

5.7 Conclusion

A novel method has been proposed for mitigating the thermal sensitivity of HCFs through careful selection of coiling parameters. Through the simulation and experiments, the designed coil showcased its capability to achieve zero or even negative thermal phase sensitivity. This is caused by the fibre in the inner coil layers shrinking and fibre at the outer layers expanding as temperature is increased. Considering that long fibres used in timing references and other interferometers are commonly deployed in coiled forms, this technique offers an effective solution that can be implemented through a thoughtful choice of fibre coiling geometry.

Chapter 6. Highly sensitive OTDR system

Since the backscattering power is directly proportional to the power of the launching pulse, the generation of high-power pulses is crucial for obtaining HCFs backscattering well above the noise floor of the OTDR system. Therefore, the core of this chapter is to understand pulse-related principles, including optical pulse characterisation, generation, and amplification. Finally, the approach of building a highly sensitive OTDR system will be discussed in detail.

6.1 Pulse characterisation

Before starting the pulse manipulation, it is necessary to understand the typical measurement and characterisation techniques. Several parameters are used to describe a pulse, including pulse period/frequency, pulse-width, peak power, and extinction ratio or signal to noise ratio (SNR), as illustrated in Figure 6.1.

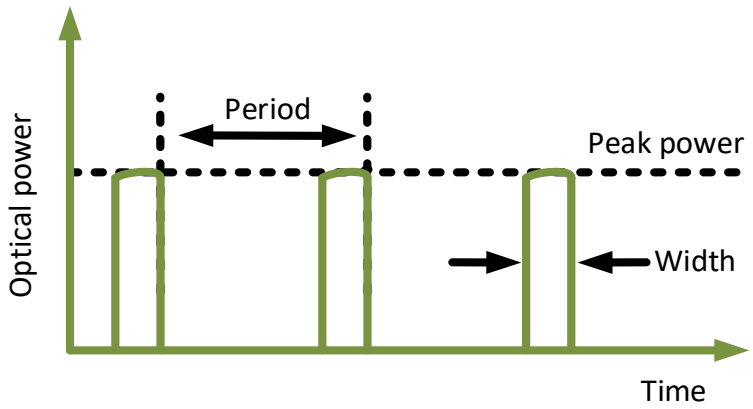

Figure 6.1 Key parameters of optical pulses

6.1.1 Short-Pulse (ns-scale) measurement

To measure a pulse, especially for ns-scale pulse, the measurement system is required to be fast enough. Here are the factors that should be considered:

(1) Bandwidth (BW) or rise time (T_r)**:**

To successfully measure a pulse, the rise time should be approximately 1/5 of the pulse width. The rise time is commonly defined in terms of the bandwidth using the equation [118]:

$$BW = {}^{\mathrm{K}}/_{T_r}. \qquad 6\text{-}1$$

K is a constant, which is typically around 0.35.

(2) Photo detector, Oscilloscope and cable:

The overall rise time of the measurement system is defined as:

$$T_{r\_final} = \sqrt{T_{r\_PD}^2 + T_{r\_cable}^2 + T_{r\_scope}^2}. \quad 6\text{-}2$$

Therefore, the measurement of a 10 ns pulse requires the system rise time to be less than 2.5 ns. With a photodetector (PD from Thorlabs, DET08CFC, 5GHz) and the a 12 GHz oscilloscope (Agilent, DSO81204B), the rise time for the system is, primarily limited by the BNC cable used, which typically has a rise time of 1.5 to 2.0 ns. Consequently, the overall system rise time is in the range of 1.1 to 2.0 ns using Eq. 6-2.

A commercial OTDR (LOR-200 from Luciol Instruments) was used for the pulse measurement and characterisation, with the measuring system shown in Figure 6.2.

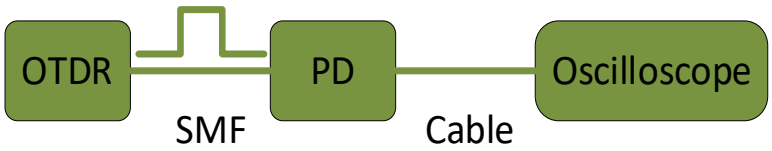

Figure 6.2 The measurement setup (PD: photo detector).

As seen in Figure 6.3, the system's response is less than 2.0 ns, which is fast enough for the 10 ns pulse measurement. Since 10 ns is the pulse width aiming to use for OTDR, providing with a spatial resolution of less than 2 meters, this system is reasonably good for our experiment. It is worth mentioning that the direct measurement provides amplitude in voltage, which has been proportionally converted to pulse power.

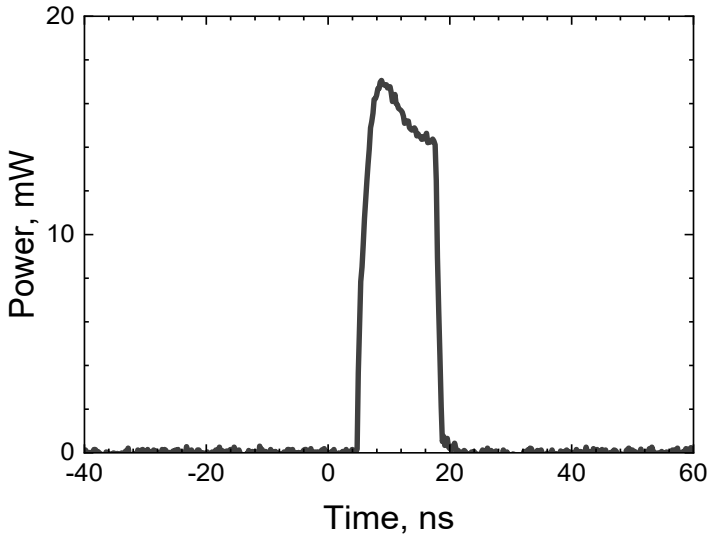

Figure 6.3 The measured pulse of 10 ns.

6.1.2 Extinction ratio

Minimizing the noise contribution to the backscattered signal requires maximizing the pulse extinction ratio, which is defined as the ratio between the peak power and the noise floor (or pedestal floor). This ratio is given by:

$$\varepsilon = 10log_{10}(\frac{P_{peak}}{P_{noise}}). \quad 6\text{-}3$$

where P_{peak} is the peak power and P_{noise} is the noise power. For a 10 ns pulse from the OTDR in Figure 6.3, the peak power is about 15 mW while the noise floor is not measurable due to the relatively high system noise.

6.2 Pulse generation and amplification

In this section, experiments will be conducted on pulse generation (ns-scale pulses) and amplification to understand the behaviour of typical optical devices and to prepare for building a highly sensitive OTDR system.

6.2.1 Pulse generation

Electro-optic modulators (EOMs) or acousto-optic modulators (AOMs) are often used for laser modulation, e.g., generating pulsed laser. EOMs operate on the principle of the electro-optic effect of some materials such as LiNbO3, where the electric field applied to the arm alters the refractive index, inducing a phase shift in the light passing through it. The combined signals from different phase then enables the modulation of light intensity. In contrast, AOMs utilize acoustic waves generated within a crystal through the acousto-optic effect, causing periodic changes in refractive index and resulting in light diffraction. The typical setup for EOM (structure of Mach-Zehnder interferometer) and AOM is shown in Figure 6.4.

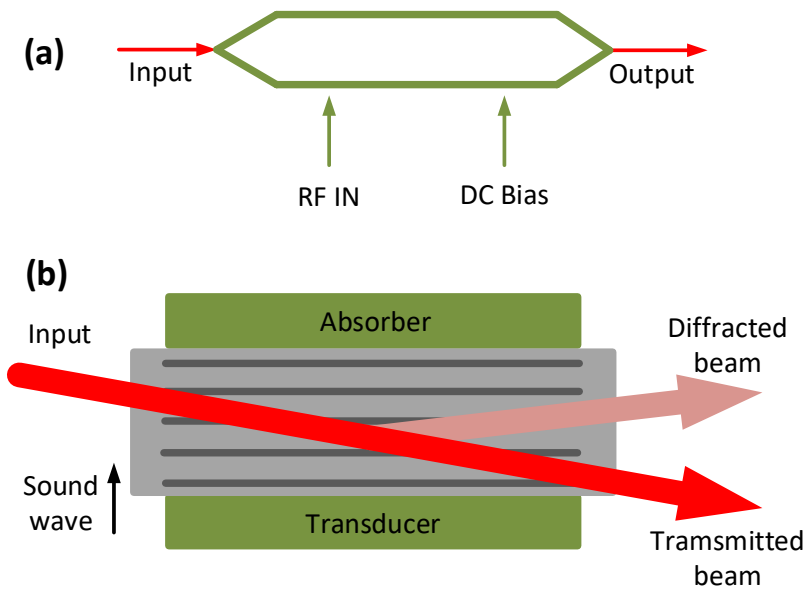

Figure 6.4 Schematic setup of typical EOMs and AOMs.

The EOM is inherently fast, with a rise time of 1 ns and below, which is because once the electric field is applied the device condition is switched. The AOM typically has a slower rise time. This is because it takes time for the transducer to start vibrating and for the acoustic waves to propagate completely through the crystal. Since the main parameter considered here is the temporal performance - rise time, which is how long it takes the device to transition from a closed state to open, EOM is used to generate short pulses. The setup of using a typical EOM (Thorlabs, LNA2124) to generate a pulse from a CW laser is shown in Figure 6.5.

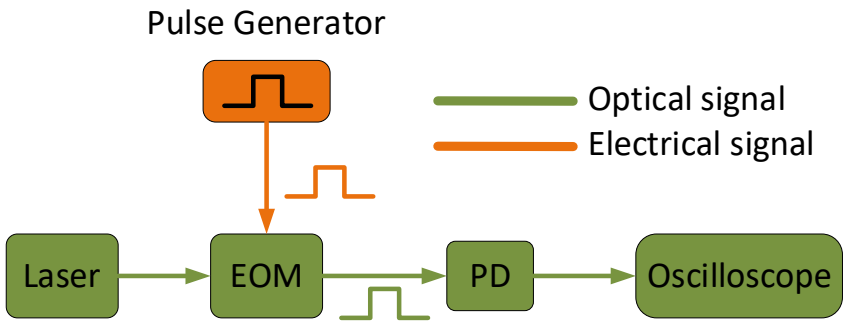

Figure 6.5 A pulse generation setup based on EOM (Laser: NKT BASIK module; PD: photodetector; EOM: electro-optic modulator).

DC voltage is applied to make the EOM work at minimum point and then RF signal from a pulse generator is applied to produce optical pulses with the same frequency as the pulse generator. The generated pulses are shown in Figure 6.6, where we show that peak power can be modified based on the RF pulse amplitude (3 V, 4 V and 5 V). Therefore, 5 V would be the highest pulse we can acquire from the setup, which produces a reasonably good pulse shape.

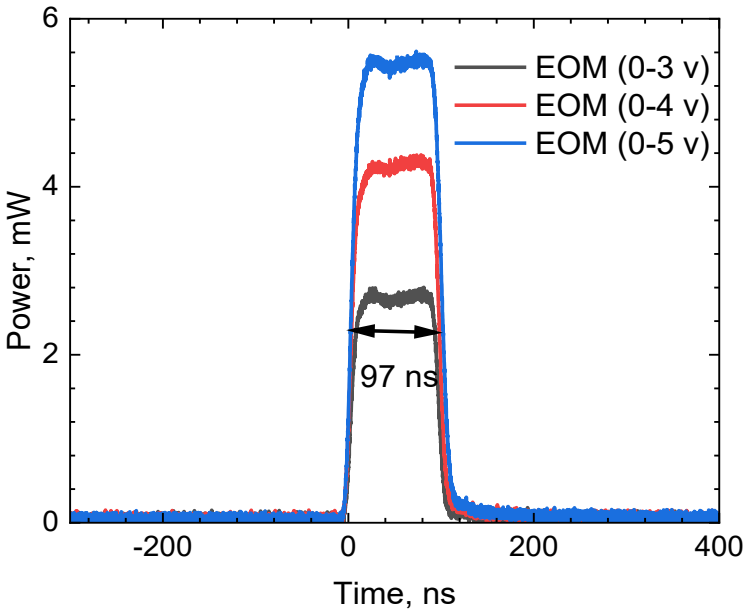

Figure 6.6 EOM's output when the amplitude of RF pulse changes.

Because maintaining precise alignment and stability in the M-Z interferometer arms is challenging and can be affected by various factors, such as temperature changes, the extinction ratio of the used EOM is usually lower (<30 dB) [123]. In contrast, AOMs generally achieve higher extinction ratios, often exceeding 40 dB and typically around 50 dB. To further reduce the noise floor, an AOM (from Gooch & Housego, rise time: 100 ns, model number: 26035-2-1.55-LTD-FO) is employed after the EOM, as shown in Figure 6.7. The second pulse generator is triggered by the pulse applied on EOM for exact control of the pulse passing. The pulse after AOM is shown in Figure 6.8. It is worth mentioning that although this AOM is relatively slow, it was used due to its availability in our lab. A fast AOM will be required in future.

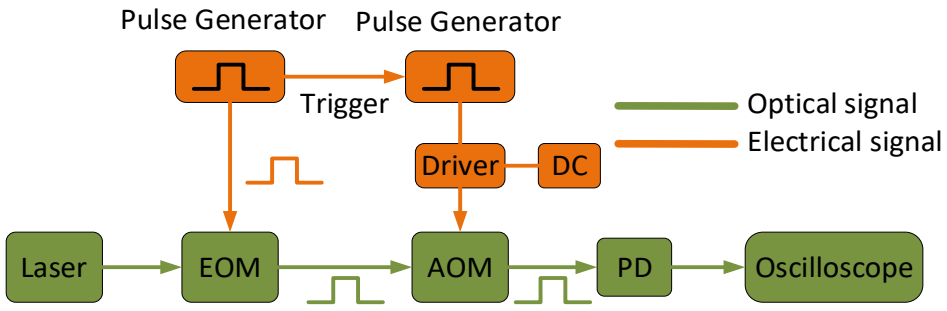

Figure 6.7 A pulse generation setup based on EOM and AOM (PD: photodetector, EOM: electro-optic modulator, AOM: acousto-optic modulator).

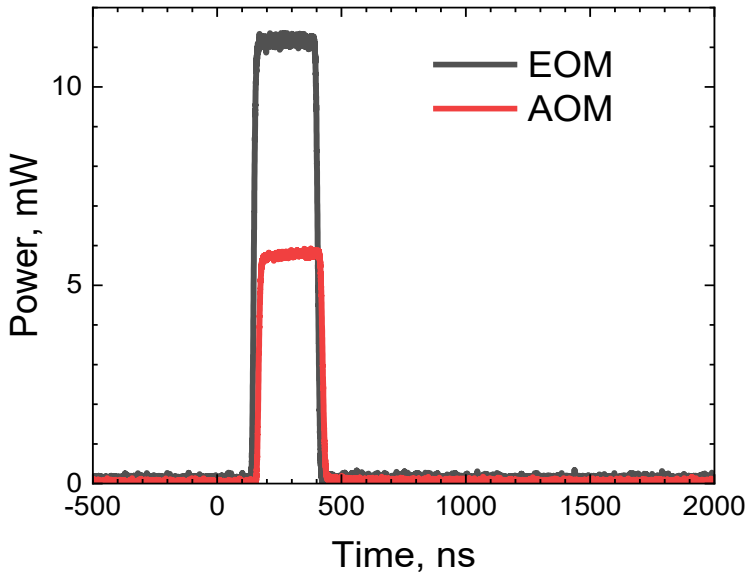

Figure 6.8 The pulses generated by AOM with the EOM output as comparison.

Here, key parameters are calculated of the two pulses generated by EOM and EOM+AOM, as seen in Table 6.1. The extinction ratio of EOM is 21 dB, which is as expected for the used EOM (> 20 dB). However, AOM output gives a extinction ratio of only 22 dB, far below the value suggested by this product of 50 dB. This is because the noise floor considered here is from the oscilloscope instead of the pulse.

Table 6.1 Key parameters of pulse.

	Peak power, mW	Pulse-width, ns	Noise floor, mW	Extinction ratio, dB
EOM	11.1	260	0.08	21
AOM	5.8	260	0.03	22

6.2.2 Pulse amplification

After obtaining pulses with EOM and AOM, we now show how to amplify pulses with commercial EDFAs. As the backscattering signal from an optical fibre is proportional to the pulse power, this part would enable us to further understand how the EDFA works and get us prepared for future experiment on building high power OTDR pulses. Based on the setup above, we used an EDFA to amplify the pulse produced by the setup in Figure 6.7, as shown in Figure 6.9. The used EDFA (FA-15 from PriTel's) has a minimum input power of -30 dBm, which allows the amplification of the low power pulse source (≈-20 dBm) as shown here.

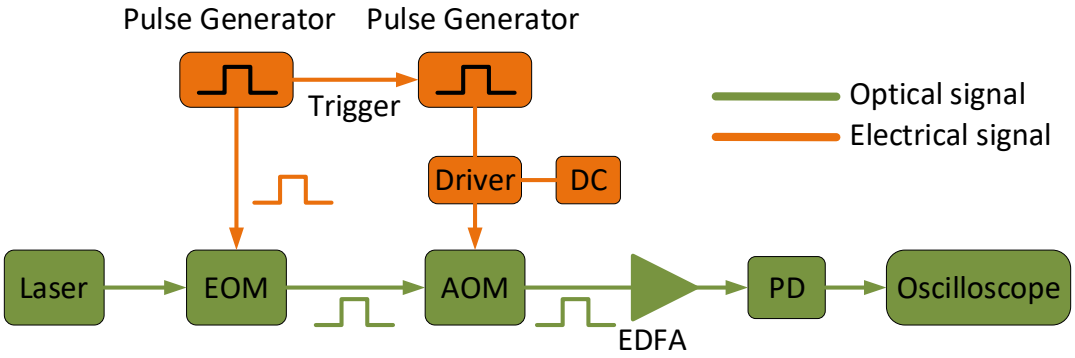

Figure 6.9 System setup for pulse amplification (PD: photodetector, EOM: electro-optic modulator, AOM: acousto-optic modulator).

The pulse to be amplified is shown in Figure 6.10. Here, the pulse width is relatively large at 260 ns, which is limited by the used AOM and pulse generator. When the EDFA is pumped on, where gain increases with the pump current, the output power and the amplified pulse of EDFA are shown in Figure 6.11 and Figure 6.12, respectively. A 20 dB attenuator was used to protect the PD from damage. Here, the pulse has been amplified by more than 20 dB when the pump current reaches 100 mA and can be further amplified, though the gain is close to saturation.

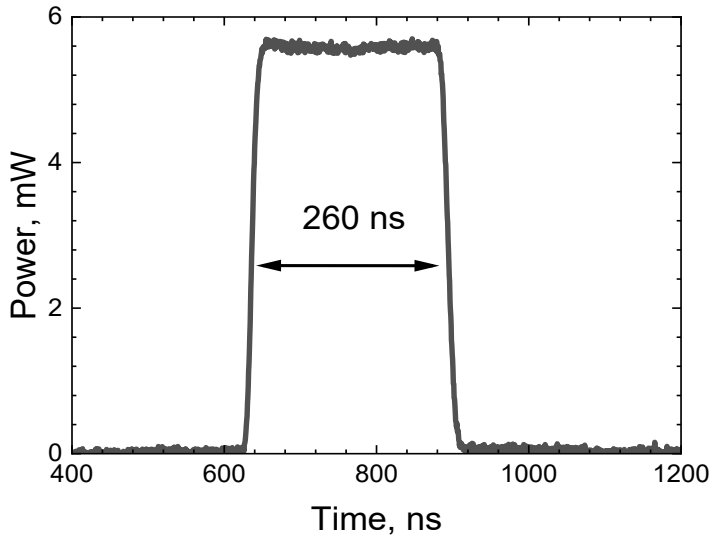

Figure 6.10 Pulse at the output of AOM 260 ns (period: 76.8 μs)

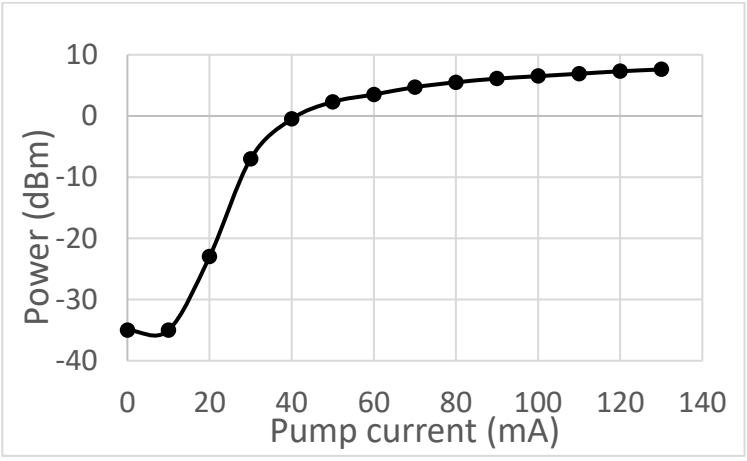

Figure 6.11 Output power of EDFA as a function of pump current.

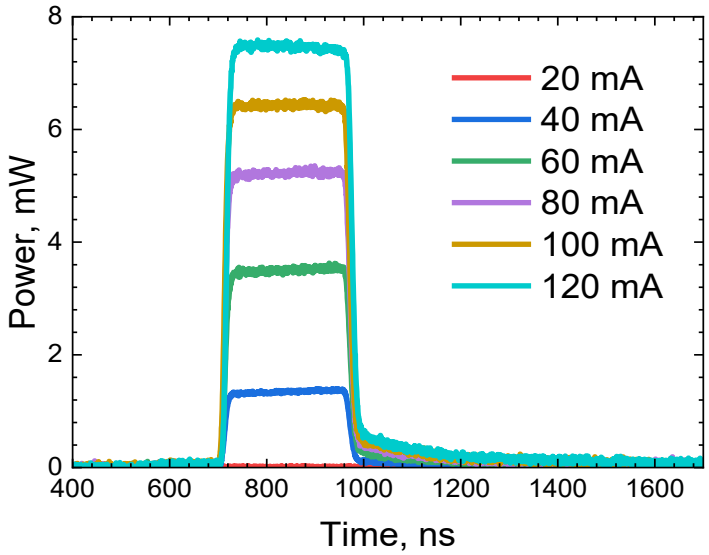

Figure 6.12 Amplified pulses with an attenuator (20 dB attenuated) applied to avoid damaging the photodetector.

As seen in Figure 6.13, the signal floor of the amplified pulses is increased to be above the system noise, corresponding to a extinction ratio of down close to 25 dB (or 300 times). This suggests a SNR of approximately 1, as the noise width is about 300 times larger than the pulse width (SNR=peak amplitude*pulse width/(noise amplitude*period)). To improve this, the noise can be reduced by employing an AOM after amplification. Otherwise, the noise level would equal the signal, resulting in a zero dynamic range for the OTDR system.

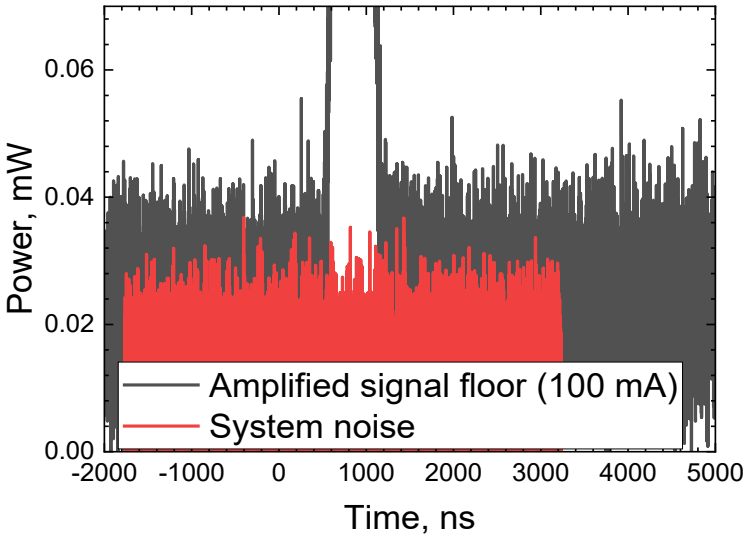

Figure 6.13 The measured signa floor and system noise.

As we show earlier, AOM is effective in improving the extinction ratio, here the EDFA is used between EOM and AOM, where AOM can reduce noise between pulses with the setup as shown in Figure 6.14.

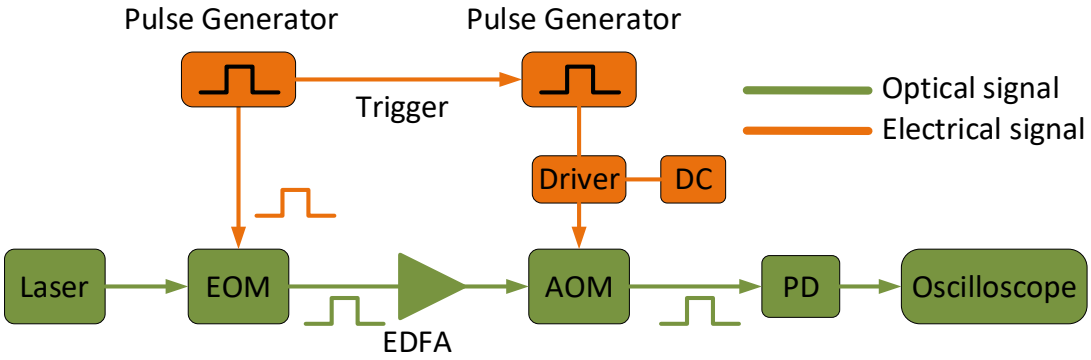

Figure 6.14 System setup for pulse amplification with AOM reducing the noise (PD: photodetector, EOM: electro-optic modulator, AOM: acousto-optic modulator).

The amplified pulse with the AOM reducing the noise floor is shown in Figure 6.15. Similarly, the pulse can be gradually amplified as the pump current increases, with slight loss due to the AOM. The pulses after EOM, EDFA and AOM are shown together for comparison, in Figure 6.16. When the pump current is at 100 mA, the pulse peak amplitude is increased by more than 17 dB, followed by a 3 dB attenuation at the AOM (red pulse VS blue pulse).

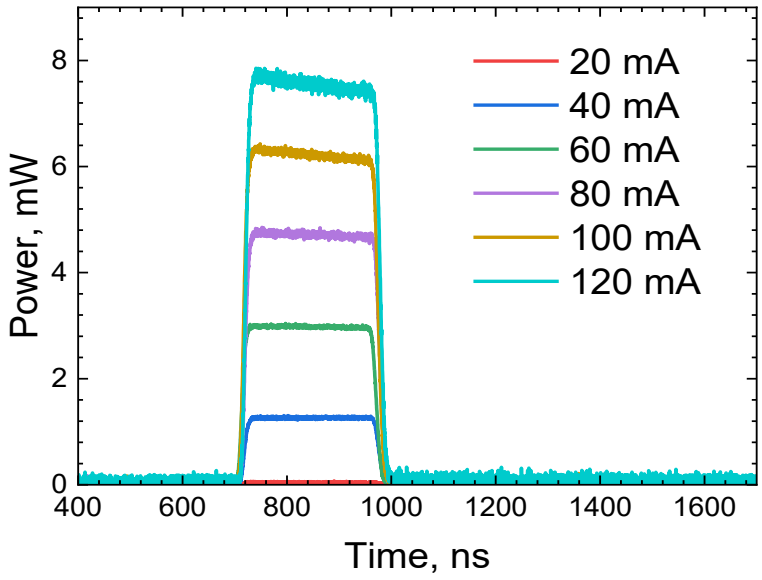

Figure 6.15 Amplified pulses with an attenuator (20 dB attenuated) applied to avoid damaging the photodetector.

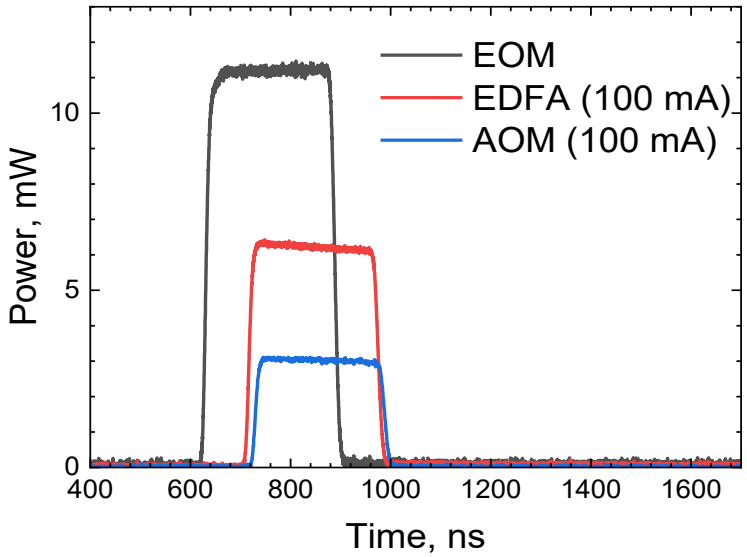

Figure 6.16 Pulses generated in the setup when EDFA works at 100 mA (here, 20 dB is attenuated to protect PD when measuring pulses from EDFA and AOM).

To demonstrate the AOM's effect in improving SNR of the pulses, The noise within the AOM window and outside are shown in Figure 6.17. With the use of AOM, the amplified noise can be significantly reduced to be below the level of system noise, achieving an expected extinction of ratio of about 50 dB. To accurately determine the extinction ratio, more precise instrumentation is required to measure the pulse's noise floor.

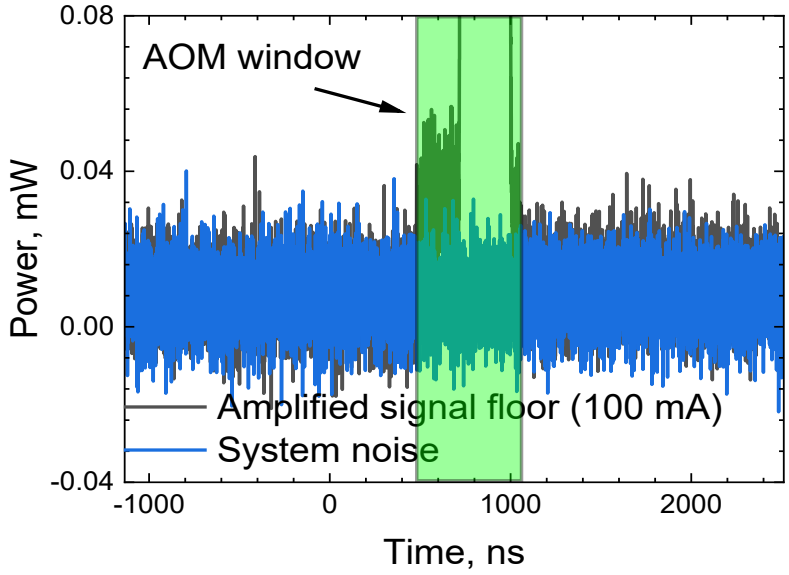

Figure 6.17 AOM's noise-reducing effect, where the noise is reduced (out of the window).

As shown in Figure 6.17, there are two noise levels, the noise within the AOM window (noise-1) and out of the window (noise), corresponding to two extinction ratios defined here as $\varepsilon_1 = 10\log_{10}\frac{P_{peak}}{P_{noise-1}}$ and $\varepsilon = 10\log_{10}\frac{P_{peak}}{P_{noise}}$.

Here, the calculated the extinction ratio and SNR of the pulses generated by the three setups (Figure 6.7, Figure 6.9, and Figure 6.14), and comparison is listed in Table 6.2. Here,

an relatively larger AOM window of 600 ns is used to show the noise difference within and outside the AOM, which will be optimised later. A pulse period of 76.8 μs has been maintained for all the measurements shown above.

Table 6.2 Key parameters of pulses generated from the three setups above (* calculated using extinction ratio of 50 dB).

Setup	Extinction ratio-1, dB	Extinction ratio, dB	SNR
EOM-AOM	21	50	75:1*
EOM-EDFA-AOM	20	50	62:1*
EOM- AOM-EDFA	20	25	1:1

The extinction ratio-1 is similar across all three setups, as expected from the EOM. However, the AOM significantly enhances the extinction ratio by 30 dB compared to configurations without using the AOM following the EDFA. This is confirmed later when it is used in OTDR system (Figure 6.24). These results demonstrate that the AOM substantially reduces noise levels and enhances the system's signal-to-noise ratio, which is particularly crucial when an EDFA is used for amplification. Therefore, in future experiments involving pulse amplification, the AOM is expected to be highly beneficial in mitigating the amplified noise introduced by EDFAs, a common approach that has already been demonstrated [124].

6.3 Building a highly sensitive OTDR system

In this part, the method of increasing the dynamic range is discussed so that the built OTDR system can be used for characterisation of HCFs.

As the backscattering signal is proportional to the power of the launched pulse, a pulse-amplification unit is designed to enhance the low-power commercial OTDR pulses before launching them into the fibre under test. The devices used, such as the AOM and EDFA, prevent the receiving of the backscattering signal directly. To address this, the backscattering signal is directed back to the OTDR's photodetector using two optical fibre circulators. The primary setup is shown in Figure 6.18.

Here, an EDFA (FA-15 from PriTel’s) is employed to amplify the OTDR pulses, followed by an AOM (from Gooch & Housego, rise time: 100 ns, model number: 26035-2-1.55-LTD-FO) to reduce the noise coming from the EDFA. The SMF is used as a pulse delay to make the synchronisation possible for the AOM window to the OTDR pulses via a Tap PD that receives 5% of the OTDR pulse, allowing the majority of light to propagate into the main path for pulse amplification.

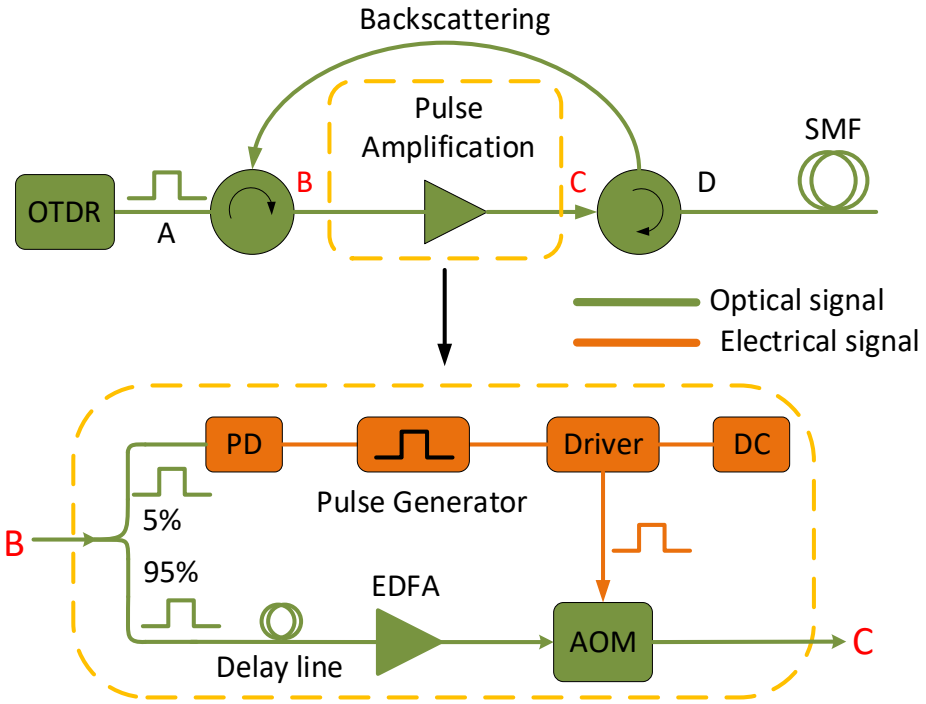

Figure 6.18 The proposed setup of amplifying OTDR pulses and guiding the signal back to OTDR detector (PD: photodetector, AOM: acousto-optic modulator).

As shown in Figure 6.19 (a), Tap PD uses an adjustable resistor (here, 500 kΩ) to adjust the gain of the detector in order to be able to trigger the pulse generator with the made PD shown in Figure 6.19 (b). As shown in Figure 6.20, the peak amplitude exceeds 2 V, more than enough to trigger the pulse generator despite the pulse width is far wider than the used 500 ns pulse here.

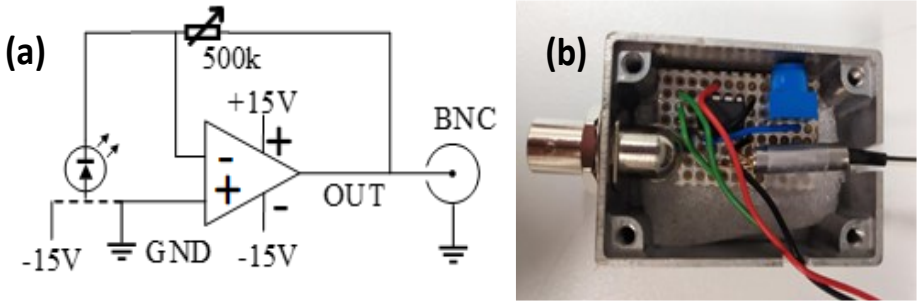

Figure 6.19 (a) The circuit and (b) the made Tap photodetector used in Figure 6.18.

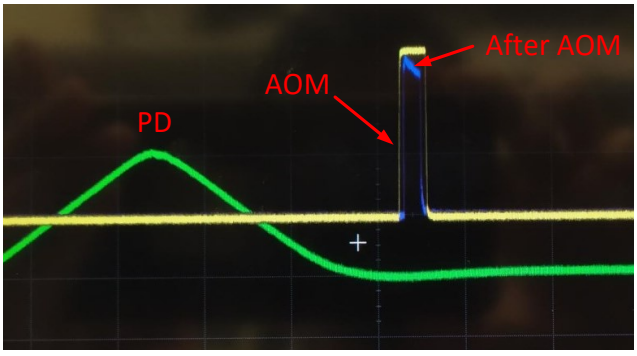

Figure 6.20 The observed synchronised pulses of output of the made Tap PD, RF pulse on AOM and output of AOM.

6.3.1 System based on a photo-counting OTDR

Here, two commercial OTDR instruments are available: one is the highly sensitive photo-counting OTDR (LOR-200 from Luciol Instruments) and the other is a low cost handheld OTDR instrument (FOTR-203 from fs.com). The performance of the photo-counting OTDR is shown in Figure 6.21. Since shorter pulses provide more detailed information about the fibre, and most current applications use relatively short lengths (kilometres or less), we focus on a 10 ns pulse, corresponding to a spatial resolution of 1 m in SMFs and 1.5 m in HCFs. As a highly sensitive OTDR, it has a dynamic range of almost 30 dB by using the photo-counting detector. It is worth mentioning that here, SMFs are used as the fibre under test to evaluate the OTDR performance due to their simple and easy connection with the OTDR system. Although 30 dB is close to detection of the predicted backscattering level in air-filled HCFs, we will show how it can be further improved.

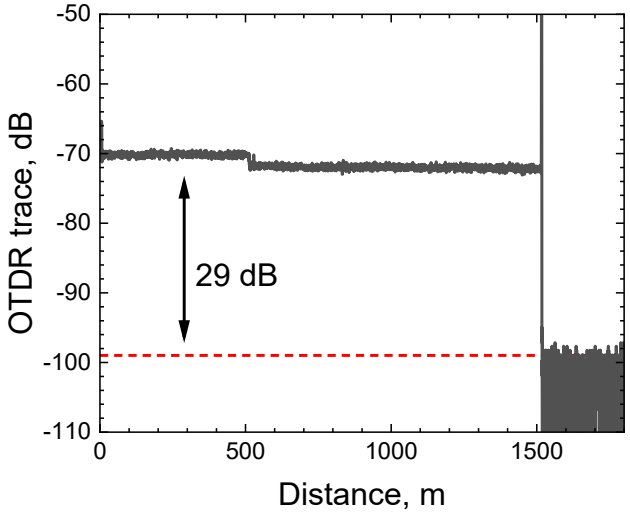

Figure 6.21 The trace of the photo-counting OTDR instrument (500 m SMF + 1 km SMF) is shown when the pulse is 10 ns.

When the pump current is increased, the amplified pulse power (launched pulse) is subsequently increased, as shown in Figure 6.22. For example, the pulse power is increased by two times at 29 mA (Figure 6.22), corresponding to the pulse in Figure 6.23 (a). Further amplified pulse's measurement requires attenuation to avoid saturating the detector, which will be shown later. This amplified pulse is then launched into the fibre under test with 3 dB higher backscattering signal. The noise floor of the amplified pulse is also shown in Figure 6.23 (b), which shows again the AOM's effect on reducing noise. Similarly, a large window is used, which will be optimised later to minimize the noise.

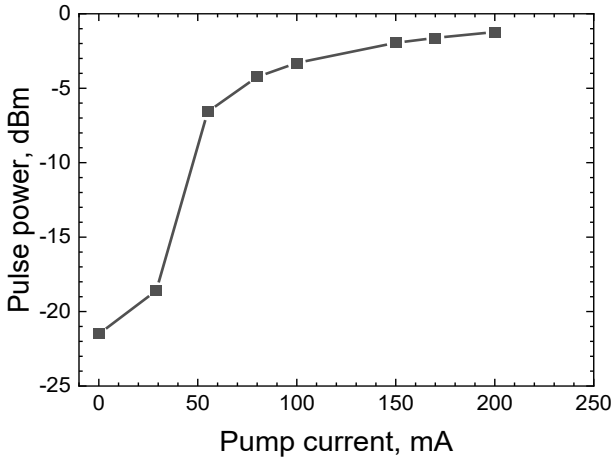

Figure 6.22 Increased power of the amplified pulse when EDFA works at different pump current.

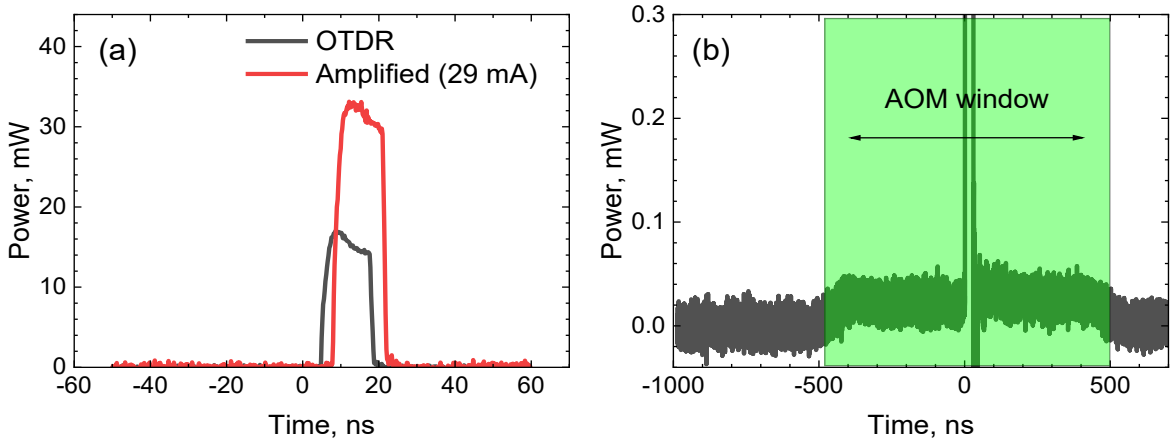

Figure 6.23 (a) 2× amplified pulse when EDFA works at 29 mA (further amplified pulses requires attenuator for detector measuring) and (b) the noise of the pulse with the AOM open window demonstrated.

The measured backscattering traces when the EDFA is pumped at different currents are shown in Figure 6.24. For the OTDR itself, the backscattering level is at the level of around -70 dB, while this can be increased to be 3 dB higher for 29 mA pump current (increased from black trace to red), corresponding to the amplified pulse in Figure 6.23 (a). By further increasing the pump current, the signal can be improved to be almost 20 dB higher for 200 mA pump current. Again, this backscattering level is in good agreement with the pulse power amplification shown in Figure 6.22, which demonstrates that the backscattering level from the fibre is proportional to the pulse power.

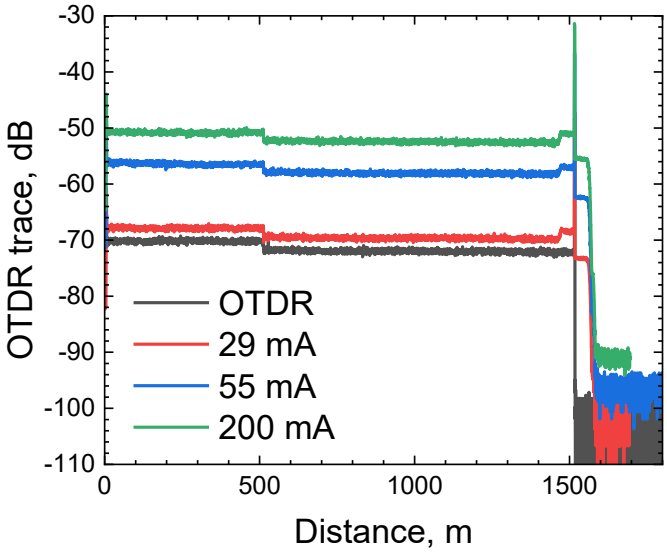

Figure 6.24 The OTDR traces of 500 m SMF + 1 km SMF when pulse-amplification is applied with the non-amplified OTDR showing for comparison.

However, the noise level also increases with the increased backscattering due to the EDFA induced noise (amplified spontaneous emission, ASE). This limits the improvement of dynamic range. For example, the backscattering can be improved up to almost 20 dB higher than the OTDR, but the noise level also get worse by about 10 dB, which leads to an improvement of dynamic range by only 10 dB when 200 mA is pumped for EDFA. The performance comparison is shown in Table 6.3. From the table, the backscattering level can be increased from 30.0 dB to 38.8 dB for the 55 mA pump current. This level can be further increased just slightly when increasing the pump current to 200 mA, which indicates that EDFA starts to generate more noise than the pulse amplification after 55 mA. This, on the one hand, shows launching stronger pulses can produce stronger backscattering, while, on the other hand, noise generated in pulse amplification system must be carefully managed.

Table 6.3 Performance comparison between the amplified OTDR and non-amplified.

Setup	Noise floor, dB	Backscattering level, dB	Dynamic range, dB
OTDR	-100.0	-70.0	30.0
29 mA	-98.2	-67.8	30.4
55 mA	-95.0	-56.2	38.8
200 mA	-90.2	-50.6	39.6

It is worth mentioning that a small ‘pedestal’ appears in the amplified OTDR traces at the end of the fibre (distance of 1500 m on the x-axis), which is caused by the large window (almost 1000 ns as seen in Figure 6.23 (b)) used for the AOM as the noise within it is not

reduced. This can be optimised by using shorter pulse for AOM operation, as seen in Figure 6.25. Compared to the 1000 ns window, the used 240 ns window can significantly reduce the “pedestal”, which can be further reduced by using a fast AOM. This pedestal noise demonstrates again that AOM is effective in improving the SNR of the amplified pulse.

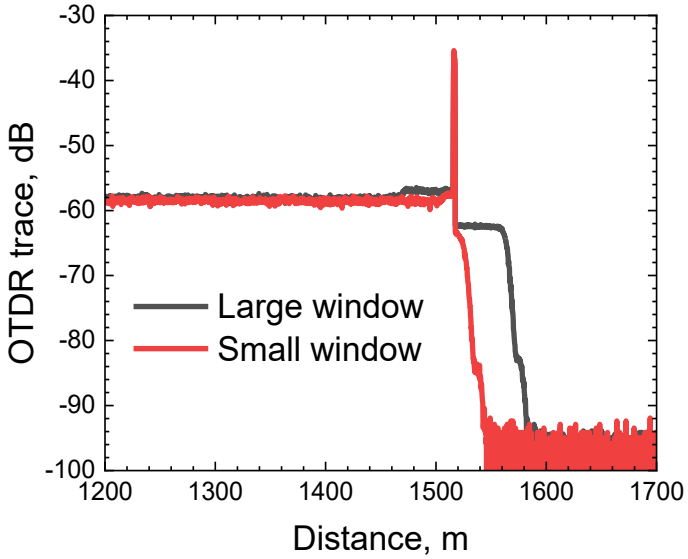

Figure 6.25 AOM window’s impact.

To further reduce the increased noise level for increasing the dynamic range of the system, we measure the optical spectrum of the OTDR pulse and the amplified pulse, as seen in Figure 6.26. The noise located at 1530 nm appears once the EDFA is used and the bigger is the gain, the worse is the noise. As the main noise is in different wavelength, a bandpass filter is expected to fill the main noise out. The setup is shown in Figure 6.27.

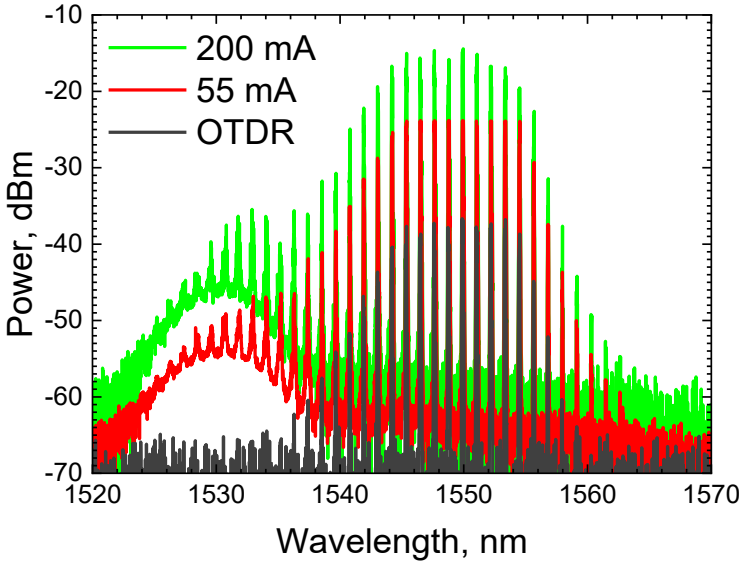

Figure 6.26 Optical spectrum of non-amplified and the amplified pulse.

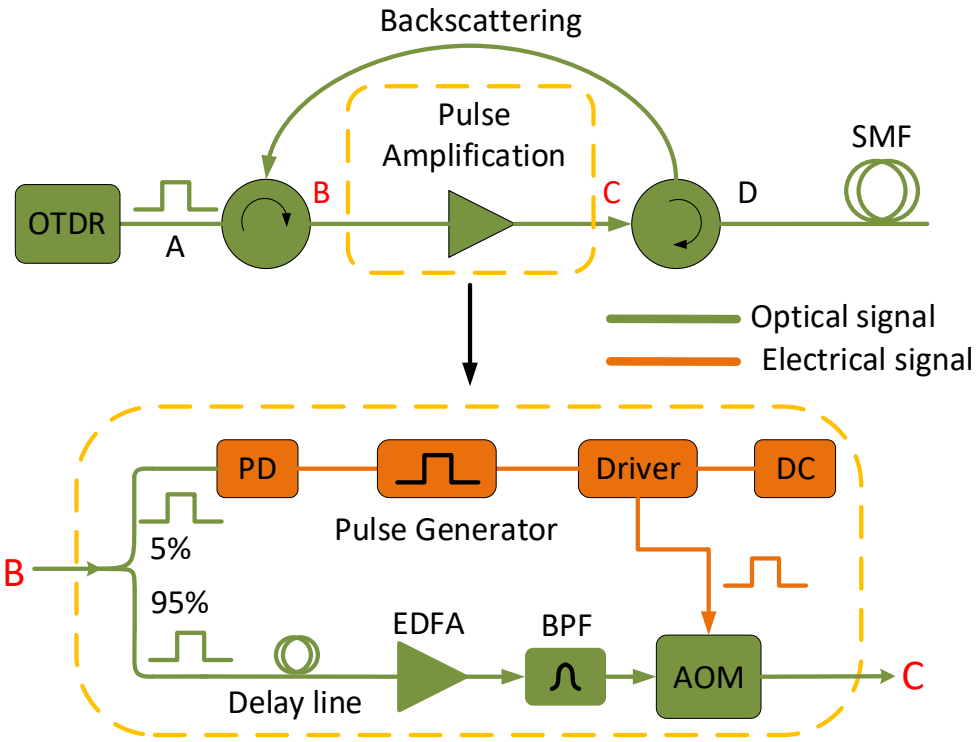

Figure 6.27 The proposed setup of amplifying OTDR pulses and guiding the signal back to OTDR detector with a bandpass filter applied (PD: photodetector, AOM: acousto-optic modulator, BPF: bandpass filter).

The filter's effect (passband: 1543 nm-1557 nm) is shown in Figure 6.28. As seen here, the noise around 1530 nm has been significantly reduced, which helps lower the noise floor of the OTDR traces, as shown in Figure 6.29. Although the filter introduces an insertion loss of about 1 dB, the noise level is reduced relatively more (nearly 4 dB), resulting in an increased dynamic range of about 3 dB. Despite this modest improvement, we keep the filter, as it also helps mitigate the ASE noise accumulation when another EDFA will be employed later. Here, the reflection peak at 500 m appears, which is due to the reconnection at the SMF-SMF connector.

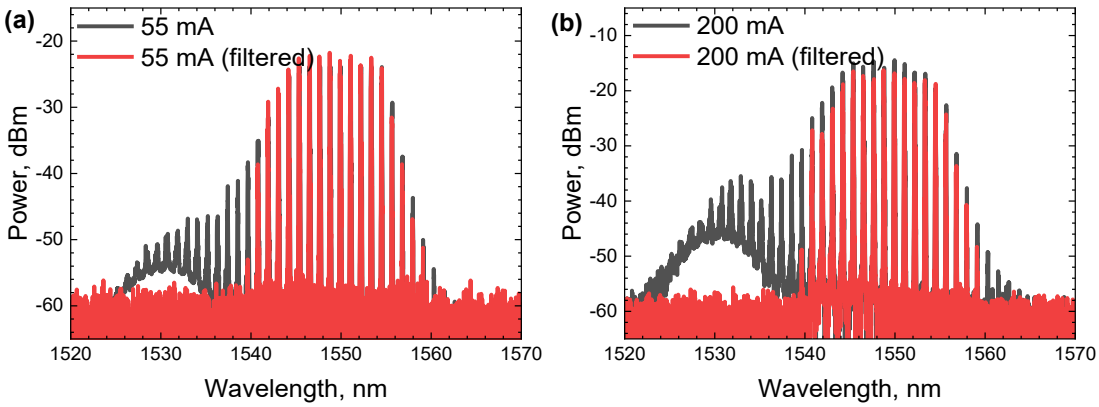

Figure 6.28 Optical spectrum of the amplified pulse and the filtered (a) 55 mA (b) 200 mA.

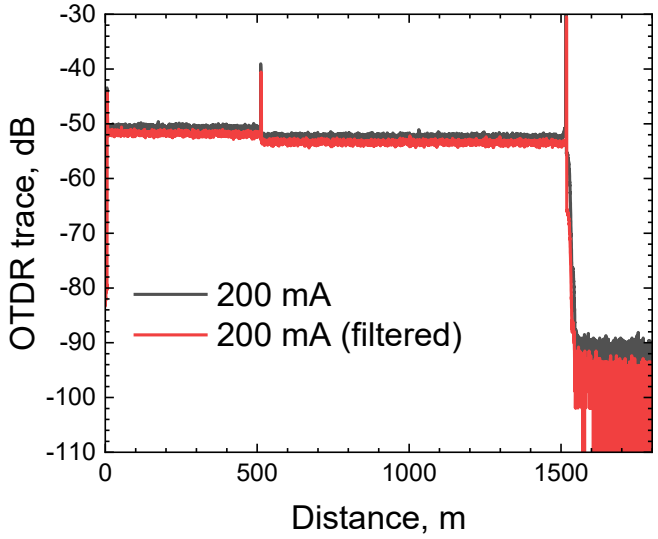

Figure 6.29 Bandpass filter's impact on noise floor of OTDR trace of 500 m SMF + 1 km SMF (here, peak at 500 m appears due to the reflection at the SMF-SMF connector).

Since the EDFA in Figure 6.27 amplifies more noise than signal at high pump current, a second EDFA (FA-18 from PriTel's) is required with the aim to further increase the pulse power, as seen the setup in Figure 6.30.

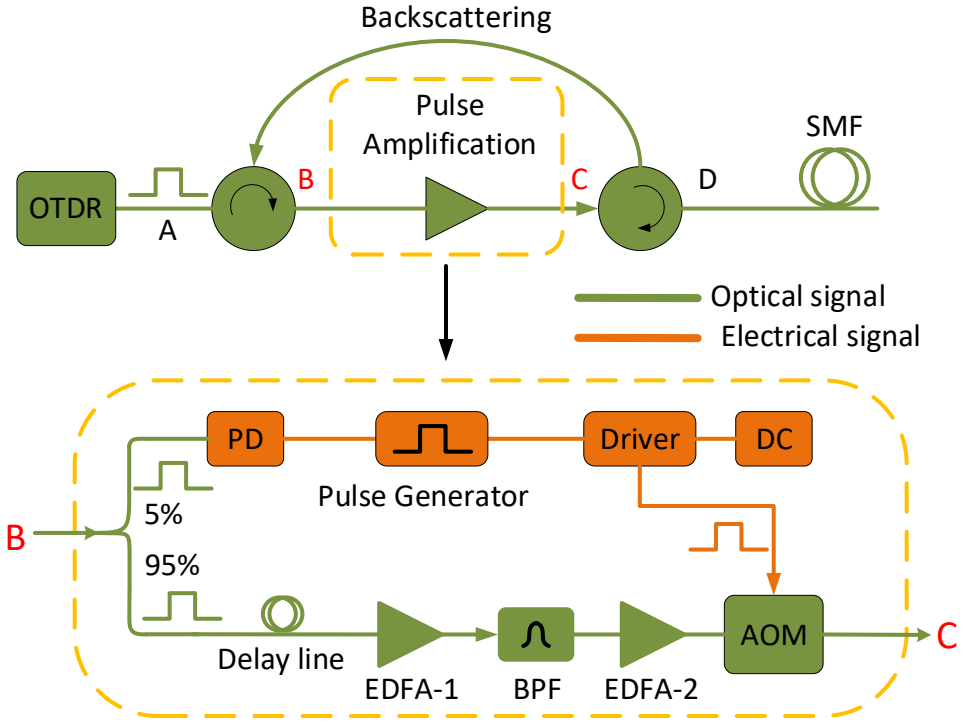

Figure 6.30 Setup based on two EDFAs.

As compared in Figure 6.31, the backscattering can be further improved by 10.5 dB, with a dynamic range improvement of 8.2 dB compared to the system when only one EDFA is used. The dynamic range of >45 dB is significantly higher than the OTDR itself, making it enough for measuring the backscattering in HCFs. Again, the reflection peak appears for the amplified OTDR traces compared to the OTDR trace measured when having a better SMF-SMF connection.

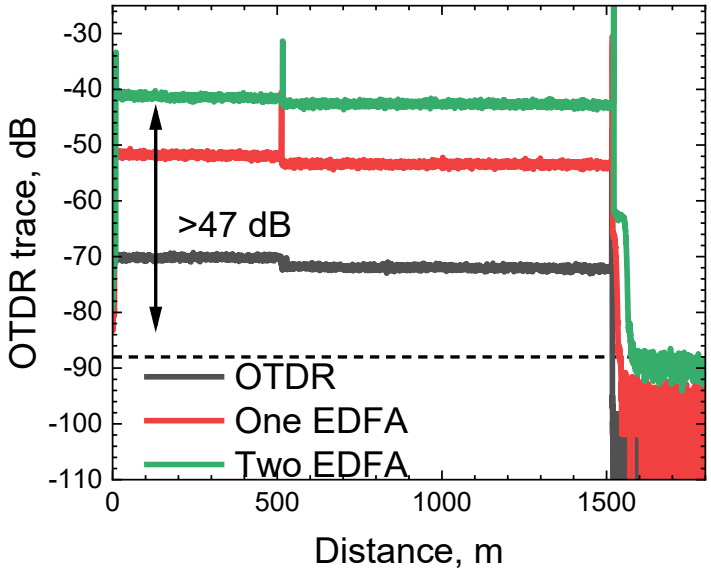

Figure 6.31 Comparison in the performance of OTDR traces of 500 m SMF+1 km SMF between OTDR, amplified OTDR (one EDFA) and amplified OTDR (two EDFAs).

As a summary, we have shown that a highly sensitive OTDR system can be achieved by applying a pulse-amplification unit that comprises two commercial EDFAs. Although the amplified noise level can be reduced when optical bandpass filter and the AOM are employed, the dynamic range of such a system can still be significantly improved.

6.3.2 System based on a standard OTDR

Since the used photo-counting OTDR records the data only one by one in length (e.g., 1.0 m, then 2.0 m…) for keeping a low noise level, the measurement can be very time-consuming, which is not friendly to the cases when fast measurement is required. For example, the as-drawn HCFs are always in low pressure that are subject to air ingress when they are operated for characterising, e.g., cutback, which has an impact on the performance, e.g., loss [45]. Therefore, fast measurement is preferred for HCFs characterisation. Here, we extend this strategy to a standard OTDR (FOTR-203, fs.com) that uses a standard photodetector and can conduct a measurement of the data of the whole length at the same time.

The optical spectrum of the used OTDR is shown in Figure 6.32. Since it is similar to the photo-counting OTDR, we expect the pulse-amplification unit can be applied to it. The same setup is in Figure 6.30.

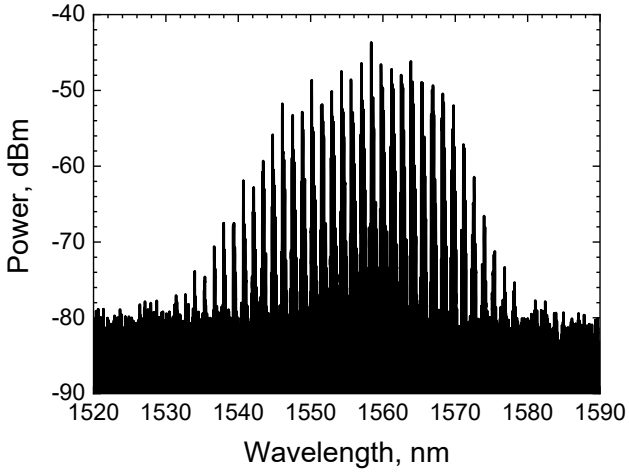

Figure 6.32 Optical spectrum of FOTR OTDR pulse.

The average power at the output of EDFA-1, output of filter, output of EDFA-2 and the launched power (after AOM) is shown in Figure 6.33. The input power for EDFA-2 is the power when EDFA-1 operates at 100 mA, which can increase the power from -5.9 dBm to more than 14.6 dBm at 200 mA and then reduced to 4 dBm due to the noise reduced by AOM. This leads to a 30 dB gain of the OTDR pulse power, corresponding to a 30 dB higher backscattering.

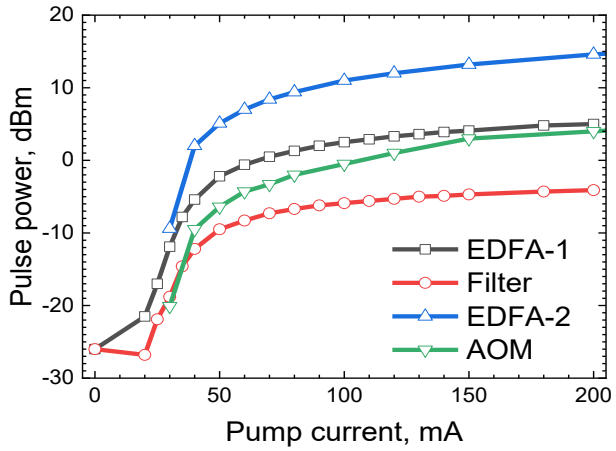

Figure 6.33 Pulse Power of the system in Figure 6.30 (the power of -26 dBm at 0 mA is the power from the OTDR).

The performance of the amplified FOTR OTDR system is shown in Figure 6.34. Here, 1-km SMF was used as the fibre under test. By applying one EDFA, the sensitivity can be increased by >12 dB and the second EDFA can further improve it by another 15 dB, contributing to a >28 dB higher sensitivity. Thanks to the employment of the filter and AOM, the noise floor remains relatively unchanged, which might also be due to the relatively higher noise tolerance compared to the ultralow photo-counting detection system. Consequently, the dynamic range is improved by more than 28 dB, consistent with the increased power. This improvement shall allow us to detect the backscattering from HCFs with a fast response. It is worth mentioning that the averaging time used here is just 15 seconds and

can be increased further, the noise floor could be reduced correspondingly. In later experiments, we will choose the averaging time accordingly.

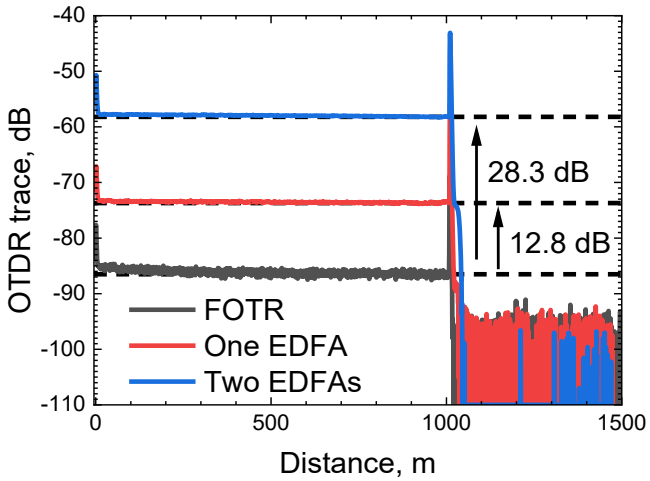

Figure 6.34 The OTDR traces of a 1 km SMF for FOTR based system.

6.4 Conclusion

The concept has been demonstrated of launching high-power pulses into the fibre under test to build a highly sensitive OTDR system. To prepare it, experiments was firstly conducted on optical pulse characterization and amplification, enabling the generation of high-power pulses. Subsequently, a method was proposed to enhance the dynamic range of commercial OTDRs, a concept demonstrated with both a photo-counting OTDR and a standard OTDR. This approach significantly increases sensitivity, with nearly 30 dB improvement observed for a standard OTDR. The built system is capable of characterising HCFs.

Chapter 7. Distributed characterisation of HCFs

In this chapter, we use the highly sensitive OTDR system that we have developed to characterise low loss HCFs (NANFs and DNANFs). Since the HCFs are easily filled with air, which generates relatively strong backscattering, atmospheric pressure distributed HCFs are tested firstly. Subsequently, air evacuation of HCFs is performed to study gas flow dynamics and explore surface roughness-related features. Finally, we extend our technique to apply a bi-directional OTDR measurement based method to HCFs, which makes it possible to extract the local attenuation and backscattering coefficient variation.

7.1 Air-filled HCFs

To measure the HCFs (a 885-m NANF, core size of 31 μm, end-face structure shown as inset in Figure 7.1 (a)), proper connection with SMF is required for light coupling. We, here, use free space coupling method, which is repeatable for measuring more samples at atmospheric pressure. This is based on an graded-index fibre (GRIN) fibre as a mode field adaptor, which is angled cleaved for reducing the strong Fresnel reflection at the silica-air interface and is directly spliced to SMF. The detail can be seen in Figure 7.1 (b), and the applied pulse-amplification unit again is shown in Figure 7.1 (a).

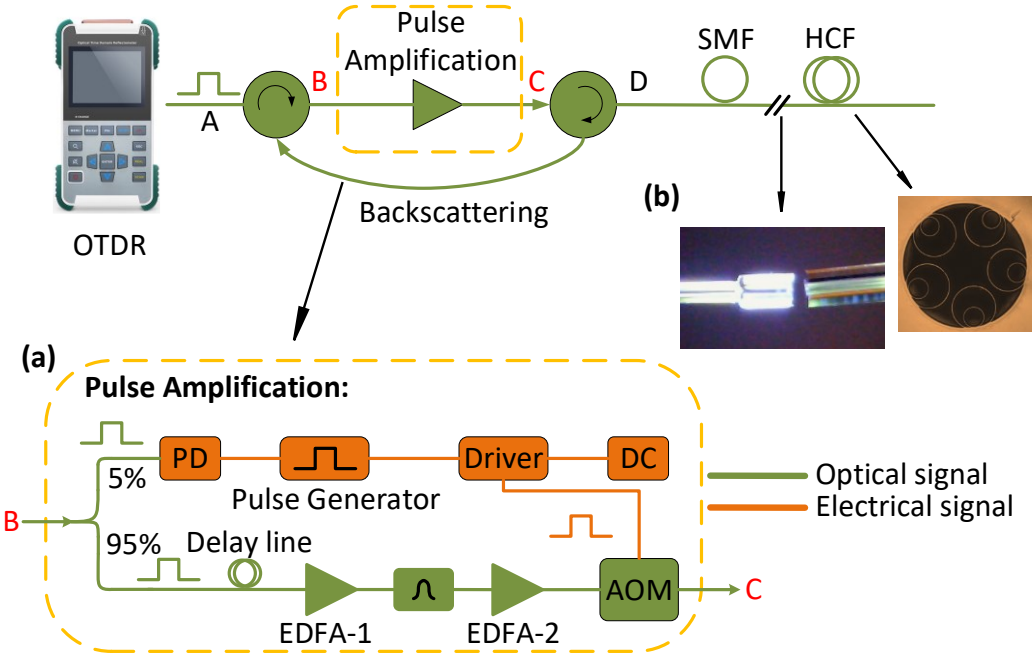

Figure 7.1 Experimental system showing the detail of the implemented Pulse Amplification unit (a) and detail of SMF-HCF light coupling (b). PD: photodetector, AOM: acousto-optic modulator.

The amplified pulse, shown in Figure 7.2 (a), is 28 dB higher than the non-amplified OTDR pulse. Notably, pulse distortion occurs, with the power on the falling edge being more than 50% lower than the power on the rising edge, which is a typical characteristic of EDFAs

[124, 125]. Although this level of distortion is reasonably acceptable for the experiment, the method for optimizing it is also discussed, which is shown in Appendix A.

The amplified pulse is expected to increase the sensitivity by 28 dB. The measured backscattering trace using the FOTR OTDR and amplified FOTR OTDR is shown in Figure 7.1 (b). Here, a 500 m SMF is used to show the backscattering difference between SMFs and the HCF. Without the Pulse Amplification unit, the FOTR-203 shows a dynamic range of only 14.4 dB for SMFs, which is insufficient for using with HCF which is expected to have an almost 30 dB lower backscattering level. Using the Pulse Amplification unit, the power was boosted by 28 dB, whereas the detection noise level stayed unchanged thanks to the use of the optical bandpass filter and the AOM in the Pulse Amplification unit. This results in a significantly higher overall dynamic range of 14.4 + 28 = 42.4 dB for 10 ns pulses that can “see” the backscattering in HCF, which is 15 dB higher than the noise floor.

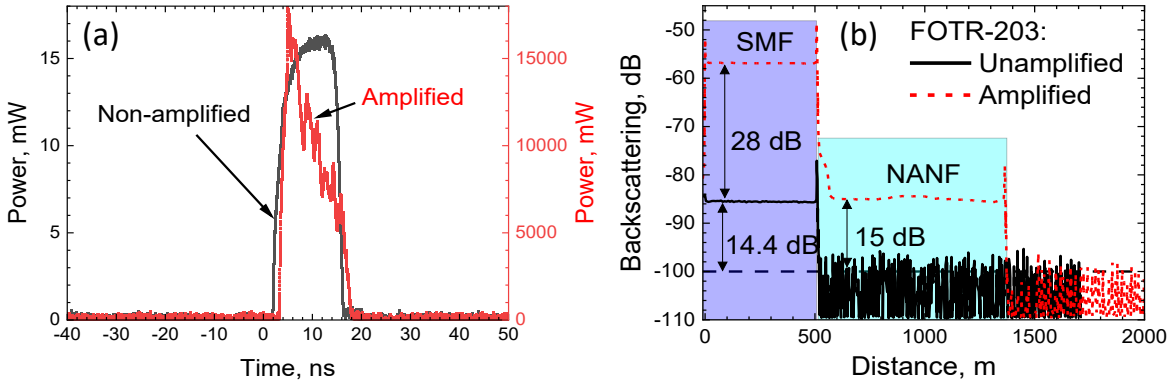

Figure 7.2 (a) The amplified pulse with the non-amplified shown for comparison (b) The measured backscattering using 10 ns pulses of the 509-m SMF and 885-m NANF with the FOTR-203 both without and with the Pulse Amplification unit.

To make it comparable, the backscattering is also converted into backscattering coefficient.

The length-normalized backscattering coefficient *B* (dB/m) is obtained as:

$$B = P_b - 10\log(0.5 \cdot Pw \cdot v_g) + 15.0\ dB, \quad 7\text{-}1$$

where P_b is the relative power of the backscattered signal when the pulse width is Pw (10 ns here), the middle term represents the normalization to 1 m in fibres, and 15.0 dB is the calibration constant for the Pulse Amplified FOTR-203 setup, which we calculated from the SMF backscattering by considering a SMF backscattering coefficient of -72 dB/m [104].

After compensating the round-trip loss introduced by the connector (2 × 0.2 dB FC/APC connector between the OTDR SMF pigtail and 500-m SMF) and the coupling at SMF-HCF (2 × 0.9 dB), we obtained:

$$B_{SMF} = P_b - 10\log(0.5 \cdot Pw \cdot v_g) + 15.0\ dB + 0.4\ dB, \quad 7\text{-}2$$

$$B_{HCF} = P_b - 10\log(0.5 \cdot Pw \cdot v_g) + 15.0\ dB + 2.2\ dB \quad (7\text{-}3)$$

As shown in Figure 7.3, the NANF backscattering coefficient is close to -99 dB/m, which is 27 dB lower than that of the SMF, which agrees well with that as predicted in [46]. We also use the LOR-200 OTDR (using photon counting detection) to conduct the same measurement and the comparison is shown in Figure 7.3. Both instruments (FOTR-203 with Pulse Amplification unit and LOR-200) give almost identical backscattering coefficients. They also show comparable dynamic range. For FOTR-203, this was achieved thanks to our Pulse Amplification unit that boosted the pulse power without degrading the noise level.

The FOTR-203 with Pulse Amplification unit enabled us to measure with 10 ns pulses with 30 seconds averaging time, which is significantly faster than with LOR-200 photon-counting, which without any Pulse Amplification unit required almost 1 hour to perform the same measurement with similar noise performance. This is an important advantage for charactering HCFs when the time of opening to air needs to be as short as possible to avoid contamination or gas ingress. The comparison in the performance of these two techniques is shown in Table 7.1. It is worth mentioning that our LOR-200 is upgraded from the instrument used earlier with a reduced noise level.

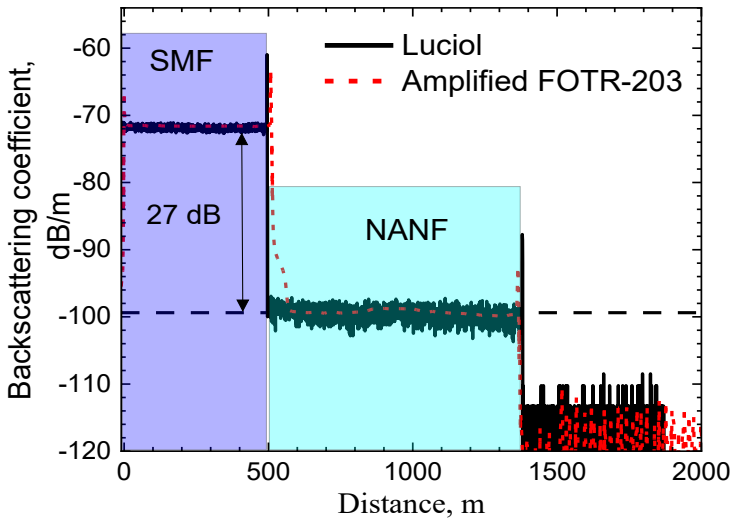

Figure 7.3 Backscattering coefficients obtained from measurements with the Pulse Amplified FOTR-203 and with a high sensitivity LOR-200 OTDR without Amplification unit.

Table 7.1 Performance comparison of Amplified FOTR-203 and photon counting LOR-200 OTDR.

	Low-cost OTDR (amplified)	Photon-counting OTDR
Pulse-width	10 ns	10 ns
Acquiring time	30 seconds	~ 1 hour
Backscattering variation	<±0.2 dB	±2 dB

A DNANF fibre (length: 1.6 km, core size: 28 μm) with some defects has been measured using this system, as shown in Figure 7.4. From the traces, some features can be observed,

e.g., the peaks (the local strong reflection) at 1602 m and 1975 m. Although the exactly factors related to these features are not clear and requires further investigation (e.g., using other techniques [18]), one of the several possibilities is the change in local microstructure (e.g., roughness). The measured spatial resolution at the full width at half maximum (FWHM) is shown in Figure 7.4 (b), which is < 2 m, as expected from the pulse width.

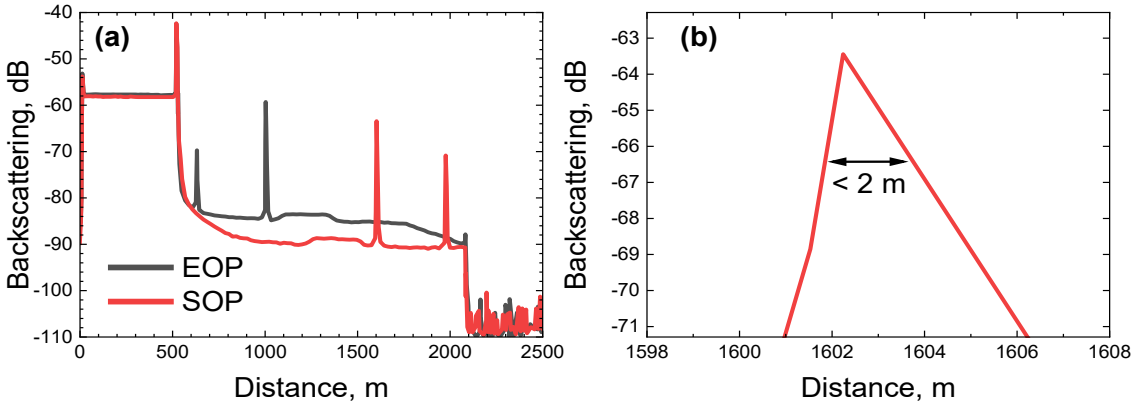

Figure 7.4 (a) The measured backscattering of a DNANF (b) The spatial resolution measured at the full width at half maximum (FWHM).

7.2 Evacuation of HCFs

In many applications, controlling the composition of the gas in the HCF core or even eliminating it through evacuation may be necessary. This may be required to avoid water vapor absorption (prominent at wavelengths around 1.3 μm), CO_2 (absorption at ~2 μm) or to decrease the already-low nonlinearity when using very high peak powers [8].

Evacuation of HCFs is typically not monitored due to the lack of practical techniques, and the required evacuation time is often estimated using theoretical models. These models usually consider circular-shape cores, while low-loss HCFs such as NANFs/DNANFs have cores with significantly more complex shapes. For HCFs longer than 100 m, the evacuation process can take weeks; real-time monitoring could save considerable amounts of time and help identify potential leaks during the process.

It is expected that the backscattering in air-filled HCFs is proportional to the air pressure, so the evacuation can be monitored by measuring its backscattering. As demonstrated earlier in measuring air-filled HCFs, the backscattering at atmospheric pressure is >10 dB higher than the noise floor, which indicates that this system will allow us to monitor the pressure of down to at least 0.1 atm.

Here, the HCF evacuation is experimentally monitored using the developed system. This requires not only sensitive instrumentation but also the good management of the launch back-reflection that usually limits the measurement sensitivity. Extending this technique to monitor HCF evacuation requires measuring of even weaker signals (10 dB weaker when

targeting 0.1 atm internal air pressure) and hermetically sealing the optical input end of the HCF while maintaining low loss and a low level of back-reflection.

7.2.1 Evacuation of a NANF (gas flow)

7.2.1.1 SMF-HCF connection

For the SMF-HCF connection, there are mainly two challenges that must be addressed [126]. Firstly, there is a mismatch in the mode field diameter between the fundamental mode of a low-loss HCF and the fundamental mode of SMF (e.g. ~24 μm for NANFs vs ~10 μm for SMF), which can cause loss as large as ~3 dB. A mode-field adapter (MFA) between the HCF and SMF is required, which is a short piece of a GRIN fibre. Secondly, it is essential to control the strong back-reflection (Fresnel reflection) at the air-silica interface that can easily damage the detector used in OTDR or cause significant dead zone.

To address this, a short piece of a graded-index fibre is spliced to SMF with the other end angled-cleaved for reducing the back-reflection, which is angled spliced to the HCF, as shown in Figure 7.5. The detailed discussion is in [91].

Figure 7.5 Illustration of the SMF-HCF connection for low loss and low back-reflection.

7.2.1.2 Experiment

(1) 55 m NANF

Since the evacuation in HCFs is a very slow process, which usually takes weeks for hundreds meters HCF, a short length of HCF is firstly used in our experiment. Here, the 55 m HCF with a core diameter of 33.4 μm is spliced to the SMF, as the same in Figure 7.5. The achieved connection here has an insertion loss of about 1.5 dB with a back-reflection of below -55 dB (15 dB better than the spliced connection of the same geometry published in [91]).

As shown in Figure 7.6, OTDR is directly connected to SMF pigtail via FC/APC connector and the distal end of HCF is mounted into a vacuum chamber. The used pulse gives a spatial resolution of <2 m, which is more than sufficient for the 55 m long HCF used here.

Before the experiment, the HCF had been kept open to air long enough (weeks) to achieve equilibrium pressure of 1 atm and this is confirmed with the measured backscattering distribution of the HCF as shown in Figure 7.7 (0 min). The backscattering signal monitored

over 2 days of evacuation is shown in Figure 7.7. The pressure inside the vacuum chamber has been kept below 0.01 atm (measurement range limited by the pressure gauge).

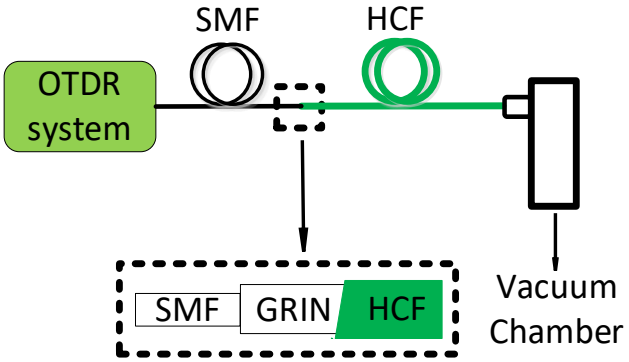

Figure 7.6 The diagram of the experimental setup for HCF evacuation and monitoring.

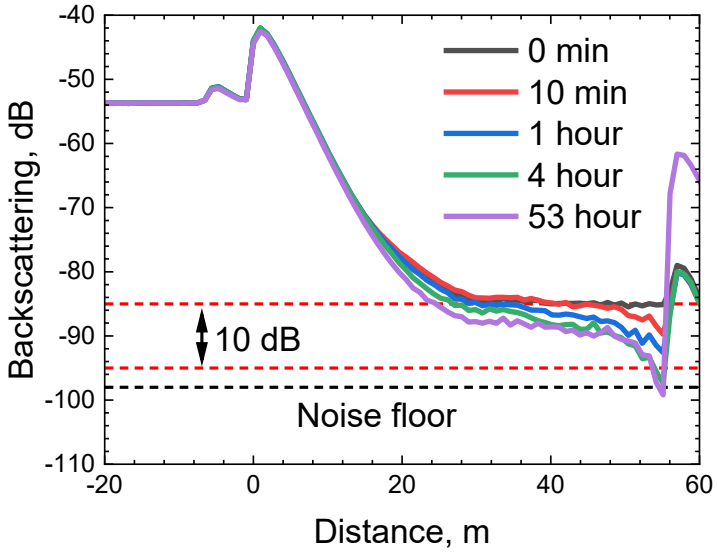

Figure 7.7 Backscattering distribution during evacuation.

As air escapes from the hollow core due to the pressure gradient-driven force, the backscattering decreases from the distal end. It is worth mentioning that the end facet reflection increased at 55 m after 53 hours, possibly due to contamination. This issue is not a problem as it only can introduce a dead zone beyond that point. Although more than 10 dB lower backscattering (10 times less pressure) is monitored after 4 hours, the whole backscattering seems keep unchanged after 4 dB decreasing, which is very likely limited by the dead zone of used low-cost OTDR, as seen the slope from 0 m to 20 m and even longer (as seen from the decreasing trend of the trace after 53 hour). To have more useful data, length extension will be required.

(2) 167 m NANF

To obtain the desired length beyond the OTDR dead zone, a 112 m NANF (from the same spool as 55 m NANF) is directly spliced to the 55 m NANF with a 0.5 dB loss. To repeat the experiment, we record the data, as shown in Figure 7.8. The backscattering decreases after evacuation starts, which, however, stopped changing from 4 days to 10 days. This strongly

suggests the connection is leaking and air from the environment is filling. Therefore, we further seal all the connectors (both SMF-HCF and HCF-HCF) with glue, and the results are shown in Figure 7.9.

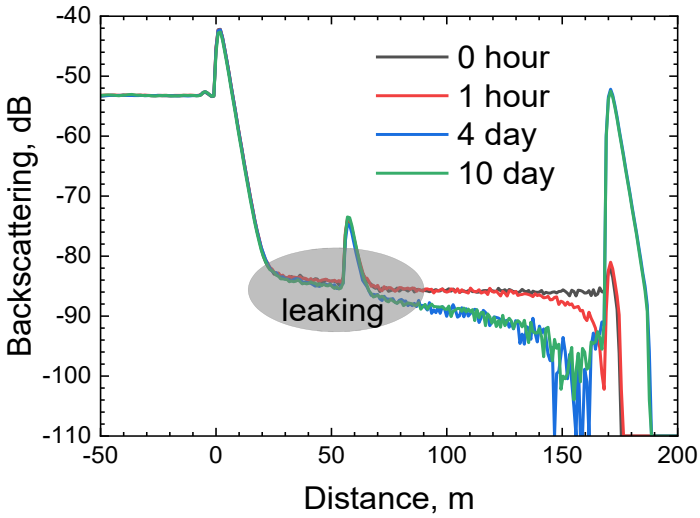

Figure 7.8 Monitoring of the 55 m +112 m HCF.

The backscattering signal monitored over 15 days of evacuation is shown in Figure 7.9. As we observed earlier, backscattering decreases at the distal end and gradually the whole length. The backscattering signal from the distal end of the HCF reaches the measurement noise floor (12 dB reduction in the backscattering signal) in about 1 day. This noise floor allows us to monitor the pressure change down to 0.07 atm. Although the measured data is still affected by the dead zone, the level of 0.07 atm could be reached beyond the dead zone of about 70 m.

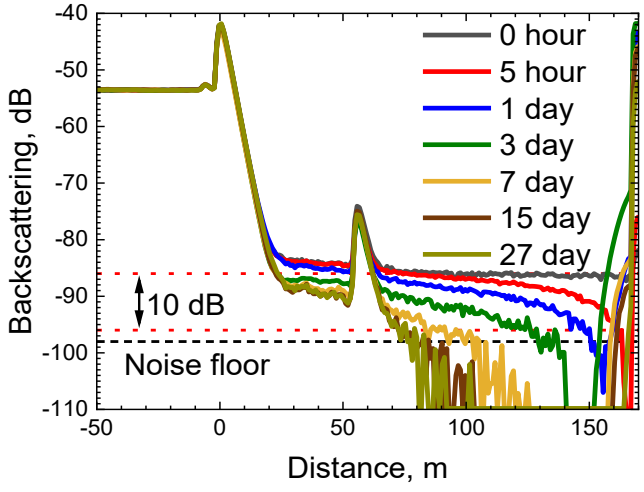

Figure 7.9 Monitoring of the 55 m +112 m HCF after sealing the connection using glue.

7.2.1.3 Gas flow dynamic

For a homogeneous gas, it is described by different models, which is determined by the Knudsen number. As shown in Figure 7.10, gas flow generally has three regimes [127].

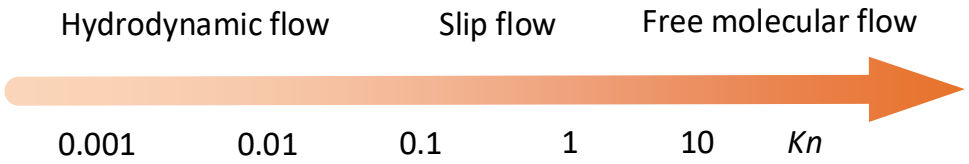

Figure 7.10 Knudsen number based gas flow regimes.

The definition of Knudsen number K_n:

$$K_n = \frac{\sigma}{d}, \tag{7-4}$$

where σ is the mean free path, which is the average distance that a particle can travel between two successive collisions with other particles or between intermolecular collisions, and d is the core size of the HCF.

For collisions of identical particles, the mean free path can be defined as:

$$\sigma = \frac{kT}{\sqrt{2}\pi p d_m^2}, \tag{7-5}$$

Here, T is the temperature, k is the Boltzmann constant, p is the pressure, and d_m is the molecule diameter. Therefore, we have:

$$K_n = \frac{kT}{d\sqrt{2}\pi p d_m^2}, \tag{7-6}$$

When we consider the gas to be nitrogen with a diameter of 364 pm and temperature is 25°C, the calculated Knudsen number with pressure is shown in Figure 7.11. For low vacuum condition (e.g., ~0.1 atm), the gas flow can be treated as in the hydrodynamic flow regime and slip flow regime may be approached. To simplify our analysis, we only consider the gas flow to be hydrodynamic flow, which is a reasonable assumption due to the pretty low vacuum condition (>0.01 atm) in our experiment.

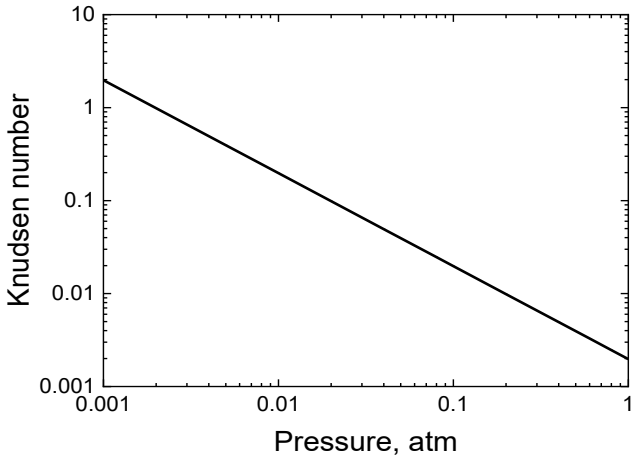

Figure 7.11 Knudsen number as a function of pressure (gas: nitrogen; temperature: 25 °C)

For hydrodynamic flow, the gas flow dynamics in a HCF can be solved using the analysis in [128], which considers a circularly shaped core:

$$\frac{\partial \rho}{\partial t} = \frac{d^2}{32\eta}\frac{\partial}{\partial x}\left(p\frac{\partial p}{\partial x}\right), \tag{7-7}$$

p is the pressure; *t* is time; η is the dynamic viscosity, which in Kinetic theory is independent of pressure; *x* is the HCF distance; *d* is the core size.

In the dimensionless form, it is:

$$\frac{\partial k}{\partial th} = \frac{\partial}{\partial \xi}\left(k\frac{\partial k}{\partial \xi}\right), \tag{7-8}$$

where k is the normalized pressure $k = p/p_0$; ξ is the normalized distance $\xi = x/L$ (*L*, fibre length); t_h is the dimensionless time, which can be converted to the real time *t* by:

$$t = \frac{32\eta L^2}{d^2 p_0} t_h = K_h \cdot t_h. \tag{7-9}$$

The Eq. 7-8 can be solved numerically and the result for HCF evacuation is shown in Figure 7.12. The air escapes dramatically slower than the filling, which indicates the HCFs evacuation is time-consuming.

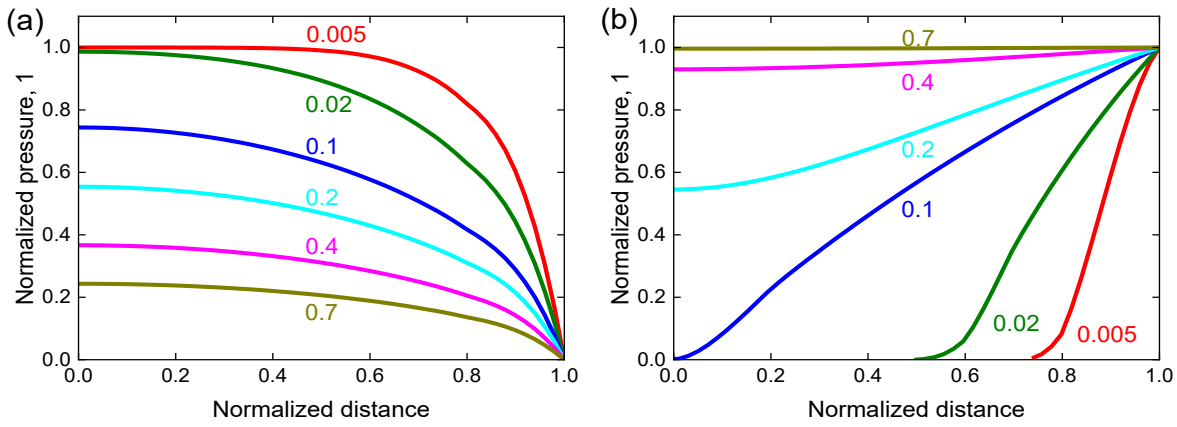

Figure 7.12 The calculated distributed normalized pressure as a function of dimensionless time of (a) air-evacuation and (b) air-filling.

7.2.1.4 Comparison between experiment and theory

To make it comparable, we firstly convert the measured backscattering traces (Figure 7.9) into pressure distribution, which is based on the assumption that the backscattering in air-filled HCFs is approximately proportional to the air pressure. As shown in Figure 7.13, the pressure decreases during evacuation and the minimum pressure we measured is below 0.1 atm (0.07 atm) after 15 days evacuation.

When a circular core is considered in the model using Eq. 7-8, as shown in Figure 7.14, the predicted pressure during evacuation can be calculated using the HCF's core as the circular core. As shown in Figure 7.13, there is a big discrepancy between experiment and theory, which shows that air flow in HCF (NANF) is slower than that suggested by the theory.

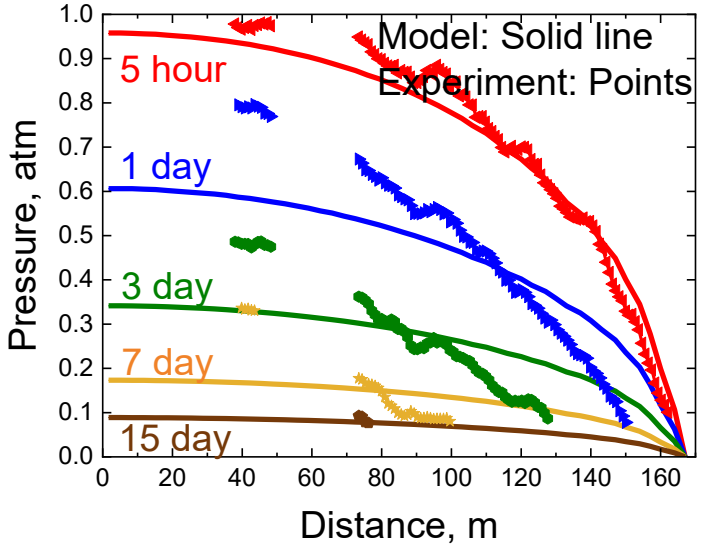

Figure 7.13 The comparison of pressure distribution between the measured results and the model in [128].

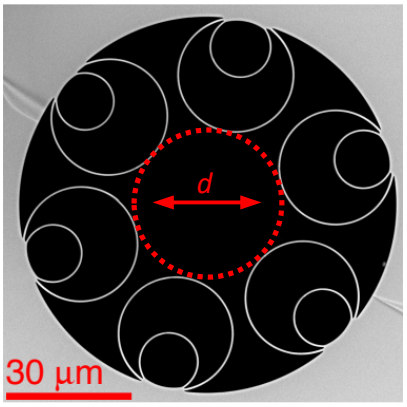

Figure 7.14 The considered core size in model.

The slower gas flow is believed to be caused by the air inside those small gaps of the cladding capillaries. For achieving a better prediction, a scaling factor of about 70% was suggested in a recently published paper [129]. The results is shown in Figure 7.15 when we consider the core size to be 70%, which shows significantly better agreement. The measured pressure gradient along the HCF length is not very well matched with the predicted result, which might be due to the splicing between 55-m NANF and 112-m NANF that slowed down the gas flow. However, the average pressure gives a reasonable agreement, enabling us to estimate the time necessary for evacuation of an HCF of NANF. For example, it can take about two weeks to evacuate the 167 m HCF to achieve an average pressure close to 0.1 atm.

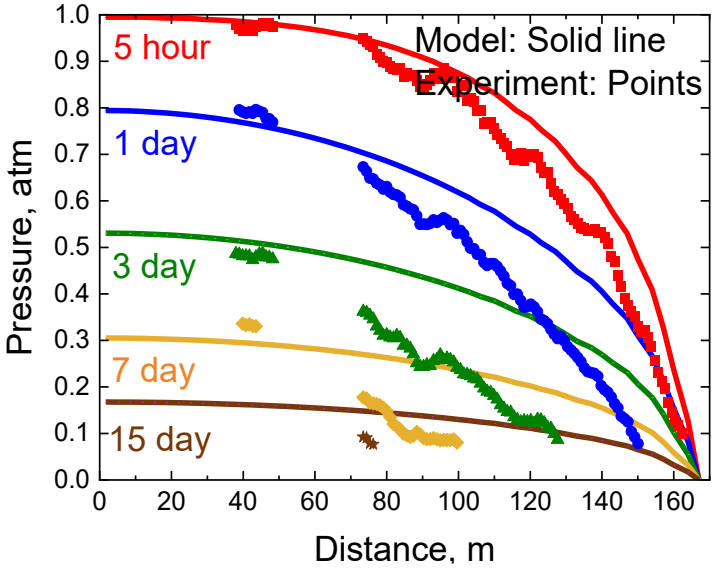

Figure 7.15 The comparison of pressure distribution between the measured results and the model in [128] when the core size is considered to be 70%, as suggested in [129].

7.2.1.5 Gas-refilling

After the evacuation, the air-filling process has also been monitored when the HCF end was open to the environment. The monitored backscattering change is shown in Figure 7.16. The air ingress is significantly fast than the evacuation, and reaches close to atmosphere pressure everywhere within just 3 days.

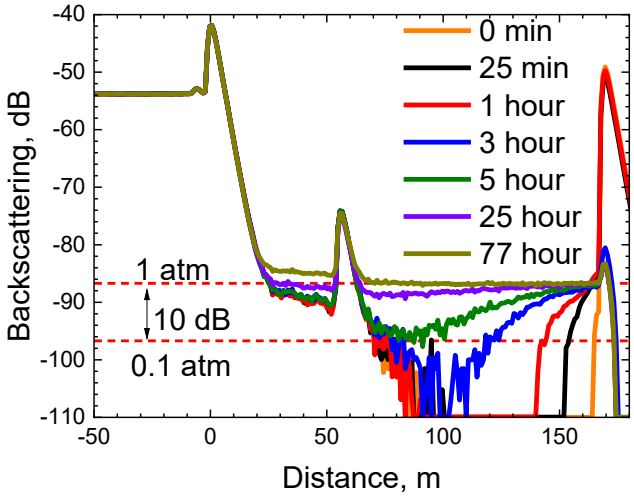

Figure 7.16 Monitoring of the HCF filling.

The calculated pressure change is shown, and compared with the theory, in Figure 7.17 when the core size is considered to be 70% of the NANF core size. This can be an importance guidance for HCFs operation. For example, the air of 0.1 atm can penetrate 20 m within one hour after opening to environment. This allows researchers to evaluate the pressure inside the sealed HCF, which is practically very important in preparing low pressure HCF samples for applications such as gyroscopes [14].

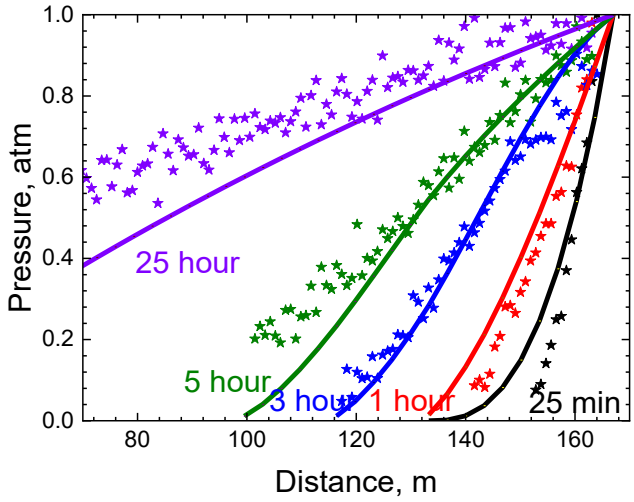

Figure 7.17 Pressure change during HCF filling (solid line: model; star: experiment).

7.2.2 Evacuation of a DNANF (surface scattering)

To further study the gas flow, and meanwhile aim to see the static surface structures of the HCFs for fundamental characterisation (our main interest), a DNANF (core diameter: 26.5 μm) is used for evacuation. Since the core size is smaller than the NANF used earlier (26.5 μm vs 33.4 μm), the expected surface scattering is higher (>5 dB) than the NANF used above. Furthermore, the SMF-HCF connection is optimised with backscattering of about -70 dB (>10 dB reduced, reducing the impact of dead zone) and insertion loss is also reduced to just half a dB, which results in a 2 dB higher dynamic range as it is roundtrip (0.5 dB vs 1.5 dB).

The experimental setup is shown in Figure 7.18 (a). The HCF is connected with the SMF via GRIN, which is glued together based on a modified fibre-array technology to maintain the low back-reflection and low insertion loss [130, 131]. The distal end of the HCF is mounted into the vacuum chamber, which is monitored by a pressure meter. Once we start the pump for the chamber, the OTDR measurement is recorded periodically until the air inside HCF is negligible.

As predicted in [46], the surface scattering is 8 dB lower than that at atmospheric pressure. This suggests the surface scattering becomes dominant after the pressure is reduced to 0.16 atm (a predicted value).

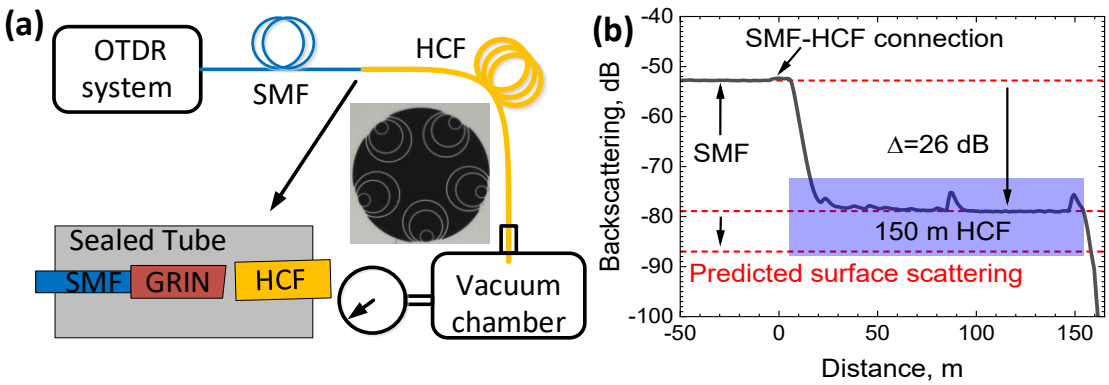

Figure 7.18 (a) Experimental setup, with the insets showing the SMF-HCF connection and the cross-section of the used HCF sample (b) the measured backscattering trace of the SMF+HCF (at atmospheric pressure).

Figure 7.18 (b) shows the backscattering distribution when the HCF is still at atmospheric pressure. The backscattering level of the air-filled HCF is at -79 dB, which is almost 7 dB higher than that in Figure 7.9 (stronger backscattering + lower connection loss). Since the noise floor is another > 15 dB lower, this shall allow us to see the surface scattering (at the level of -87 dB) as predicted.

The recorded backscattering traces during evacuation of up to 49 days are shown in Figure 7.19. As expected as the air pressure inside the HCF reduces, the backscattering signal

from the air inside the HCF reduces. As the gas pressure continues to reduce, further surface-related features become clear and this is successfully measured by OTDR for the first time.

The measured surface scattering clearly shows the features that are directly related to the glass surface, which are usually obscured in HCFs with an atmospheric pressure air-filled core. The position of these features along the fibre length remain fixed as the gas pressure reduces further, as would be expected from (static) surface scattering. For example, the features between 132 and 138 m only start appearing after 15 days when the pressure is below 0.1 atm (a measured value) (note, internal gas pressure estimated based on that the backscattering is proportional to pressure). Although the factors related to these features are still unclear, they are likely caused by localized increases in surface roughness around the core. After 49 days, all the fibre shows backscattering features from the microstructure surface. The surface scattering is surprisingly about 7 dB lower than that as predicted, which suggests the model in [46] needs to be modified.

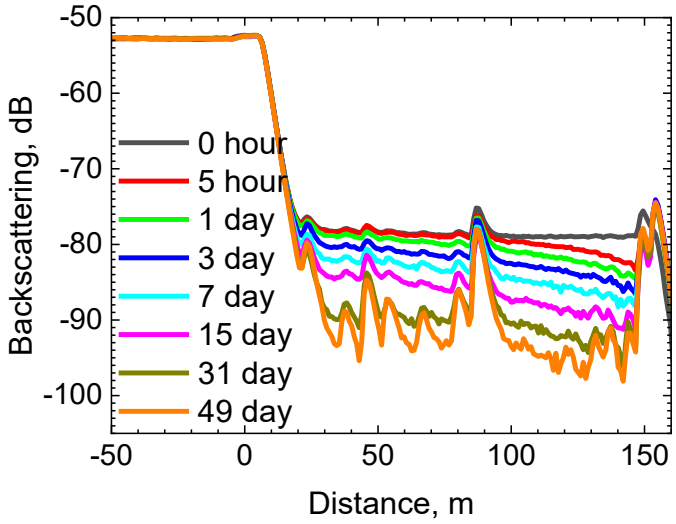

Figure 7.19 Monitoring of the 150 m HCF of up to 49 days.

To simplify the analysis, the contribution from surface roughness is considered negligible. The backscattering traces are then converted to pressure, assuming that the backscattering intensity is proportional to the air pressure. As shown in Figure 7.20, the pressure has been reduced to below 0.1 atm (about 0.05 atm) at 49 days. The comparison with the theory when 70% core size is considered gives a good agreement, especially at high pressure (close to 1 atm). At low pressures it seems less accurate, where evacuation expected after 100 days is reached already in 49 days. This might be because the gas flow is going through the slip flow region where the model used here no longer applies, which suggests a novel model might be required for high vacuum HCFs characterisation and applications.

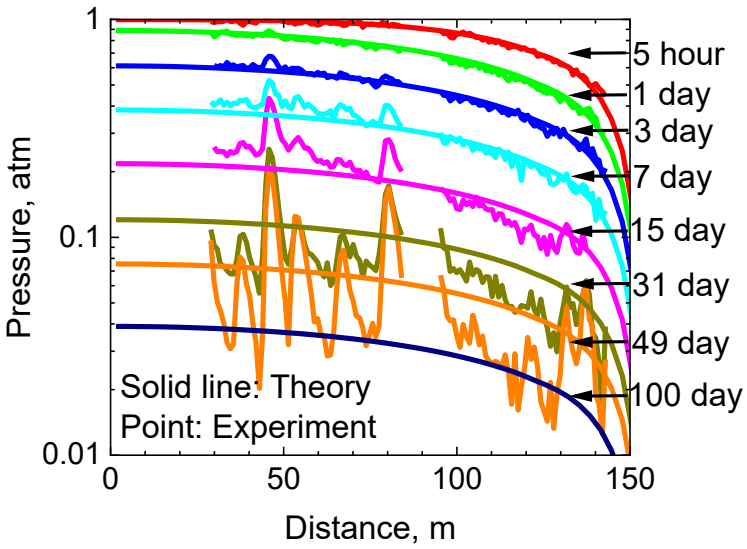

Figure 7.20 The comparison of pressure distribution between the measured results and the model in [128] when consider the core size to be 70%, as suggested in [129].

7.3 End facet contamination

During our experiments, we noticed the reflection at the end facet increases with time and we monitored this. The setup is shown in Figure 7.21, where the distal end of the HCF is flat cleaved.

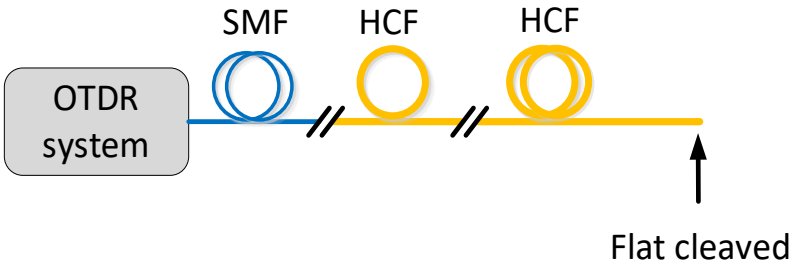

Figure 7.21 Experimental setup of monitoring the end facet contamination.

As shown in Figure 7.22, there is no observed reflection at the moment when the HCF was just cleaved (below the level of HCF backscattering). As time goes on, the reflection increases by 1.5 dB at 1 day and >10 dB after 4 days. We believe this is caused by the end facet contamination (the optical microscope image of the contamination growth is shown in Figure 7.23), which was investigated in [132]. The contaminant originates from the growth of ammonium chloride (NH_4Cl) which is likely from the glass itself and can be restored by measures such as heating.

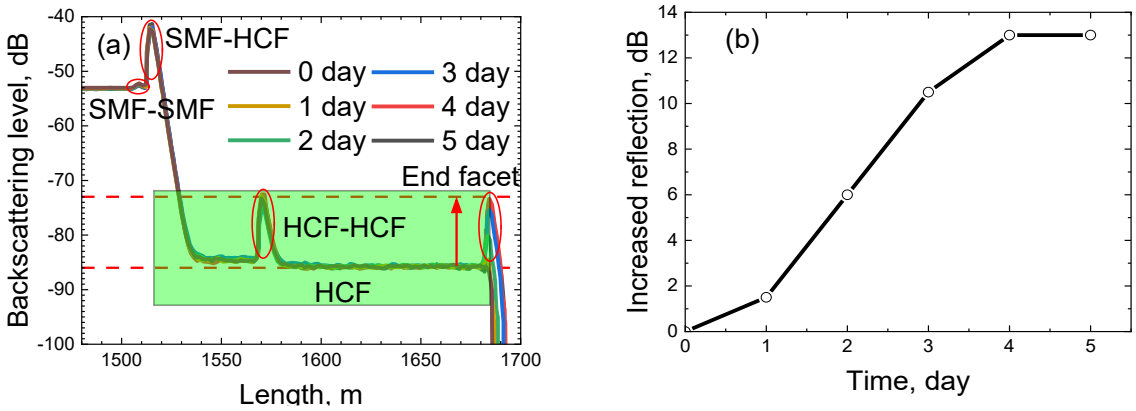

Figure 7.22 The monitored end facet reflection of the HCF (a) OTDR trace (b) The increased reflection based on HCF's backscattering level.

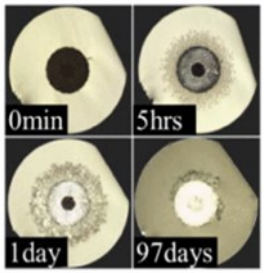

Figure 7.23 Evolution of contamination on the cleaved surface of a HCF [132].

The monitoring of the end facet contamination demonstrates that a highly sensitive OTDR system is also able to see the feature of contamination. Moreover, this is of practically importance in our analysis of the backscattering in HCFs where HCFs are often connected to SMF via free space coupling, as contamination introduces extra loss.

7.4 Bi-directional OTDR analysis

For the HCFs studied in this thesis (NANFs & DNANFs), the primary backscattering is from air within the core region [46]. Consequently, the strength of the backscattering signal, characterized by the backscattering coefficient, changes with the air pressure or composition inside the core, which can also shift over time as air moves through the core [133]. Additionally, the backscattering coefficient is predicted to change with the core size, which varies at the micrometre level in today's low-loss HCFs [18]. This variation complicates the evaluation of the distributed HCFs attenuation coefficient, as the OTDR signal is influenced by both the backscattering coefficient and attenuation, both of which are expected to vary along the fibre length. To address this, the investigation is conducted, which is based on measuring it from two ends of HCF samples, to acquire the distributed attenuation coefficient and the longitudinal backscattering coefficient.

7.4.1 Principle

For a HCF with length of *L*, its beginning (*z* = 0) is marked as “Start Of Pull” (SOP) and its end (*z* = *L*) as “End Of Pull” (EOP). Subsequently, two OTDR traces are measured: (1) when launching OTDR pulses into the SOP (Figure 7.24 (a)) and EOP (Figure 7.24 (b)) ends, respectively. Example of measured traces using 1980 m long HCF sample with NANF geometry at 1 atm pressure (end-face shown in Figure 7.24 (a)) is shown in Figure 7.24 (c). This sample is referred to as HCF-1 and further details will be provided later.

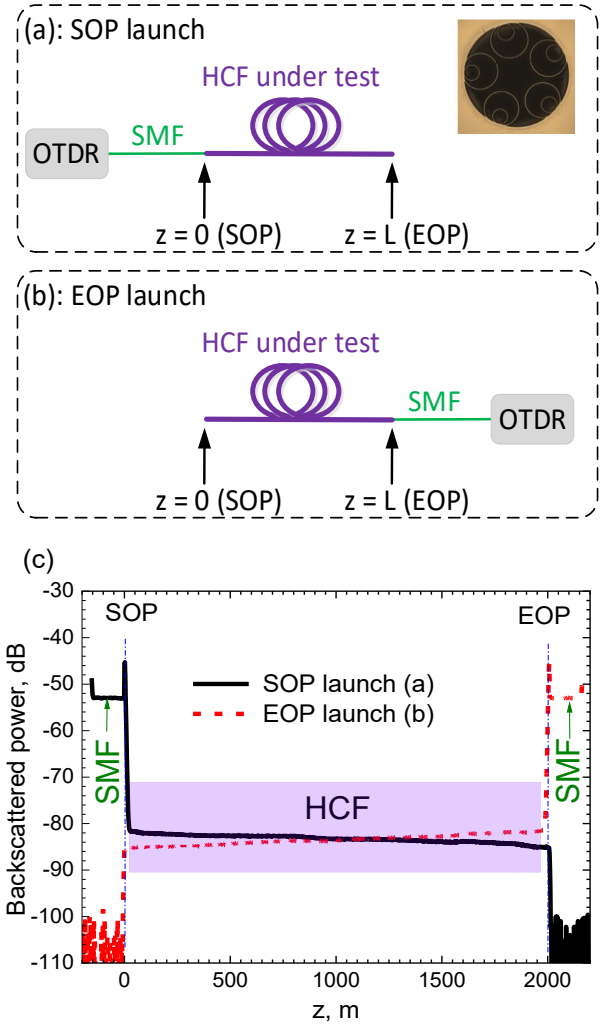

Figure 7.24 Setup for OTDR measurement performed by launching from the OTDR SMF pigtail into the HCF under test (a) from the SOP and (b) from the EOP end. Inset: cross section of NANF type HCF; (C) the obtained two OTDR traces.

In the Figure 7.24 (c), at first glance, both measured traces appear to decrease along the propagation direction due to attenuation in the HCF under test, similarly to OTDR traces of a SMF. More detailed observation, however, shows discrepancies. For example, around *z* = 1800 m, EOP launch trace (dashed) is almost flat, suggesting very small HCF attenuation, while the SOP launch trace (solid) decreases with propagation distance significantly, suggesting high HCF attenuation. As we show later, this is due to the variation in the backscattering coefficient that in this example decreases with *z* around *z* = 1800 m.

This example suggests that the backscattering coefficient and attenuation variation can be separated when analyzing SOP and EOP launch traces, which is confirmed later by theoretical analysis presented in the following section.

The backscattered power received from the SOP end EOP launch is:

$$P_{SOP}(z) = P_{SOP}^{0} B(z) e^{-2\int_0^z \alpha(u)du}, \quad 7\text{-}10$$

$$P_{EOP}(z) = P_{EOP}^{0} B(z) e^{-2\int_z^L \alpha(u)du}. \quad 7\text{-}11$$

Here, P^0 is the launched power into the HCF from SOP (subscript 'SOP') and EOP (subscript 'EOP') ends, respectively. $B(z)$ and ***α(z)*** are backscattering and attenuation coefficients at point ***z*** along the HCF.

By applying natural logarithm and summing of Eq. 7-10 and Eq. 7-11, we obtain:

$$lnP_{SOP}(z) + lnP_{EOP}(z) = lnP_{SOP}^{0} + lnP_{EOP}^{0} + 2lnB(z) - 2\int_0^L \alpha(u)du. \quad 7\text{-}12$$

Here, $A = \int_0^L \alpha(u)du$ is the total HCF loss. The backscattering coefficient is then obtained as:

$$B(z) = \exp\left(0.5\, lnP_{SOP}(z) + 0.5\, lnP_{EOP}(z) - 0.5lnP_{EOP}^{0} - 0.5lnP_{SOP}^{0} + A\right). \quad 7\text{-}13$$

When all variables are in unit of dB:

$$B(z)_{dB} = 0.5(P_{SOP}(z)_{dB} + P_{EOP}(z)_{dB}) - 0.5(P_{SOP,dB}^{0} + P_{EOP,dB}^{0}) + A_{dB}). \quad 7\text{-}14$$

Subsequently, we can obtain the accumulated loss from Eq. 7-10 and Eq.7-13:

$$\int_0^z \alpha(u)du = 0.25(\, lnP_{EOP}(z) - lnP_{SOP}(z) - lnP_{EOP}^{0} + lnP_{SOP}^{0}) + 0.5\text{A}. \quad 7\text{-}15$$

In dB:

$$\int_0^z \alpha(u)du_{dB} = 0.25\left((P_{EOP}(z)_{dB} - P_{SOP}(z)_{dB}) + (P_{SOP,dB}^{0} - P_{EOP,dB}^{0})\right) + 0.5A_{dB}. \quad 7\text{-}16$$

Then the derivate of Eq. 7-16 is the fibre attenuation coefficient along the HCF length:

$$\alpha(z)_{dB} = \frac{d}{dz}\int_0^z \alpha(u)du_{dB} = 0.25(\frac{d}{dz}P_{EOP}(z)_{dB} - \frac{d}{dz}P_{SOP}(z)_{dB}). \quad 7\text{-}17$$

The backscattering coefficient $B(z)_{dB}$ is then evaluated using Eq. 7-14 where the total HCF loss A_{dB} is evaluated from Eq. 7-16 by putting ***z*** = ***L***.

The first practical consideration regards the differentiation of data measured experimentally to obtain attenuation coefficient from Eq. 7-17, as differentiation of noisy experimental data usually produce large noise variation. The approach adopted in analysis of the SMF OTDR traces are used, in which we will firstly obtain the accumulated loss of $\int_0^z \alpha(u)du$ and then

fit it before we differentiate the fitted curve to finally obtain the attenuation coefficient along the fibre α(z).

To find $P_{SOP}(z)_{dB}$and $P_{EOP}(z)_{dB}$, we need to calibrate our OTDR, for which we use a 3.5% Fresnel back-reflection from the flat-cleaved SMF, Figure 7.25 (a). The detailed calibration will be shown later.

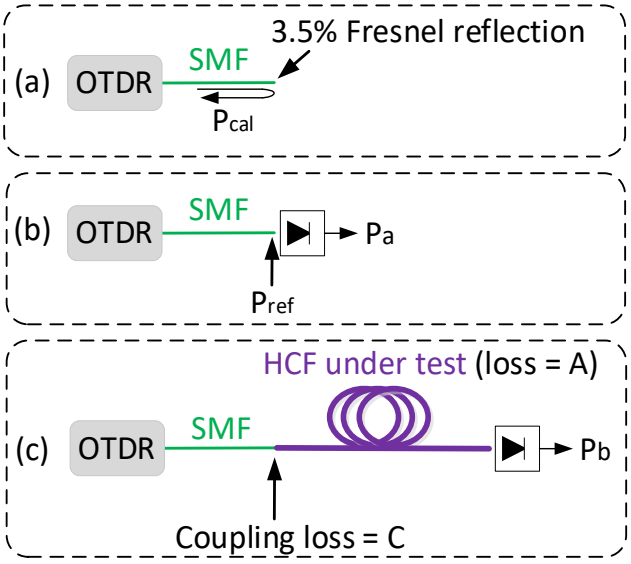

Figure 7.25 Set-up for calibrating the OTDR system (a) and to measure powers of P^a (b),and P^b (c) for evaluating the quantities of P^0_{EOP} or P^0_{SOP}.

Further, we need to derive the backscattering coefficient (Eq. 7-14) from the quantities that can be measured experimentally rather than $P^0_{SOP,dB}$,dB, $P^0_{EOP,dB}$, and A_{dB} used in Eq. 7-14. We consider experimentally-measurable quantities of power at the launching SMF output, P^a (Figure 7.25 (b)) and at the output of the HCF under test, P^b (Figure 7.25 (b)). Below we show derivation for SOP launch, as EOP launch can be treated identically. Firstly, the difference between the power measured after and before the HCF under test is due to the HCF loss A_{dB} and coupling loss C_{dB} (Figure 7.25 (c)):

$$P^a_{SOP,dB} - P^b_{SOP,dB} = C_{dB} + A_{dB}. \qquad 7\text{-}18$$

Further, light propagating in the SMF tail experiences two times coupling loss ($2C_{dB}$) when backscattered plus Fresnel loss F_{dB} (F_{dB} = 0.15 dB) entering SMF into the HCF:

$$P^0_{SOP,dB} = P^a_{SOP,dB} - 2C_{dB} - F_{dB}. \qquad 7\text{-}19$$

Note that the Fresnel loss for the SMF-HCF direction is already accounted for, as P^a is measured after light experience this Fresnel loss in the forward direction ($P_{ref,dB} = P^a_{dB} + F_{dB}$). Eq. 7-18 and Eq. 7-19 lead to:

$$P^0_{SOP,dB} = 2P^b_{SOP,dB} - P^a_{SOP,dB} + 2A_{dB} - F_{dB}, \qquad 7\text{-}20$$

and similarly for the opposite direction:

$$P^0_{EOP,dB} = 2P^b_{EOP,dB} - P^a_{EOP,dB} + 2A_{dB} - F_{dB}, \quad 7\text{-}21$$

We now can evaluate the total HCF loss A_{dB} by using Eq. 7-16 and putting $z = L$:

$$A_{dB} = \int_0^L \alpha(u)du \Big|_{dB} = 0.25\left(P_{EOP,dB}(L) - P_{SOP,dB}(L)\right) + 0.25\left(P^0_{SOP,dB} - P^0_{EOP,dB}\right) + 0.5A_{dB}, \quad 7\text{-}22$$

Giving:

$$A_{dB} = 0.5\left(P_{EOP,dB}(L) - P_{SOP,dB}(L)\right) + 0.5(P^0_{SOP,dB} - P^0_{EOP,dB}). \quad 7\text{-}23$$

Using the Eq. 7-20 and Eq. 7-21 to replace $P^0_{SOP,dB}$ and $P^0_{EOP,dB}$ in Eq. 7-23, we get:

$$A_{dB} = 0.5\left(P_{EOP,dB}(L) - P_{SOP,dB}(L)\right) + 0.5\left(2P^b_{SOP,dB} - P^a_{SOP,dB} - 2P^b_{EOP,dB} + P^a_{EOP,dB}\right) \quad 7\text{-}24$$

We then put Eq. 7-20, 7-21, and 7-24 into Eq. 7-14 to obtain the backscattering coefficient from measured quantities:

$$B(z)_{dB} = 0.5(P_{SOP,dB}(z) + P_{EOP,dB}(z) + P_{SOP,dB}(L) - P_{EOP,dB}(L)) + P^a_{SOP,dB} - 2P^b_{SOP,dB} + F_{dB}. \quad 7\text{-}25$$

The accumulated loss $A(z)_{dB}$ can be then obtained from Eq. 7-16 using Eq. 7-20, 7-21, and 7-24 as:

$$A(z)_{dB} = 0.25(P_{EOP,dB}(z) - P_{SOP,dB}(z) + P_{EOP,dB}(L) - P_{SOP,dB}(L)) + 0.5(2P^b_{SOP,dB} - P^a_{SOP,dB} - 2P^b_{EOP,dB} + P^a_{EOP,dB}). \quad 7\text{-}26$$

In regards to the attenuation coefficient $\alpha(z)_{dB}$, it does not require $P^0_{SOP,dB}$, $P^0_{EOP,dB}$ or A_{dB} and even calibration of the OTDR is not necessary. With all the parameters of interest related directly to the measurable quantities, the wanted attenuation and backscattering coefficient can be directly calculated.

7.4.2 OTDR system calibration

The used OTDR was calibrated following procedure shown in Figure 7.25 (a). As the 3.5% reflection (corresponding to -14.5 dB) is very strong and beyond the dynamic range of the OTDR detector, a variable optical attenuator was placed at the output and set it to 20.0 dB by comparing the output power with and without the attenuator. This reduced the back-reflected light by 40.0 dB, as light passes through the attenuator in both directions. The detected light than should be -14.5 - 40 = -54.5 dB below light launched into the fibre. We used 10 ns pulses and show detected OTDR trace in Figure 7.26.

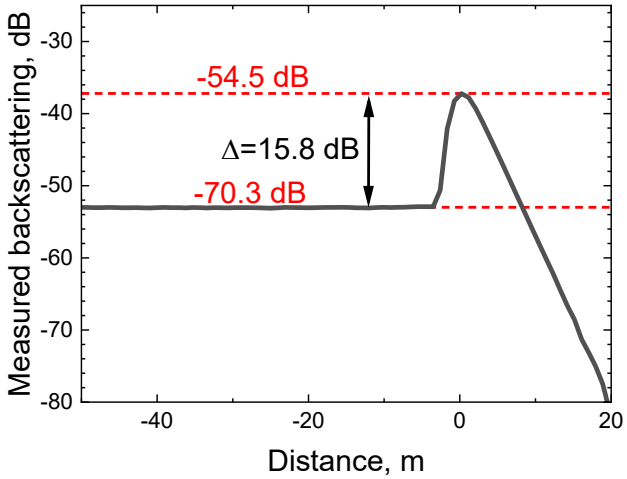

Figure 7.26 The measured backscattering from the SMF pigtail and Fresnel reflection (attenuated by 40 dB) at its end. The measured Fresnel reflection (-54.5 dB) is at the level of -37.2 dB. Then SMF pigtail backscattering is evaluated to be -70.3 dB. Given pulse width of 10 ns, this corresponds to backscattering coefficient of -70.3 dB/m.

The measured Fresnel reflection (-54.5 dB) is at the level of -37.2 dB, which is corresponding to the absolute power of -12.85 dBm for a measured pulse power of $P_{ref} = P_a + 0.15 = 41.65$ dBm (the peak power for 10 ns at P^a was measured to be 41.5 dBm). Then the backscattering power of SMF would be -12.85 - 15.8 = -28.65 dBm. As the measured level of the SMF is -53.0 dB, then the calibration constant of the system would be -28.65 - (-53.0) = 24.35 dB.

As the used 10 ns corresponds to OTDR signal received from 1 m of SMF, we can directly read backscattering from the SMF pigtail, which is -70.3 dB/m, which is a value consistent with SMF [104]. The trace in Figure 7.26 would then be calibrated to that shown in Figure 7.27.

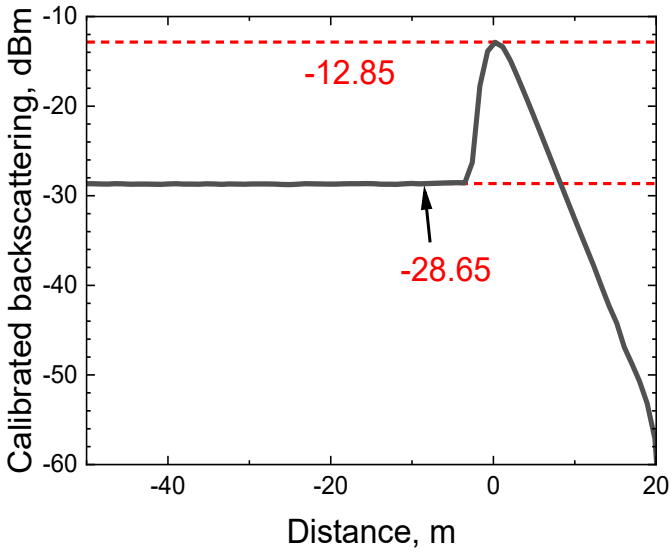

Figure 7.27 The calibration of the measured backscattering from the SMF pigtail and Fresnel reflection (attenuated by 40 dB) at its end.

7.4.3 Experimental results

To demonstrate the capability and accuracy of the developed technique, we have characterized three HCF samples, namely HCF-1 (NANF), HCF-2 (NANF) and HCF-3 (DNANF). The three samples have different core size and two of them are at atmosphere pressure, the DNANF is at sub-atmospheric condition, a so called “as-drawn” HCF and we will show them separately and summarise later. The parameters of the three samples are shown in Table 7.2. It is worth mentioning that we removed data at both ends of the samples to avoid the influence from the dead zone of the OTDR system, as shown in Figure 7.24 (c).

Table 7.2 Parameters of HCF samples.

	HCF-1	HCF-2	HCF-3
Type	NANF	NANF	DNANF
Core size, μm	34.7	31.0	26.7
Length, m	1980	680	6500
Air pressure, atm	1	1	0.25*

(*As-drawn HCF, which has sub-atmospheric air pressure [45]. Value estimated based on backscattering level [46])

7.4.3.1 Atmospheric pressure air-filled HCF

The measured OTDR traces from both SOP and EOP for HCF-1 are already shown in Figure 7.24 (c), which were then calibrated using the constant of 24.35 dB for the used OTDR system, as given in Figure 7.28. Using the Eq. 7-15, the accumulated loss can be extracted and was fitted with polynomial fitting (cubic fit), as shown in Figure 7.29 (a). For the fitting, accumulated loss traces for all samples were fitted by the 1st, 2nd, ... order polynomials and the Coefficient of Determination (R^2) was obtained for each fit. Fit was used with the polynomial order from which R^2 did not change within four digits. For example, for HCF-1, the R^2 values were 0.9932, 0.9956, 0.9972, and 0.9972 for the 1st, 2nd, 3rd, and 4th order polynomial fit, respectively. Then 3rd order was chosen, as R^2 did not change between the 3rd and 4th order. This suggested using cubic fit for all three samples. The obtained attenuation for HCF-1 (slope of the fitted curve) is shown in Figure 7.29 (b).

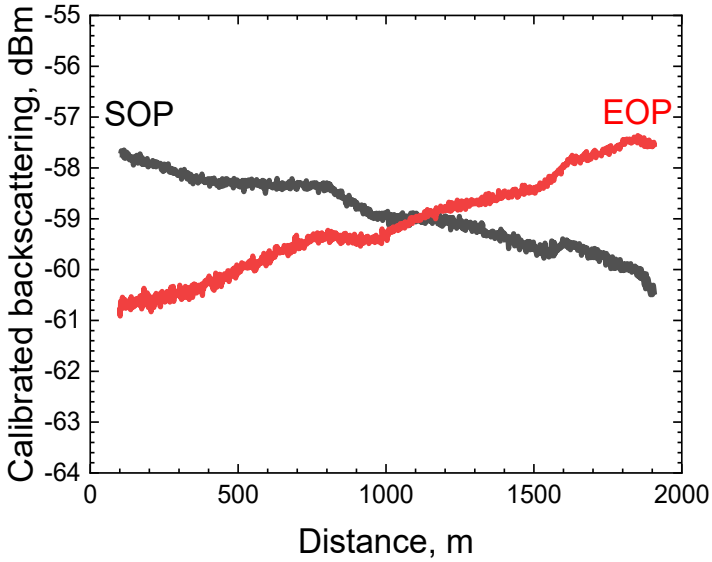

Figure 7.28 The calibrated backscattering traces when launching light from both SOP and EOP for HCF-1.

As seen in Figure 7.29 (a), the accumulated loss increases in different rate along the length and the attenuation in Figure 7.29 (b) clearly shows the attenuation distribution along the length, which suggests the minimum loss happens in middle of the fibre, while a bit higher at the start and end.

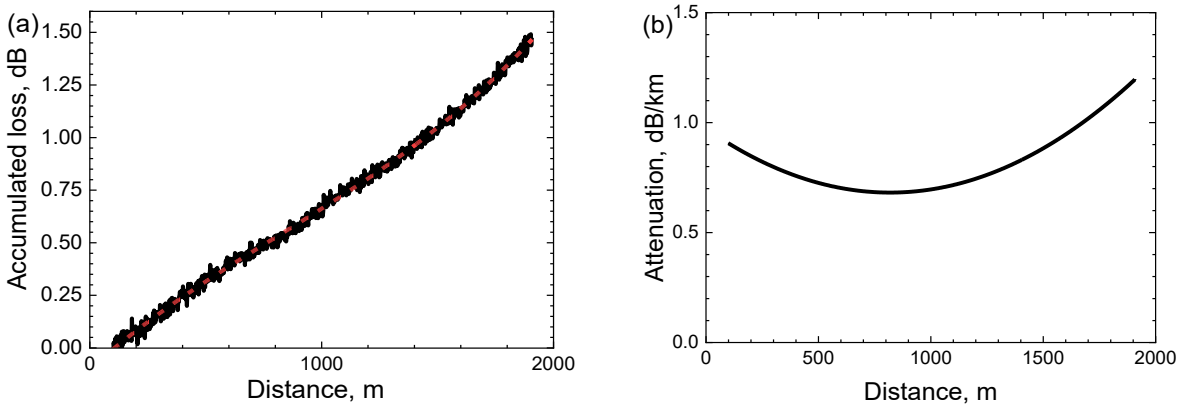

Figure 7.29 (a) The accumulated loss for HCF-1 and its polynomial fit (red dashed line) and (b) Attenuation coefficients.

The backscattering coefficient obtained using Eq. 7-25 is shown in Figure 7.30. This shows the variation of the backscattering coefficient of 0.6 dB, which is believed to be caused by the core size change. The overall backscattering coefficient level is between 98.4 dB/m and 99.0 dB/m, which is close to what is predicted in [46].

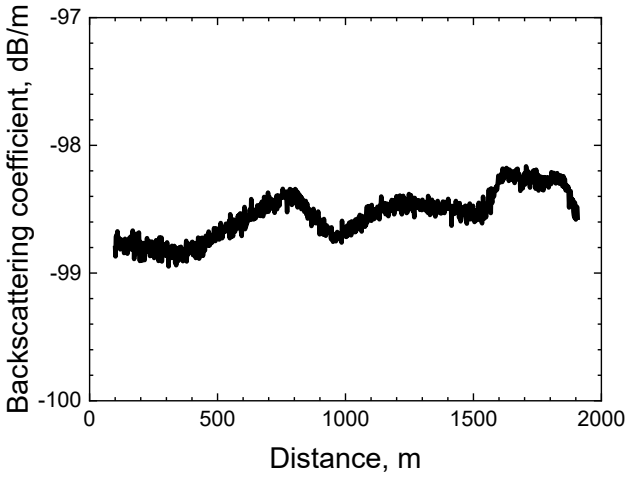

Figure 7.30 The obtained backscattering coefficient for HCF-1.

7.4.3.2 HCF in different winding conditions

For HCF-2, it is also atmospheric pressure air-filled. Here, HCF-2 sample that has relatively large bending loss was initially measured on a standard fibre bobbin (diameter of 16 cm) and subsequently rewound and remeasured on a large bobbin (diameter of 32 cm). Bending loss's influence will be, thus, shown here. The calibrated OTDR traces from SOP and EOP for HCF-2 are shown in Figure 7.31. A "bump" is observed between 200 m and 300 m.

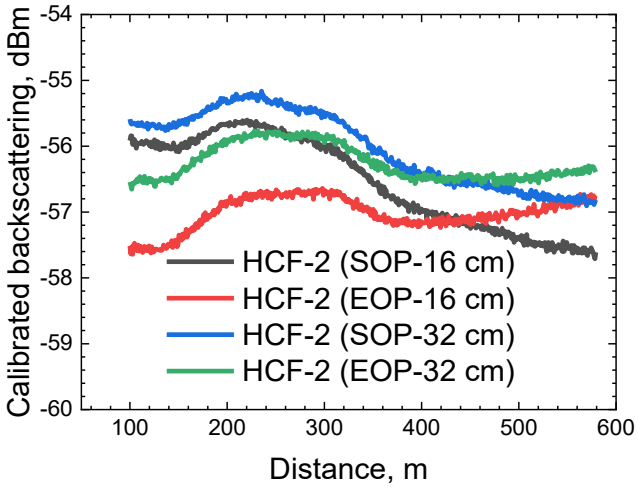

Figure 7.31 The calibrated backscattering traces when launching light from both SOP and EOP for HCF-2.

Following the same procedures as we did on HCF-1, the accumulated loss can be obtained and we fitted it with polynomial fitting (cubic fit), as shown in Figure 7.32 (a). The obtained attenuation (slope of the fitted curve) is shown in Figure 7.32 (b), which allows us to see the bending loss can cause extra loss of 0.4 dB for the 680 m fibre, almost double that of the loss when spooled properly.

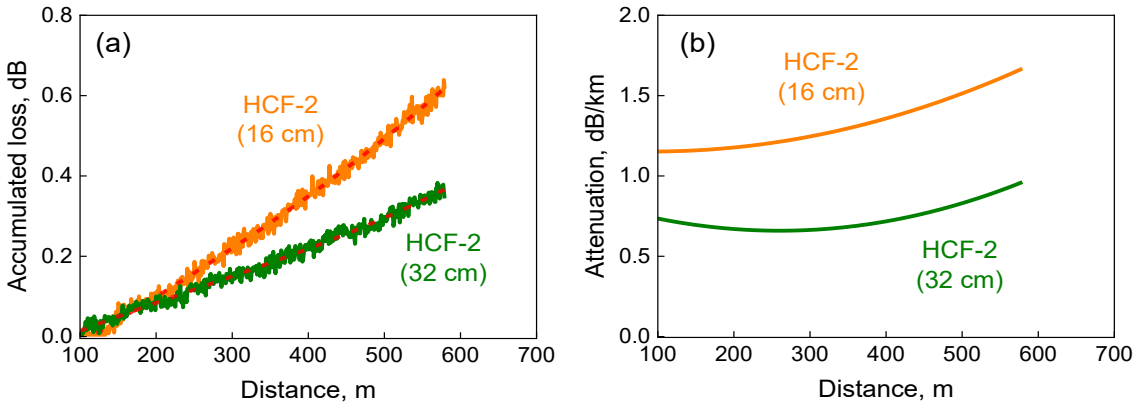

Figure 7.32 (a) The accumulated loss for HCF-2 and its polynomial fit (red dashed line) and (b) Attenuation coefficients.

The backscattering coefficient obtained using Eq. 7-25 is shown in Figure 7.33, which shows the variation of the backscattering coefficient of 1.1 dB. The overall backscattering coefficient level is around -98.4 dB/m. As we see in the direct OTDR traces, the “bump” between 200 m and 300 m shows higher backscattering coefficient, suggesting a core size variation of about 2 μm [46].

The almost same backscattering coefficient proves that bending only introduces extra loss but does not change the backscattering coefficient. Again, after we acquire the backscattering coefficient distribution of a HCF, we shall be able to monitor the bending loss of the spooled/deployed HCF via a direct OTDR measurement.

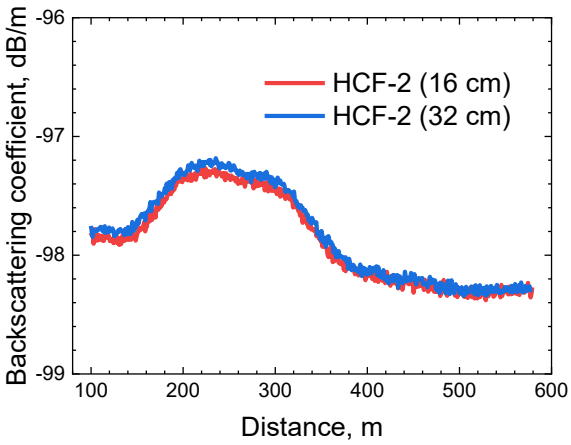

Figure 7.33 The obtained backscattering coefficient for HCF-2 in standard bobbin (red) and large bobbin(blue).

7.4.3.3 As drawn HCF (sub-atm pressure)

For the as-drawn fibre HCF-3, the calibrated OTDR traces from both SOP and EOP are shown in Figure 7.34. Although there are few peaks (defects) along the fibre, it shall not influence the results on loss and backscattering coefficient.

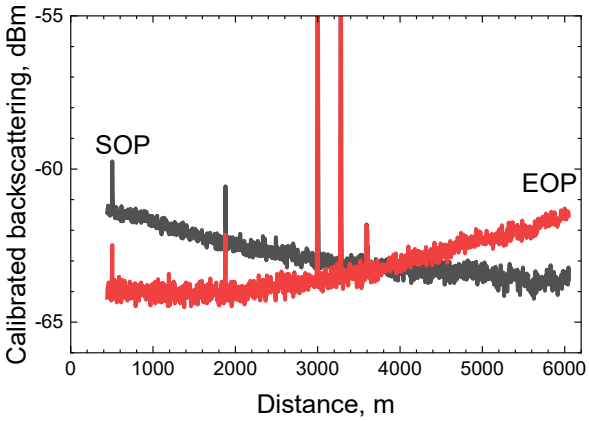

Figure 7.34 The calibrated backscattering traces when launching light from both SOP and EOP for HCF-3.

The obtained accumulated loss with polynomial fitting (cubic fit) is shown in Figure 7.35 (a) and the obtained attenuation (slope of the fitted curve) is shown in Figure 7.35 (b). The attenuation of HCF-3 increases from 0.17 dB/km to 0.25 dB/km, with an average loss of 0.21 dB/km. The observed variation along the 6.5 km length, which is usually difficult to obtain, can be useful for fabricators/designers to develop low loss HCFs.

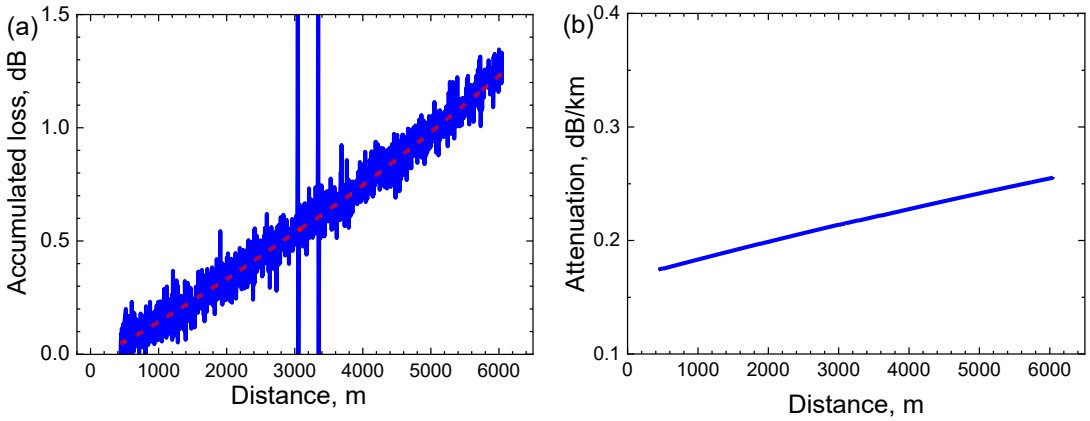

Figure 7.35 The accumulated loss for HCF-3 and its polynomial fit (red dashed line).

The obtained backscattering coefficient is shown in Figure 7.36. The backscattering coefficient level is between -103.9 dB/m and -103.2 dB/m, which decreases to reach the minimum in middle and increase again. Due to the sub-atm pressure inside the hollow core, air ingress happens during our experiment. This leads to a higher backscattering at both ends (SOP and EOP). Since we believe the pressure at SOP and EOP is at atmosphere, the difference of around 6.0 dB (in Figure 7.36 (b)) allows us to estimate the pressure inside this as-drawn HCF is around 0.25 atm (consistent with the report [43]). Therefore, the backscattering coefficient at atmospheric pressure air-filled condition is 6.0 dB higher than that shown in Figure 7.36.

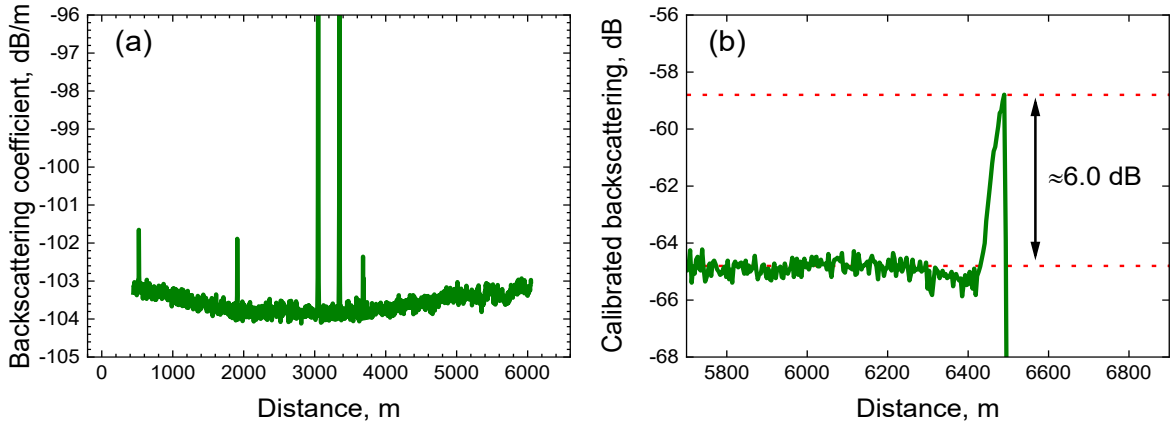

Figure 7.36 (a) The obtained backscattering coefficient for HCF-3 (sub-atm) and (b) the calibrated backscattering trace at the EOP.

7.4.4 Discussion

As all the samples were characterised with cutback method, this allows us to compare it with the results obtained via the OTDR method demonstrated here. The compared results are shown in Table 7.3. Good agreement has been achieved for both HCF-1 and HCF-3. For HCF-2, the fibre has been re-wound between the measurements to a smaller (16-cm bobbin) and back to a larger spool (32-cm bobbin), which may have slightly altered the attenuation, possibly explaining the OTDR result to be slightly higher than expected from the cut-back method.

Table 7.3 Comparison between the average loss extracted from the OTDR measurement and loss from cutback measurement.

Sample	OTDR, dB/km	Cutback, dB/km
HCF1	0.69-1.20	0.85±0.03
HCF2 (32-cm)	0.66-0.96	0.6±0.1
HCF3	0.17-0.25	0.21±0.01

The obtained backscattering coefficients of the three samples are also compared with that predicted in [46], as shown in Figure 7.37. As mentioned earlier, the pressure in HCF-3 is estimated to be 0.25 atm with the backscattering coefficient of 6.0 dB lower than atmosphere pressure, which has been compensated (from -103.2 dB/m to -97.2 dB/m). The backscattering coefficient decreases with core size, which agrees with the analysis in [46]. However, the obtained backscattering coefficients are overall higher than the prediction, which is >1.0 dB for HCF-1. The reasons behind this requires further investigation, including uncertainties of the measurement, gas composition.

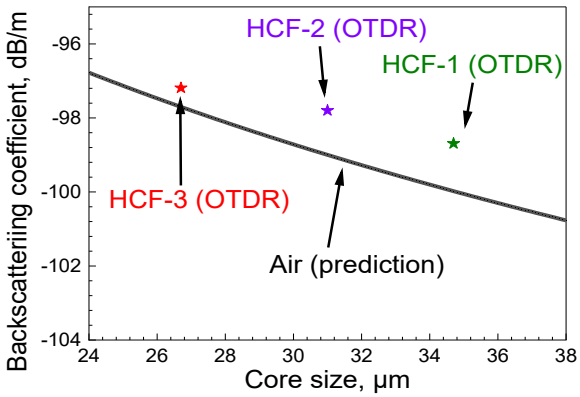

Figure 7.37 The extracted backscattering coefficient (at SOP) of three samples with the value predicted in [46] shown for comparison (HCF-3 has been compensated to 1 atm).

It has been demonstrated that the distributed attenuation coefficient can be obtained from bi-directional OTDR analysis, showing strong consistency with the values measured using the cutback method. Additionally, the acquired backscattering coefficient distribution provides valuable feedback for HCF fabricators, as it is closely related to the microstructure uniformity.

7.5 Conclusion

In this chapter, it has been demonstrated that the developed OTDR system is capable of characterising HCFs in conditions from air-filled to evacuated, which enables the technique to monitor HCFs evacuation and related studies. The demonstrated method of bi-directional OTDR analysis shows the strategy how to measure and process OTDR traces to enable distributed attenuation measurement, as well as the monitoring of the backscattering coefficient variation along the HCF length. Since the backscattering coefficient is strongly related to the microstructure of the HCFs, this finds interesting in HCF fabrication for drawing long length uniform HCFs.

Chapter 8. Summary and future work

8.1 Summary

This thesis focused on the characterisation of HCFs, which unfolded across two topics. Firstly, we study the origins of thermal sensitivity of HCFs, with a particular focus on the impact of the coating. Based on experimental results by my colleague, we uncovered, for the first time, the relaxation effect introduced by the coating on HCFs thermal expansion. Our analysis attributed this effect to the viscoelastic properties of the coating, elucidated through the application of a COMSOL model. The work was published in [35].

Based on the study of HCFs thermal sensitivity, we proposed a novel method of acquiring thermal insensitive HCF coil through optimized winding with the removal of the bobbin. The design of this coil involved a systematic simulation process to determine optimal coil parameters, including the number of turns, number of layers, coil diameter, and fibre gap. Subsequently, the designed coil was experimentally validated, showcasing a remarkable achievement with the measured thermal phase sensitivity being more than 1000 times lower than that of non-coiled SMFs. The work was published in [134].

The second part of this thesis was dedicated to the distributed characterisation of HCFs. This had been greatly inspired by the first demonstration of the backscattering in HCFs (NANFs), which is >40 dB lower than in SMFs. We started with the building of a comprehensive OTDR system. Initial experiments focused on the generation, amplification and optimization of OTDR pulses. Subsequently, we proposed a strategy to construct a highly sensitive OTDR system tailored for the characterization of HCFs. Notably, this approach utilized a commercial OTDR instrument. The achieved dynamic range exceeded that of the OTDR instrument by approximately 30 dB, resulting in a dynamic range of about 45 dB—sufficient for the characterization of HCFs. Noteworthy is the accomplishment of a high dynamic range coupled with a remarkable spatial resolution of <2.0 m, representing the best-ever reported resolution in the characterization of such HCFs. Using this system, we conducted measurements of backscattering in low-loss HCFs, revealing substantially improved performance in terms of spatial resolution, acquisition time, and signal clarity when compared to a highly sensitive photo-counting OTDR. This work was published in [135].

We extended this technique to measure the backscattering of HCFs' evacuation (NANF), which was possible through the careful management of the SMF-HCF connection, ensuring low back reflection and low insertion loss. Benefiting from its high dynamic range, we were

able to monitor the evacuation of pressure of down to below 0.1 atm, which represented the first distributed monitoring of evacuation. This work was published in [133].

The evacuation on a DNANF fibre was also conducted. Thanks to the significantly improved SMF-HCF connection (>10 dB lower back reflection than [135] and low loss of 0.5 dB), the backscattering from the microstructure surface was successfully measured. This reveals features that are strongly related to the microstructure, which is otherwise obscured by the presence of air. This was the first demonstration that shows OTDR can measure backscattering from both air-filled HCFs and evacuated HCFs, rendering it apt for the comprehensive characterization of such fibres. Furthermore, this capability serves as a powerful tool for investigating the dynamics of gas flow in HCFs and for preparing evacuated HCFs. The work has been submitted to the CLEO 2024 conference and accepted.

Since the measured backscattering is a function of not only loss, but also the core size, it becomes very challenging to obtain the useful information, e.g., loss, from the direct OTDR measurement. To address this challenge, we applied a method to separate the loss and backscattering coefficient variation. The method is based on measuring backscattering of HCFs from both ends. Samples including NANF and DNANF were used, and the loss we obtained was in good agreement with that measured by cutback. Given that the extracted backscattering coefficient is strongly related to the microstructure, e.g., core size, this can be a direct indication of the longitudinal uniformity of the fabricated HCFs. In summary, the demonstrated method holds substantial promise in both distributed characterising low loss HCFs and beneficial for drawing long length uniform and low loss HCFs. A journal paper on this work has been submitted to ACS Photonics.

8.2 Future work

Although the coating's impact has been extensively studied, the effect from its viscoelastic property limits the application where thermal sensitivity matters. Therefore, improved coating design is required. For the thermal insensitive HCF coil, the "memory" effect is significant. By using a glue to fill the fibre gaps together with thin coating, this is expected to serve as a final solution for eliminating the adverse effect of coating while achieving zero thermal sensitivity.

While our custom-built OTDR system has been instrumental in conducting various characterizations of HCFs, there exists room for further enhancement in performance, including the dead zone (currently exceeding 20 m), spatial resolution, and dynamic range. The backscattering analysis from evacuated HCFs has unveiled features related to the microstructure, prompting a need for additional study to discern their origin.

Although the employed method for extracting the loss and backscattering coefficient is promising in characterising HCFs, further detailed research is still required. For example, the impact of gas ingress induced backscattering coefficient imbalance desires further research, which will be particularly important in characterising as-drawn HCFs where the pressure is sub-atm. The accuracy of this method has not yet been analysed in detail, which shall be conducted in future. Finally, the method is believed to be useful in monitoring winding for low bending loss and perhaps of interest in gas sensing.

Appendix A: Pulse amplification optimisation

Due to the initial unsaturated gain of the amplifier, the leading edge of the pulse experiences more gain than the falling edge (>50 % as shown in Figure 7.2), resulting in an exponential decay of the pulse envelope [124, 125]. Moreover, the dramatically high peak power at the rising edge can potentially cause optical damage to the system, thus proper measures are required to mitigate this effect.

The method adopted to address this issue is based on pulse-shaping techniques, as demonstrated in various studies. The setup is shown in Figure A. 1, where an AOM is used to shape the rectangular pulse generated by the OTDR. An attenuator (-15 dB) is also used to protect the photodetector. To see more distortion, a slightly wider pulse of 100 ns is used.

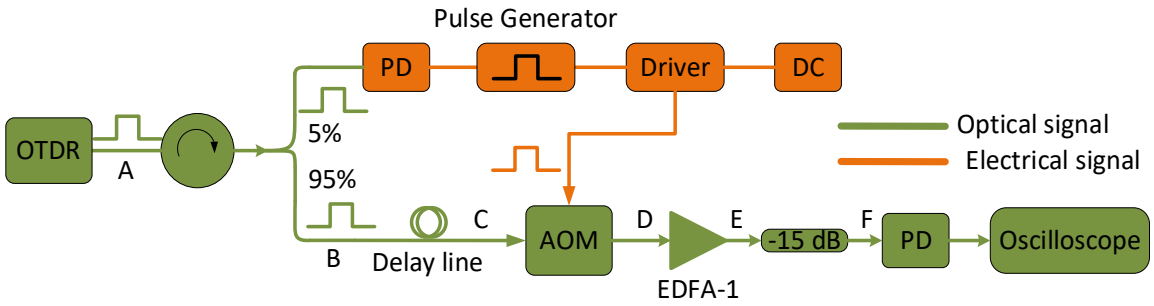

Figure A. 1 Setup for pulse-shaping and amplification

When the pulse is not shaped, the amplified pulses are shown in Figure A. 2, with the EDFA operating at small gain (pump current: 35 mA) and high gain (pump current: 250 mA). As mentioned in the setup, the amplified pulses shown here have been attenuated by 15 dB. As expected, the rising edge of the pulse sees more gain than the falling edge and the pulse at high gain is significantly distorted. To achieve a flat gain, the rising edge must be suppressed.

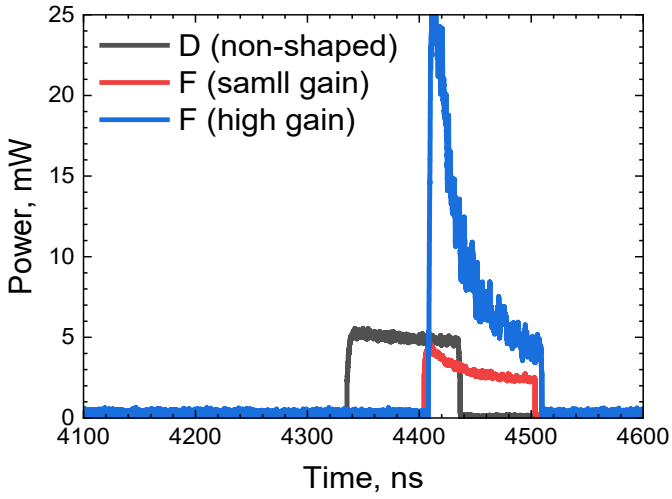

Figure A. 2 Amplified pulses when the rectangular pulse is not shaped.

An AOM is then applied to shape the pulse thanks to its limited rise time of 100 ns. The pulse delay from the generator is adjusted to get the desired shape, which is determined only visually. Two examples of the shaped pulses are shown in Figure A. 3. Even with a slight adjustment to the pulse shape, the effect is still significant, particularly for the high gain pulse.

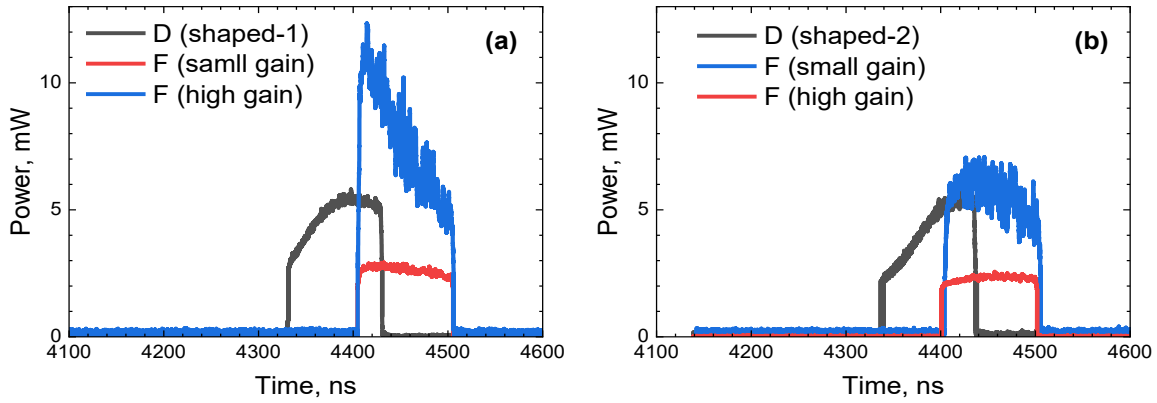

Figure A. 3 (a) The shaped pulse-1 and its amplified pulses (b) the shaped pulse-2 and its amplified pulses.

To evaluate the performance of pulse-shaping and facilitate comparisons, pulse fluctuation is defined as the relative difference between the amplitude of the falling edge and the rising edge, normalized by the amplitude of the rising edge, as illustrated in Figure A. 4.

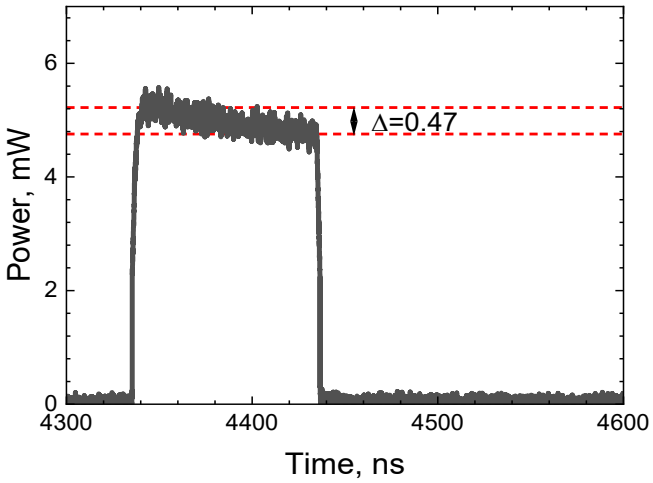

Figure A. 4 The fluctuation of the non-shaped pulse in Figure A. 2 (fluctuation of 8.9%).

The comparison results are presented in Table A. 1. Compared to the amplified pulse without shaping, the fluctuation is significantly reduced with pulse shaping. For example, when EDFA operates at small gain, the fluctuation has been reduced from 43.6% to 8.3% for shaped pulse-1, and -6.4% for shaped pulse-2. However, at higher gain level, although the fluctuation is still significantly reduced, it becomes more pronounced (-6.4% vs 23.5%). This indicates that higher gain requires more careful pulse shaping.

While shaping is not currently necessary for the present OTDR system developed in this thesis, it would become increasingly important when a higher dynamic range, such as 20 dB more, is required.

Table A. 1 Performance comparison of the amplified pulses under different pulse shapes.

EDFA state	Pulse	Power, rising edge, mW	Power, falling edge, mW	Δ	Fluctuation (%)
Small gain	Non-shaped	4.33	2.44	1.89	43.6
	Shaped-1	2.67	2.44	0.23	8.6
	Shaped-2	2.08	2.22	-0.14	-6.7
High gain	Non-shaping	25.56	4.44	21.12	82.6
	Shaped-1	10.89	4.67	6.22	57.1
	Shaped-2	5.78	4.42	1.36	23.5

Appendix B: Publications

[1] B. Shi, H. Sakr, J. Hayes, **X. Wei**, E. Numkam Fokoua, M. Ding, Z. Feng, G. Marra, F. Poletti, D. J. Richardson, and R. Slavík, "Thinly coated hollow core fibre for improved thermal phase-stability performance," *Opt. Lett*. 46, 5177-5180, 2021.

[2] **X. Wei**, A. Taranta, B. Shi, M. Ding, Z. Feng, D. J. Richardson, F. Poletti, and R. Slavík, "Support-Free Thermally Insensitive Hollow Core Fibre Coil," *J. Lightwave Technol*, 41(10), 3145-3152, 2023.

[3] **X. Wei**, B. Shi, D. J. Richardson, F. Poletti, and R. Slavík, "Distributed Characterization of Low-loss Hollow Core fibres using EDFA-assisted Low-cost OTDR instrument," *Optical Fibre Communications Conference and Exhibition (OFC)*, W1C.4, 2023.

[4] **X. Wei**, B. Shi, N. Wheeler, P. Horak, F. Poletti, and R. Slavík, "Distributed Monitoring of Evacuation of Hollow Core Fibres," *Frontiers in Optics*, FTu1D.1, 2023. (Winner of Wolf Outstanding Student Paper Award)

[5] **X. Wei**, N. V. Wheeler, S. Bakhtiari Gorajoobi, S. R. Sandoghchi, F. Poletti, and R. Slavík, “Backscattering in Antiresonant Hollow Core Fibres: from Air Scattering to Surface Scattering”, *Conference on Lasers and Electro-Optics (CLEO)*, SM3I.5, 2024.

[6] B. Shi, C. Zhang, T. Kelly, **X. Wei**, M. Ding, M. Huang, S. Fu, F. Poletti, and R. Slavik. "Splicing Hollow-Core Fiber with Standard Glass-Core Fiber with Ultralow Back-Reflection and Low Coupling Loss," *ACS Photonics*, 2024.

[7] **X. Wei**, E. Numkam Fokoua, F. Poletti, and R. Slavík, "Extraction of Attenuation and Backscattering Coefficient along Hollow Core Fiber Length using Two-Way Optical Time Domain Backscattering," *ACS Photonics*, accepted.

List of Reference

[1] R. Cregan *et al.*, "Single-mode photonic band gap guidance of light in air," *science,* vol. 285, no. 5433, pp. 1537-1539, 1999.

[2] J. C. Knight, "Photonic crystal fibres," *nature,* vol. 424, no. 6950, pp. 847-851, 2003.

[3] F. Poletti, M. N. Petrovich, and D. J. Richardson, "Hollow-core photonic bandgap fibers: technology and applications," *Nanophotonics,* vol. 2, no. 5-6, pp. 315-340, 2013.

[4] G. T. Jasion *et al.*, "0.174 dB/km hollow core double nested antiresonant nodeless fiber (DNANF)," *Optical Fiber Communication Conference (OFC)*, Th4C.7, 2022.

[5] H. Sakr *et al.*, "Towards hollow-core optical fibers with lower attenuation than silica fibers," *Next-Generation Optical Communication: Components, Sub-Systems, and Systems XI*, SPIE, PC1202802, 2022.

[6] H. Sakr *et al.*, "Hollow core optical fibres with comparable attenuation to silica fibres between 600 and 1100 nm," *Nature communications,* vol. 11, no. 1, p. 6030, 2020.

[7] F. e. Poletti *et al.*, "Towards high-capacity fibre-optic communications at the speed of light in vacuum," *Nature Photonics,* vol. 7, no. 4, pp. 279-284, 2013.

[8] H. Mulvad *et al.*, "Kilowatt-average-power single-mode laser light transmission over kilometre-scale hollow-core fibre," *Nature Photonics,* vol. 16, no. 6, pp. 448-453, 2022.

[9] V. Michaud-Belleau *et al.*, "Backscattering in antiresonant hollow-core fibers: over 40 dB lower than in standard optical fibers," *Optica,* vol. 8, no. 2, pp. 216-219, 2021.

[10] R. Slavík *et al.*, "Ultralow thermal sensitivity of phase and propagation delay in hollow core optical fibres," *Scientific reports,* vol. 5, no. 1, p. 15447, 2015.

[11] A. Saljoghei *et al.*, "First Demonstration of Field-Deployable Low Latency Hollow-core Cable Capable of Supporting> 1000km, 400Gb/s WDM Transmission," *arXiv preprint arXiv:2106.05343,* 2021.

[12] A. Nespola *et al.*, "Ultra-long-haul WDM transmission in a reduced inter-modal interference NANF hollow-core fiber," *Optical Fiber Communication Conference (OFC)*, F3B. 5, 2021.

[13] P. Poggiolini and F. Poletti, "Opportunities and challenges for long-distance transmission in hollow-core fibres," *Journal of Lightwave Technology,* vol. 40, no. 6, pp. 1605-1616, 2022.

[14] G. A. Sanders *et al.*, "Hollow-core resonator fiber optic gyroscope using nodeless anti-resonant fiber," *Optics Letters,* vol. 46, no. 1, pp. 46-49, 2021.

[15] W. S. Brooks *et al.*, "Development of a gas-phase Raman instrument using a hollow core anti-resonant tubular fibre," *Journal of Raman Spectroscopy,* vol. 52, no. 10, pp. 1772-1782, 2021.

[16] F. Poletti, "Nested antiresonant nodeless hollow core fiber," *Opt. Express,* vol. 22, no. 20, pp. 23807-23828, 2014.

[17] G. Bablani. "Microsoft acquires Lumenisity®, an innovator in hollow core fiber (HCF) cable."Microsoft. https://blogs.microsoft.com/blog/2022/12/09/microsoft-acquires-lumenisity-an-innovator-in-hollow-core-fiber-hcf-cable/ (accessed 5th August 2023).

[18] L. Budd *et al.*, "Longitudinal Non-Destructive Characterization of Nested Antiresonant Nodeless Fiber Microstructure Geometry and Twist," *Optical Fiber Communications Conference and Exhibition (OFC)*, W4D.2, 2023.

[19]Y. T. Chen, "Use of single-mode optical fiber in the stabilization of laser frequency," *Applied optics,* vol. 28, no. 11, pp. 2017-2021, 1989.

[20]D. Li *et al.,* "Efficient laser noise reduction method via actively stabilized optical delay line," *Opt. Express,* vol. 25, no. 8, pp. 9071-9077, 2017.

[21]B. S. Sheard *et al.*, "High-bandwidth laser frequency stabilization to a fiber-optic delay line," *Applied optics,* vol. 45, no. 33, pp. 8491-8499, 2006.

[22]F. Kéfélian, H. Jiang, P. Lemonde, and G. Santarelli, "Ultralow-frequency-noise stabilization of a laser by locking to an optical fiber-delay line," *Optics letters,* vol. 34, no. 7, pp. 914-916, 2009.

[23]J. Dong *et al.*, "Subhertz linewidth laser by locking to a fiber delay line," *Applied optics,* vol. 54, no. 5, pp. 1152-1156, 2015.

[24]M. Digonnet *et al*., "Sensitivity and stability of an air-core fibre-optic gyroscope," *Measurement Science and Technology,* vol. 18, no. 10, p. 3089, 2007.

[25]D. M. Shupe, "Thermally induced nonreciprocity in the fiber-optic interferometer," *Applied optics,* vol. 19, no. 5, pp. 654-655, 1980.

[26]A. Hartog, A. Conduit, and D. Payne, "Variation of pulse delay with stress and temperature in jacketed and unjacketed optical fibres," *Optical and Quantum Electronics,* vol. 11, pp. 265-273, 1979.

[27]W. Zhu *et al.*, "The thermal phase sensitivity of both coated and uncoated standard and hollow core fibers down to cryogenic temperatures," *Journal of Lightwave Technology,* vol. 38, no. 8, pp. 2477-2484, 2019.

[28] Z. Feng *et al.*, "Fiber interferometry with low temperature sensitivity," *IEEE Photonics Conference (IPC)*, pp. 1-2, 2020.

[29] M. Bousonville *et al.*, "New phase stable optical fiber," *Proc. Beam Instrum. Workshop*, pp. 101-103, 2012.

[30]V. Dangui et al., "Phase sensitivity to temperature of the fundamental mode in air-guiding photonic-bandgap fibers," *Opt. Express,* vol. 13, no. 18, pp. 6669-6684, 2005.

[31]S. Blin *et al*., "Reduced thermal sensitivity of a fiber-optic gyroscope using an air-core photonic-bandgap fiber," *Journal of Lightwave Technology,* vol. 25, no. 3, pp. 861-865, 2007.

[32]M. Ding *et al.*, "Long-length and thermally stable high-finesse Fabry-Perot interferometers made of hollow core optical fiber," *Journal of Lightwave Technology,* vol. 38, no. 8, pp. 2423-2427, 2020.

[33] H. K. Kim, V. Dangui, M. Digonnet, and G. Kino, "Fiber-optic gyroscope using an air-core photonic-bandgap fiber,"*17th International Conference on Optical Fibre Sensors*, vol. 5855: SPIE, pp. 198-201, 2005.

[34]G. White, "Thermal expansion of reference materials: copper, silica and silicon," *Journal of Physics D: Applied Physics,* vol. 6, no. 17, p. 2070, 1973.

[35]B. Shi *et al.*, "Thinly coated hollow core fiber for improved thermal phase-stability performance," *Optics Letters,* vol. 46, no. 20, pp. 5177-5180, 2021.

[36]W. Zhu *et al.*, "Temperature insensitive fiber interferometry," *Optics Letters,* vol. 44, no. 11, pp. 2768-2770, 2019.

[37]T. Ito *et al*., "New Methods for Evaluating Optical Fiber Coating Materials," *Furukawa Review,* vol. 22, pp. 1-3, 2002.

[38] Y. P. Michel *et al*., "Mechanical characterisation of the four most used coating materials for optical fibres," *International Conference on Photonics, Optics and Laser Technology (PHOTOPTICS)*, vol. 1, pp. 91-95, 2015.

[39] M. Ding *et al*., "Hollow core fiber temperature sensitivity reduction via winding on a thermally-insensitive coil," *Conference on Lasers and Electro-Optics (CLEO)*, STu1Q.7, 2021.

[40]R. Slavík *et al.*, "Demonstration of opposing thermal sensitivities in hollow-core fibers with open and sealed ends," *Optics letters,* vol. 44, no. 17, pp. 4367-4370, 2019.

[41]D. L. Philen *et al*., "Single-mode fiber OTDR: Experiment and theory," *IEEE Transactions on Microwave Theory and Techniques,* vol. 30, no. 10, pp. 1487-1496, 1982.

[42]R. Passy *et al*., "Experimental and theoretical investigations of coherent OFDR with semiconductor laser sources," *Journal of lightwave technology,* vol. 12, no. 9, pp. 1622-1630, 1994.

[43]S. Rikimi *et al.*, "Internal gas composition and pressure in as-drawn hollow core optical fibers," *Journal of Lightwave Technology,* vol. 40, no. 14, pp. 4776-4785, 2022.

[44]V. Michaud-Belleau *et al.*, "Fundamental thermal noise in antiresonant hollow-core fibers," *Physical Review A,* vol. 106, no. 2, p. 023501, 2022.

[45] S. Rikimi *et al.*, "Transient differential pressure-induced loss variation in as-drawn hollow core optical fibres," *Micro-Structured and Specialty Optical Fibres VII*, vol. 12140, p. 1214002, 2022.

[46]E. Numkam Fokoua et al., "Theoretical analysis of backscattering in hollow-core antiresonant fibers," *APL Photonics,* vol. 6, no. 9, 2021.

[47]R. Slavík *et al.*, "Optical time domain backscattering of antiresonant hollow core fibers," *Opt. Express,* vol. 30, no. 17, pp. 31310-31321, 2022.

[48]P. Eraerds *et al*., "Photon counting OTDR: advantages and limitations," *Journal of Lightwave Technology,* vol. 28, no. 6, pp. 952-964, 2010.

[49] K. C. Kao and G. A. Hockham, "Dielectric-fibre surface waveguides for optical frequencies," *Proceedings of the Institution of Electrical Engineers*, vol. 113, no. 7: IET, pp. 1151-1158, 1966.

[50]T. Birks *et al*., "Full 2D photonic band gaps in silica/air structures," *Electronics letters,* vol. 31, no. 22, pp. 1941-1943, 1995.

[51]J. Knight, T. Birks, P. S. J. Russell, and D. Atkin, "All-silica single-mode optical fiber with photonic crystal cladding," *Optics letters,* vol. 21, no. 19, pp. 1547-1549, 1996.

[52] N. Venkataraman *et al.*, "Low loss (13 dB/km) air core photonic band-gap fibre," *28th European Conference on Optical Communication*, PD1.1, 2002.

[53] B. Mangan *et al.*, "Low loss (1.7 dB/km) hollow core photonic bandgap fiber," *Optical Fiber Communications Conference and Exhibition (OFC)*, PD24, 2004.

[54]P. J. Roberts *et al.*, "Ultimate low loss of hollow-core photonic crystal fibres," *Opt. Express,* vol. 13, no. 1, pp. 236-244, 2005.

[55]E. Numkam Fokoua *et al*., "Loss in hollow-core optical fibers: mechanisms, scaling rules, and limits," *Advances in Optics and Photonics,* vol. 15, no. 1, pp. 1-85, 2023.

[56]F. Couny, F. Benabid, and P. Light, "Large-pitch kagome-structured hollow-core photonic crystal fiber," *Optics letters,* vol. 31, no. 24, pp. 3574-3576, 2006.

[57] F. Couny, F. Benabid, and P. S. Light, "Large pitch Kagome-structured hollow-core PCF," *Conference on Lasers and Electro-Optics (CLEO)*, CWF1, 2007.

[58] Y. Wang, F. Couny, P. Roberts, and F. Benabid, "Low loss broadband transmission in optimized core-shape Kagome hollow-core PCF," *Conference on Lasers and Electro-Optics (CLEO)*, CPDB4, 2010.

[59]S. Février, B. Beaudou, and P. Viale, "Understanding origin of loss in large pitch hollow-core photonic crystal fibers and their design simplification," *Opt. Express,* vol. 18, no. 5, pp. 5142-5150, 2010.

[60]A. D. Pryamikov *et al*., "Demonstration of a waveguide regime for a silica hollow-core microstructured optical fiber with a negative curvature of the core boundary in the spectral region> 3.5 μm," *Opt. Express,* vol. 19, no. 2, pp. 1441-1448, 2011.

[61]W. Belardi and J. C. Knight, "Hollow antiresonant fibers with reduced attenuation," *Optics letters,* vol. 39, no. 7, pp. 1853-1856, 2014.

[62] T. D. Bradley *et al.*, "Record low-loss 1.3 dB/km data transmitting antiresonant hollow core fibre," *European Conference on Optical Communication (ECOC)*, pp. 1-3, 2018.

[63] T. D. Bradley *et al.*, "Antiresonant hollow core fibre with 0.65 dB/km attenuation across the C and L telecommunication bands," *European Conference on Optical Communication (ECOC)*, pp. 1-4, 2019.

[64] G. T. Jasion *et al.*, "Hollow core NANF with 0.28 dB/km attenuation in the C and L bands," *Optical Fiber Communication Conference (OFC)*, Th4B. 4, 2020.

[65] H. Sakr *et al.*, "Hollow core NANFs with five nested tubes and record low loss at 850, 1060, 1300 and 1625nm," *Optical Fiber Communication Conference(OFC)*, F3A. 4, 2021.

[66]Y. Tamura *et al.*, "The first 0.14-dB/km loss optical fiber and its impact on submarine transmission," *Journal of Lightwave Technology,* vol. 36, no. 1, pp. 44-49, 2018.

[67]M. Zeisberger and M. A. Schmidt, "Analytic model for the complex effective index of the leaky modes of tube-type anti-resonant hollow core fibers," *Scientific reports,* vol. 7, no. 1, p. 11761, 2017.

[68]Y. Wang and W. Ding, "Confinement loss in hollow-core negative curvature fiber: A multi-layered model," *Opt. Express,* vol. 25, no. 26, pp. 33122-33133, 2017.

[69]N. Litchinitser, A. Abeeluck, C. Headley, and B. Eggleton, "Antiresonant reflecting photonic crystal optical waveguides," *Optics letters,* vol. 27, no. 18, pp. 1592-1594, 2002.

[70]K. Nagayama *et al*., "Ultra-low-loss (0.1484 dB/km) pure silica core fibre and extension of transmission distance," *Electronics Letters,* vol. 38, no. 20, p. 1, 2002.

[71]D. Bird, "Attenuation of model hollow-core, anti-resonant fibres," *Opt. Express,* vol. 25, no. 19, pp. 23215-23237, 2017.

[72]K. Saitoh and M. Koshiba, "Confinement losses in air-guiding photonic bandgap fibers," *IEEE Photonics Technology Letters,* vol. 15, no. 2, pp. 236-238, 2003.

[73]W. Zheng *et al.*, "Wideband low confinement loss anti-resonant hollow core fiber with nested U-shape tube," *Opt. Express,* vol. 29, no. 15, pp. 24182-24192, 2021.

[74]X. Chen *et al.*, "Double negative curvature anti-resonance hollow core fiber," *Opt. Express,* vol. 27, no. 14, pp. 19548-19554, 2019.

[75]Y. Chen, *et al*., "Hollow Core DNANF Optical Fiber with <0.11 dB/km Loss," *Optical Fiber Communication Conference(OFC)*, Th4A.8, 2024.

[76]E. N. Fokoua *et al*., "How to make the propagation time through an optical fiber fully insensitive to temperature variations," *Optica,* vol. 4, no. 6, pp. 659-668, 2017.

[77] A. Van Newkirk *et al*., "High power laser delivery using anti-resonant hollow core fiber," *Photonic Fiber and Crystal Devices: Advances in Materials and Innovations in Device Applications XV*, vol. 11826: SPIE, pp. 38-41, 2021.

[78]A. Iyer *et al.*, "Ultra-low Brillouin scattering in anti-resonant hollow-core fibers," *APL Photonics,* vol. 5, no. 9, 2020.

[79]J. D. Shephard *et al.*, "High energy nanosecond laser pulses delivered single-mode through hollow-core PBG fibers," *Opt. Express,* vol. 12, no. 4, pp. 717-723, 2004.

[80]Q. Fu *et al.*, "Hundred-meter-scale, kilowatt peak-power, near-diffraction-limited, mid-infrared pulse delivery via the low-loss hollow-core fiber," *Optics Letters,* vol. 47, no. 20, pp. 5301-5304, 2022.

[81]B. Debord *et al*., "Hollow-core fiber technology: the rising of “gas photonics”," *Fibers,* vol. 7, no. 2, p. 16, 2019.

[82]M. Nikodem, "Laser-based trace gas detection inside hollow-core fibers: A review," *Materials,* vol. 13, no. 18, p. 3983, 2020.

[83]A. M. Cubillas *et al*., "Gas sensor based on photonic crystal fibres in the 2v(3) and v(2)+2v(3) vibrational bands of methane," *Sensors,* vol. 9, no. 8, pp. 6261-6272, 2009.

[84]F. Benabid *et al*., "Compact, stable and efficient all-fibre gas cells using hollow-core photonic crystal fibres," *Nature,* vol. 434, no. 7032, pp. 488-491, 2005.

[85]F. Benabid, J. C. Knight, G. Antonopoulos, and P. S. J. Russell, "Stimulated Raman scattering in hydrogen-filled hollow-core photonic crystal fiber," *Science,* vol. 298, no. 5592, pp. 399-402, 2002.

[86]P. S. J. Russell *et al*., "Hollow-core photonic crystal fibres for gas-based nonlinear optics," *Nature Photonics,* vol. 8, no. 4, pp. 278-286, 2014.

[87]M. Cassataro *et al.*, "Generation of broadband mid-IR and UV light in gas-filled single-ring hollow-core PCF," *Opt. Express,* vol. 25, no. 7, pp. 7637-7644, 2017.

[88]F. Benabid, J. Knight, and P. S. J. Russell, "Particle levitation and guidance in hollow-core photonic crystal fiber," *Opt. Express,* vol. 10, no. 21, pp. 1195-1203, 2002.

[89]W. Jin *et al.*, "Recent advances in spectroscopic gas sensing with micro/nano-structured optical fibers," *Photonic Sensors,* vol. 11, pp. 141-157, 2021.

[90]D. Suslov *et al.*, "All-fiber hollow-core fiber gas cell," *Optical Fiber Technology,* vol. 81, p. 103513, 2023.

[91]C. Zhang *et al.*, "Angle-spliced SMF to hollow core fiber connection with optimized back-reflection and insertion loss," *Journal of Lightwave Technology,* vol. 40, no. 19, pp. 6474-6479, 2022.

[92]G. T. Jasion *et al.*, "Fabrication of tubular anti-resonant hollow core fibers: modelling, draw dynamics and process optimization," *Opt. Express,* vol. 27, no. 15, pp. 20567-20582, 2019.

[93]S.-T. Shiue and T.-Y. Shen, "Design of double-coated optical fibers to minimize long-term axial-strain-induced microbending losses," *Optical and quantum electronics,* vol. 34, pp. 1219-1229, 2002.

[94]S.-T. Shiue, "Design of double-coated optical fibers to minimize long-term hydrostatic-pressure-induced microbending losses," *Optics Letters,* vol. 26, no. 3, pp. 128-130, 2001.

[95]D. Gloge, "Optical-Fiber Packaging and Its Influence on Fiber Straightness and Loss," *Bell System Technical Journal,* vol. 54, no. 2, pp. 245-262, 1975.

[96]W. B. Gardner, "Microbending loss in optical fibers," *The bell system technical journal,* vol. 54, no. 2, pp. 457-465, 1975.

[97]K. Koo, A. Tveten, and A. Dandridge, "Passive stabilization scheme for fiber interferometers using (3× 3) fiber directional couplers," *Applied Physics Letters,* vol. 41, no. 7, pp. 616-618, 1982.

[98]L. Li, L. Xia, Z. Xie, and D. Liu, "All-fiber Mach-Zehnder interferometers for sensing applications," *Opt. Express,* vol. 20, no. 10, pp. 11109-11120, 2012.

[99]M. Mičuda *et al.*, "Highly stable polarization independent Mach-Zehnder interferometer," *Review of Scientific Instruments,* vol. 85, no. 8, 2014.

[100]J. Song *et al*., "Long-range high spatial resolution distributed temperature and strain sensing based on optical frequency-domain reflectometry," *IEEE Photonics Journal,* vol. 6, no. 3, pp. 1-8, 2014.

[101]L. Palmieri and L. Schenato, "Distributed optical fiber sensing based on Rayleigh scattering," *The Open Optics Journal,* vol. 7, no. 1, 2013.

[102]M. Barnoski and S. Jensen, "Fiber waveguides: a novel technique for investigating attenuation characteristics," *Applied optics,* vol. 15, no. 9, pp. 2112-2115, 1976.

[103]M. K. Barnoski, M. D. Rourke, S. Jensen, and R. Melville, "Optical time domain reflectometer," *Applied optics,* vol. 16, no. 9, pp. 2375-2379, 1977.

[104]https://www.corning.com/media/worldwide/coc/documents/Fiber/product-information-sheets/PI-1424-AEN.pdf (accessed 2023).

[105]B. L. Danielson, "Optical time-domain reflectometer specifications and performance testing," *Applied optics,* vol. 24, no. 15, pp. 2313-2322, 1985.

[106]P. Lu *et al.*, "Distributed optical fiber sensing: Review and perspective," *Applied Physics Reviews,* vol. 6, no. 4, 2019.

[107]S. Liehr, *Fibre optic sensing techniques based on incoherent optical frequency domain reflectometry*. Bundesanstalt für Materialforschung und-prüfung (BAM), 2015.

[108]B. Walker. "Measurement Good Practice Guide No. 31-Calibration and Use of Optical Time Domain Reflectometers (OTDR)." https://eprintspublications.npl.co.uk/2091/1/MGPG31.pdf (accessed 2024).

[109]F. Scholder *et al*., "Long-distance OTDR using photon counting and large detection gates at telecom wavelength," *Optics communications,* vol. 213, no. 1-3, pp. 57-61, 2002.

[110]B. Deng, Y. Shi, and F. Yuan, "Investigation on the structural origin of low thermal expansion coefficient of fused silica," *Materialia,* vol. 12, p. 100752, 2020.

[111]X. Li *et al.*, "Fiber-optic temperature sensor based on difference of thermal expansion coefficient between fused silica and metallic materials," *IEEE Photonics Journal,* vol. 4, no. 1, pp. 155-162, 2011.

[112]B. Shi *et al.*, "Thinly coated hollow core fiber for improved thermal phase-stability performance," *Optics Letters,* vol. 46, no. 20, pp. 5177-5180, 2021.

[113]S.-T. Shiue and Y.-K. Tu, "Relaxation of thermal stresses in double-coated optical fibers," *Journal of applied physics,* vol. 86, no. 8, pp. 4085-4090, 1999.

[114]S. S. Reddy, B. J. Overton, and S. M. Watson, "Influence of stress relaxation in primary coatings on low-temperature attenuation in optical fibers," *Fiber Optic Materials and Components*, vol. 2290: SPIE, pp. 19-28, 1994.

[115]Z. Zheng and R. Zhang, "Implementation of a viscoelastic material model to simulate relaxation in glass transition," in *COMSOL Conference Proceedings. Boston, USA*, 2014.

[116]Y. C. Ching *et al.*, "Effects of high temperature and ultraviolet radiation on polymer composites," in *Durability and Life Prediction in Biocomposites, Fibre-Reinforced Composites and Hybrid Composites*: Elsevier, pp. 407-426, 2019.

[117]N. Lagakos, J. Bucaro, and J. Jarzynski, "Temperature-induced optical phase shifts in fibers," *Applied optics,* vol. 20, no. 13, pp. 2305-2308, 1981.

[118]https://www.thorlabs.com/images/TabImages/Rise_Time_3dB_Bandwidth_Relationship_Lab_Fact.pdf (accessed2024).

[119]M. Esposito *et al.*, "Fiber Bragg Grating sensors to measure the coefficient of thermal expansion of polymers at cryogenic temperatures," *Sensors and Actuators A: Physical,* vol. 189, pp. 195-203, 2013.

[120]Y. C. Hsueh, S. C. Chiou, and S. T. Shiue, "Minimisation of thermally induced microbending losses in dual-coated optical fibres caused by viscoelastic behaviour of commercial polymeric coatings," *IET Optoelectronics,* vol. 9, no. 3, pp. 141-144, 2015.

[121]W. Ling *et al*., "Thermal effects of fiber sensing coils in different winding pattern considering both thermal gradient and thermal stress," *Optics Communications,* vol. 356, pp. 290-295, 2015.

[122]Z. Zhang and F. Yu, "Quantitative analysis for the effect of the thermal physical property parameter of adhesive on the thermal performance of the quadrupolar fiber coil," *Opt. Express,* vol. 25, no. 24, pp. 30513-30525, 2017.

[123]J. P. Salvestrini *et al*., "Analysis and Control of the DC Drift in LiNbO3-Based Mach–Zehnder Modulators," *Journal of Lightwave Technology,* vol. 29, no. 10, pp. 1522-1534, 2011.

[124]D. Taverner *et al*., "158-μJ pulses from a single-transverse-mode, large-mode-area erbium-doped fiber amplifier," *Optics Letters,* vol. 22, no. 6, pp. 378-380, 1997.

[125]D. Meena *et al.*, "Mitigation of EDFA transient effects in variable duty cycle pulsed signals," *Defence Technology,* vol. 15, no. 3, pp. 276-281, 2019.

[126]D. Suslov *et al.*, "Low loss and broadband low back-reflection interconnection between a hollow-core and standard single-mode fiber," *Opt. Express,* vol. 30, no. 20, pp. 37006-37014, 2022.

[127]Y. Li, X. Yang, X. Hao, and S. Wu, "Study of gas dynamics in hollow-core photonic crystal fibers," *Optik,* vol. 246, p. 167797, 2021.

[128]J. Henningsen and J. Hald, "Dynamics of gas flow in hollow core photonic bandgap fibers," *Applied optics,* vol. 47, no. 15, pp. 2790-2797, 2008.

[129]E. Elistratova *et al.*, "Distributed measurement of hollow-core fibre gas filling and venting via optical time-domain reflectometry," *2023 Conference on Lasers and Electro-Optics Europe & European Quantum Electronics Conference (CLEO/Europe-EQEC)*, ce_2_4, 2023.

[130]D. Suslov *et al.*, "Low loss and high performance interconnection between standard single-mode fiber and antiresonant hollow-core fiber," *Scientific Reports,* vol. 11, no. 1, p. 8799, 2021.

[131]M. Komanec *et al.*, "Low-loss and low-back-reflection hollow-core to standard fiber interconnection," *IEEE Photonics Technology Letters,* vol. 31, no. 10, pp. 723-726, 2019.

[132]S. Rikimi *et al.*, "Growth of ammonium chloride on cleaved end-facets of hollow core fibers," *Conference on Lasers and Electro-Optics (CLEO)*, SF2P. 4, 2020.

[133]X. Wei *et al.*, "Distributed Monitoring of Evacuation of Hollow Core Fibers," *Frontiers in Optics*, FTu1D.1, 2023.

[134]X. Wei *et al.*, "Support-Free Thermally Insensitive Hollow Core Fiber Coil," *Journal of Lightwave Technology,* vol. 41, no. 10, pp. 3145-3152, 2023.

[135]X. Wei *et al.*, "Distributed Characterization of Low-loss Hollow Core Fibers using EDFA-assisted Low-cost OTDR instrument," *Optical Fiber Communication Conference (OFC),* W1C. 4, 2023.